

AD \_\_\_\_\_

Award Number: DAMD17-02-1-0124

TITLE: Optimized Hyperthermia Treatment of Prostate Cancer Using  
a Novel Intracavitary Ultrasound Array

PRINCIPAL INVESTIGATOR: Nadine B. Smith, Ph.D.

CONTRACTING ORGANIZATION: The Pennsylvania State University  
University Park, PA 16802-7000

REPORT DATE: January 2004

TYPE OF REPORT: Annual

PREPARED FOR: U.S. Army Medical Research and Materiel Command  
Fort Detrick, Maryland 21702-5012

DISTRIBUTION STATEMENT: Approved for Public Release;  
Distribution Unlimited

The views, opinions and/or findings contained in this report are those of the author(s) and should not be construed as an official Department of the Army position, policy or decision unless so designated by other documentation.

20040524 136

<b>REPORT</b>			Form Approved OMB No. 074-0188		
<b>DOCUMENTATION PAGE</b>					
Public reporting burden for this collection of information is estimated to average 1 hour per response, including the time for reviewing instructions, searching existing data sources, gathering and maintaining the data needed, and completing and reviewing this collection of information. Send comments regarding this burden estimate or any other aspect of this collection of information, including suggestions for reducing this burden to Washington Headquarters Services, Directorate for Information Operations and Reports, 1215 Jefferson Davis Highway, Suite 1204, Arlington, VA 22202-4302, and to the Office of Management and Budget, Paperwork Reduction Project (0704-0188), Washington, DC 20503					
<b>1. AGENCY USE ONLY</b> (Leave blank)		<b>2. REPORT DATE</b> January 2004		<b>3. REPORT TYPE AND DATES COVERED</b> Annual (14 Dec 2002 - 13 Dec 2003)	
<b>4. TITLE AND SUBTITLE</b>  Optimized Hyperthermia Treatment of Prostate Cancer Using a Novel Intracavitary Ultrasound Array				<b>5. FUNDING NUMBERS</b>  DAMD17-02-1-0124	
<b>6. AUTHOR(S)</b>  Nadine B. Smith, Ph.D.					
<b>7. PERFORMING ORGANIZATION NAME(S) AND ADDRESS(ES)</b>  The Pennsylvania State University University Park, PA 16802-7000  E-Mail: nbs@engr.psu.edu				<b>8. PERFORMING ORGANIZATION REPORT NUMBER</b>	
<b>9. SPONSORING / MONITORING AGENCY NAME(S) AND ADDRESS(ES)</b>  U.S. Army Medical Research and Materiel Command Fort Detrick, Maryland 21702-5012				<b>10. SPONSORING / MONITORING AGENCY REPORT NUMBER</b>	
<b>11. SUPPLEMENTARY NOTES</b>  Original contains color plates: ALL DTIC reproductions will be in black and white					
<b>12a. DISTRIBUTION / AVAILABILITY STATEMENT</b> Approved for Public Release; Distribution Unlimited					<b>12b. DISTRIBUTION CODE</b>
<b>13. ABSTRACT (Maximum 200 Words)</b>  The eventual goal this research is to produce an ultrasound hyperthermia array which will uniformly heat the prostate to clinical temperatures for the treatment of prostate disease. This goal can be achieved by accounting for the physical differences between the prostate gland and surrounding tissue structures. It was therefore possible to design and construct as a transducer to produce uniform heating within the prostate while causing minimal damage to surrounding tissue. The second year of this three year research project was focused on the construction of the array based on our Year 1 results of computer simulations of the ultrasound energy interactions with the prostate. Three major areas accomplished during this term were: (a) transducer construction (b) optimization of the transducer array design, and (c) MRI thermometry experiments ( <i>in vitro</i> and <i>in vivo</i> ) using the hyperthermia ultrasound array. Specifically, a clinical applicator of the phased array has been constructed and is being used for MRI experiments. Additional information from the tissue modeling during Year 2 will be used to refine the heating pattern and can easily be incorporated in the current design. To summarize, there are no deviations from the original research plan and this research is progressing on schedule.					
<b>14. SUBJECT TERMS</b> Ultrasound, hyperthermia, array, noninvasive, thermometry magnetic resonance imaging, in vitro and in vivo results					<b>15. NUMBER OF PAGES</b> 129
					<b>16. PRICE CODE</b>
<b>17. SECURITY CLASSIFICATION OF REPORT</b> Unclassified	<b>18. SECURITY CLASSIFICATION OF THIS PAGE</b> Unclassified	<b>19. SECURITY CLASSIFICATION OF ABSTRACT</b> Unclassified		<b>20. LIMITATION OF ABSTRACT</b> Unlimited	

## Table of Contents

Cover.....	1
SF 298.....	2
Introduction.....	4
Body.....	5
Key Research Accomplishments.....	29
Reportable Outcomes.....	30
Conclusions.....	31
References.....	32
Appendices.....	33

## 1. INTRODUCTION:

This second year annual report describe the progress to date on the development of an optimized intracavitary ultrasound array system to be used in the treatment of prostate cancer. Studies have shown that ultrasound hyperthermia is a useful adjuvant to radiotherapy in the treatment of prostate cancer. The basic goal of this research is the development of an ultrasound phased array to uniformly heat the prostate to 43°C for 30-60 minutes for an effective hyperthermia treatment. To accomplish this goal an array has been developed and constructed using the hypothesis that ultrasonic wavefields can be optimized to specifically target prostate tissue, resulting in uniform hyperthermia treatment within the prostate and minimal effects to surrounding tissue. Evaluation of the heating of the ultrasound has used magnetic resonance imaging (MRI) with the proton resonance frequency shift method to noninvasively determine the temperature rise from the array with *in vitro* and *in vivo* experiments. This Year 2 annual report will describe the current progress and results.

## 2. BODY:

Ultrasonic hyperthermia is a promising technique for treatment of prostate cancer. When performed in conjunction with chemotherapy or radiotherapy, hyperthermia increases the damage to cancer cells caused by radiation, and prevents subsequent repair of cancerous tumors<sup>1,2</sup>. Intracavitary ultrasound arrays are an ideal tool for performance of hyperthermia treatments, because deep localized heating can be achieved with precise power control and without any ionizing radiation.

By accounting for the physical differences between the prostate gland and surrounding tissue structures, it was possible to design a transducer to cause heating within an area approximating the size of the prostate in rabbit thigh muscle, while causing minimal damage to surrounding tissue. A two-dimensional intracavitary array transducer was constructed and is currently being evaluated using exposimetry techniques and magnetic resonance imaging (MRI) thermometry methods. Summarizing from the original grant application, the overall specific aims from this project are:

### Specific Aims (briefly):

1. Realistic modeling of ultrasound prostate hyperthermia: An anatomically and physically accurate model will be implemented to simulate high-amplitude ultrasonic propagation in the prostate and surrounding tissues.
2. Beam design and optimization: Using the new model for ultrasound-prostate interaction, optimal sonications for therapeutic hyperthermia will be determined.
3. Hyperthermia array design and fabrication: A two-dimensional array transducer will be designed for practical realization of the optimal sonication methods. Based on the optimal design, array prototypes will be constructed and tested. Exposimetry of the ultrasound pressure field will be used to compare theoretical and experimental results.
4. *In vitro* and *in vivo* hyperthermia monitored with MR thermometry: Evaluation of the two-dimensional array will be conducted using MR thermometry.
5. *In vivo* prostate hyperthermia and evaluation: Using the two-dimensional ultrasound array, *in vivo* prostate hyperthermia will be administered to dogs.

Within the second year of this project, plus or minus a couple months given the overlap with years one and three, the timeline for progress of this research was broken into three major areas:

- (a) tissue modeling, beam design and optimization,
- (b) hyperthermia array construction
- (c) *in vitro* and *in vivo* noninvasive MRI temperature monitoring of the array

### Year two timeline:

#### Beam design and optimization

- Simulate hyperthermia treatments in the tissue models as a function of wave and beam parameters. (Months 6-18)
- Optimize wavefield and beam parameters for prostate hyperthermia treatments. (Months 9-18)

### Hyperthermia array design and fabrication

- Design transducer for realization of ultrasonic beams corresponding to optimal temperature distributions. (Months 8-18)
- Transducer construction and crystal dicing. Machining of transducer body. Cabling and crystal matching to resonance frequency. (Months 10-15)
- Transducer exposimetry and evaluation. (Months 12-18)

### *In vitro* and *in vivo* hyperthermia monitored with MRI thermometry

- Compare simulated temperature fields with three-dimensional MR temperature maps in phantoms and *in vivo* rabbit muscle using the ultrasound array. (Months 18-24)
- Refine beam design based on measured temperature maps and complementary simulations. (Months 18-24)

The results herein will describe the progress and results achieved on this project over this past year in three sections.

### 2.1. Ultrasound Hyperthermia Transducer Construction

The ultrasound transducer was designed based on the hypothesis that ultrasonic wavefields can be optimized to specifically target prostate tissue, resulting in uniform hyperthermia treatment within the prostate and minimal effects on surrounding tissue. The goals of this research are to determine the optimal wavefield characteristics for specific thermal treatment of the prostate, to design and implement a transducer optimized for prostate hyperthermia, and to confirm the transducer's performance through *in vitro* and *in vivo* experiments. Construction of a second prototype transducer is described in Section 2.2 Tissue Modeling. However, the design of this prototype will continue to be modified during year three based on improved optimization modeling studies.

The proposed design that took into consideration the anatomical measurements of the prostate and the rectal wall is shown in Fig 1.

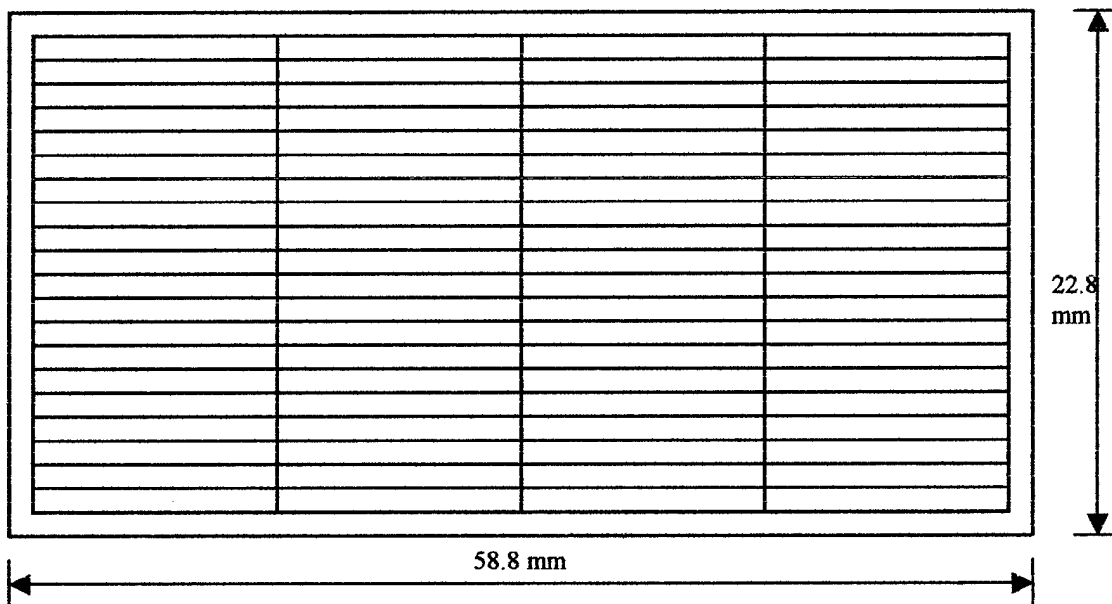


Figure 1. Sketch representation of the 20 x 4 element phased array pattern; the yellow represents inactive elements while white color represents active ones. The inactive elements were used to affix the array to the housing.

Four one dimensional (1D) arrays were arranged as shown; the dimensions of the total array including the inactive elements was  $58.8 \times 22.8 \text{ mm}^2$ . This sized transducer was determined to have the ability to generate the correct amount of energy deep inside the prostate gland and at the same time reduce the discomfort for patients during the treatment. The inner elements were connected in parallel (i.e. driven with same phases) because of restrictions in the electronics of the amplifier system that controls the phase and the power of each element. The focal point of each single one-dimensional array can be controlled separately, while the driving power for each sub-element can be controlled independently.

Construction of this array was based on simulations of the acoustic pressure field. Figure 2(a) illustrates the orientation of the xz and yz planes of the phased array.

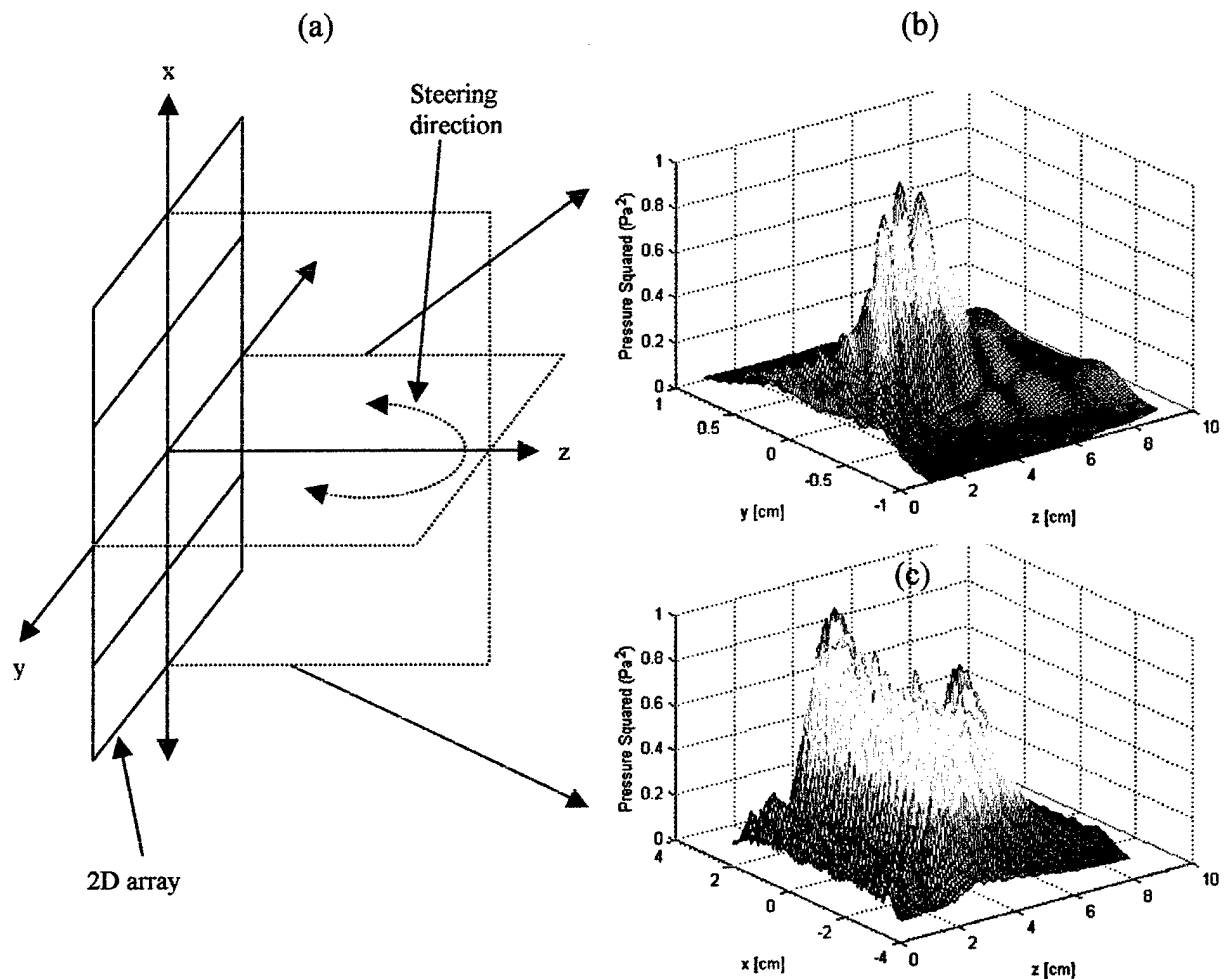


Figure 2: The drawing (a) represents the two dimensional phased array illustrating the xz and yz planes; the origin of the xyz plane is designated at (0, 0, 0) cm. The normalized squared pressure distribution through yz plane (b) and xz plane (c) is shown while focusing at (0, 0, 4) cm.

The simulation places the transducer at (0, 0, 0) cm and focuses the beam at (0, 0, 4) cm. The normalized pressure squared distribution on the yz plane is shown in Fig. 2(b), and

the distribution on the  $xz$  plane is shown in Fig. 2(c). The beam can be steered in the  $yz$  plane to help in distributing the acoustic energy as required for uniform temperature increases deep inside the prostate gland when placing the array inside the rectum. The area near the rectal wall shows the maximum destructive interference which reduces the risk of harming the surrounding tissue.

Figure 3(a) shows contour plots of the normalized squared pressure distribution on the  $xz$  plane. Based on the pressures and using the bioheat transfer equation<sup>3</sup> the temperature increase, Fig. 3(b), was determined after one minute of heating in a homogeneous medium (i.e. water). Many parameters were varied for this array to achieve an optimal thermal therapy treatment. These parameters include varying the phases of each linear array separately, altering the power of each array and changing the power of each element disjointedly. These diverse control parameters will continue to improve the treatment protocol and solve many problems when testing the array with *in vivo* animal experiments under inhomogeneous and variable perfusion tissues.

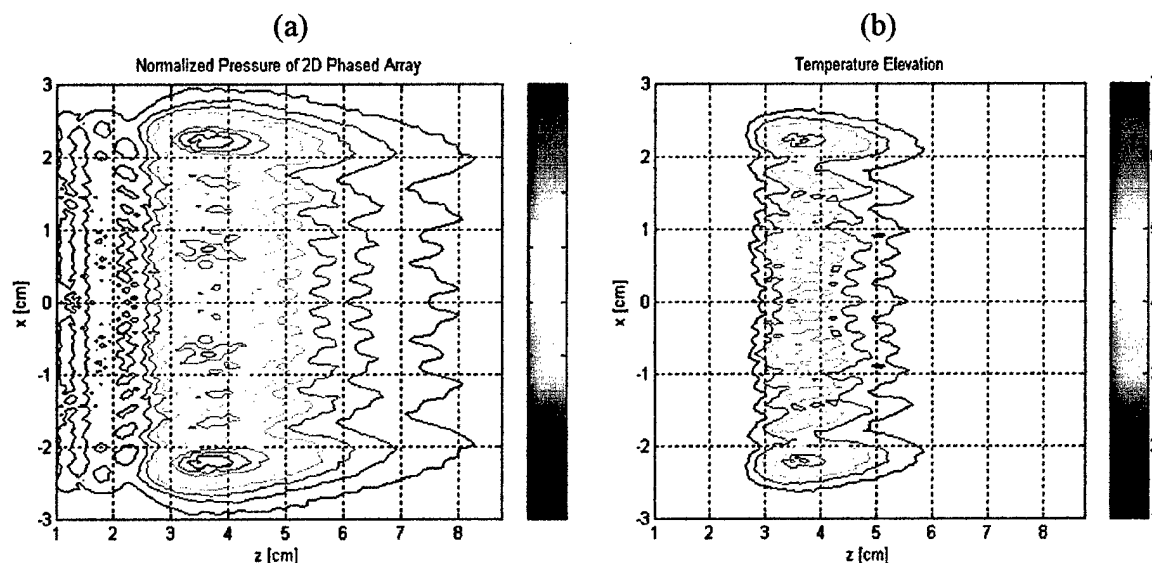


Figure 3: Contour plots showing the pressure distribution in the  $xz$  plane (a) of the two dimensional phased array while focusing at (0, 0, 4) cm, and the temperature increase (b) after one minute of heating, in homogenous material (i.e. water).

Lead zirconate titanate (PZT-8, TRS Ceramic, State College, PA, USA) was used to construct the  $20 \times 4$  ultrasound phased array; PZT-8 is capable of withstanding higher driving electrical powers than other materials such as PZT-5A and PZT-4. To increase the efficiency of acoustical energy transmission from the high acoustical impedance of PZT-8 (34 Mrayl) to the low acoustical impedance of water or soft tissue (1.5 Mrayl), two matching layers were designed. The calculated acoustic impedance for the first and second layers, assuming a water coupling medium, were 9.8 and 2.3 Mrayl, respectively.

To construct the double matching layers, parafilm was used to affix an appropriately sized PZT-8 piece to a glass plate. An adhesive primer was poured onto the surface of the transducer face. The piece was surrounded with an epoxy dam and a silver conducting matching layer was poured onto the transducer surface, which was prepared



using a 2:1 epoxy-to-silver mixture of Insulcast 501 (Insulcast, Roseland, NJ, USA) and 2-3 micron silver epoxy (Aldrich, Milwaukee, WI, USA). The whole assembly was centrifuged for 10 minutes and cured overnight. The surface of the matching layer was then sanded and lapped to the designed quarter wavelength thickness. The second matching layer was prepared in a similar fashion but without centrifuging. Parts A and B of EPO-TEK 301 (Epoxy technology, Billerica MA, USA) were mixed using 20:5 mixing ratio to create a clear uncured viscous fluid. Another piece of glass was used to spread this mixture on top of the first conductive layer and was fixed in place using appropriate fixtures while the epoxy was allowed to cure overnight. The fixture and the second glass piece were later removed, and another sanding and lapping process was performed to reduce the thickness of this layer to the required thickness. The PZT-8 piece with its two acoustical matching layers was removed from the glass and then diced in our lab using a Model 780, K & S-Kulick and Soffa Industries dicing saw (Willow Grove, PA, USA) into a complete array of 80 elements. The cutting blade had a kerf width of 0.12 mm. Figure 4 shows the final diced PTZ-8 ceramic, which is similar to the original design of Fig. 1.

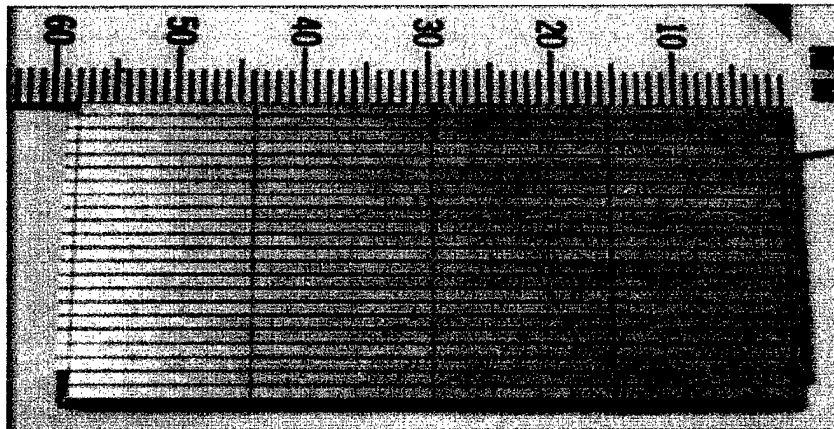


Figure 4: Photo of the diced PZT ceramic showing the separate 20 x 4 elements. Coaxial cables are soldered to the diced elements on this side of the ceramic, while the reverse side of the ceramic has the matching layers.

Sixty, 28 AWG, miniature MRI compatible coaxial cables (Belden Inc., St. Louis, Missouri, USA) six meters in length were bundled together to form the connection between the elements of the array and the amplifier system. A micro-tip soldering pin was used to solder the core of each coaxial cable to its designated element. The soldering temperature was kept below 500°F (less than the Curie temperature of PZT-8) to prevent any damage to the piezoelectric material (Fig. 5). The shields of the coax were tied together, and this ground connection was extended to the conductive matching layer through four wires running to the corners of the layer.

A specially designed transducer housing for the array was machined in-house using Delrin® magnet compatible material. Brass tubes were connected in the Delrin® housing for water and air circulation. The final constructed transrectal array probe is shown in Fig. 6, which contains 20 x 4 transducer elements and suitable brass tubes to

implement water and air circulation. The array was fitted into the housing, and bonded and insulated with a waterproof insulation material.

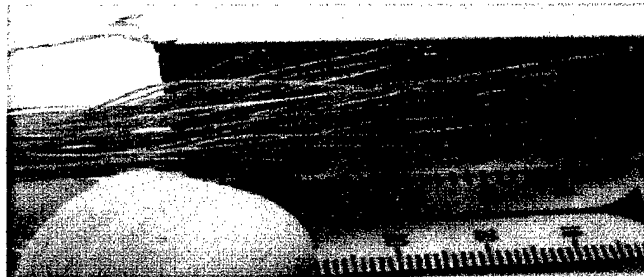


Figure 5: The soldering of 60 miniature coaxial cables is shown . For the ground connections, four wires were connected between the corners of the conductive matching layer and a common ground connection on the cables.

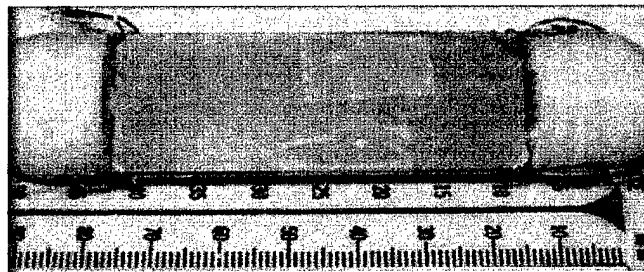


Figure 6: Photograph showing the transrectal probe after assembling the soldered array and the appropriate brass tubes into the MRI compatible housing.

## 2.2 Tissue Modeling

Although a couple of prototype arrays have been constructed and are currently being evaluated using noninvasive MRI thermometry methods using *in vitro* tissue phantoms and *in vivo* rabbit thigh muscle, modifications to the array design will continue during the third year as described with the results in this section .

### 2.2.1 Nonlinear acoustic propagation

One of the limitations of current propagation methods used for designing ultrasound probes is that the sound field is assumed to be linear. However, it is well known in the physical acoustics community that the amplitude of the ultrasound is sufficiently high that nonlinear acoustic propagation effects should be taken into account. One of the original overall goals of this project is to include the effects of realistic acoustic nonlinearities in modeling the hyperthermia process.

During the last year a new algorithm for the propagation of ultrasound including acoustical nonlinearities has been established. At the present time the algorithm has been formulated, and it will be programmed and tested during year 3 of the project. The new nonlinear propagation method is a modification of the linear k-space method being used

elsewhere in the project. It turns out, however, that one must be quite careful in making the nonlinear extension. An overview of the new algorithm will now be presented, neglecting explicit thermoviscous absorption effects that could be included in a subsequent modified formulation.

The density scaled wave equation for the present k-space method<sup>3</sup> is

$$\nabla^2 f - \sqrt{\rho(\bar{x})} f \nabla^2 \frac{1}{\sqrt{\rho(\bar{x})}} - \frac{1}{c^2(\bar{x})} \frac{\partial^2 f}{\partial t^2} = 0$$

where  $f = p / \sqrt{\rho(\bar{x})}$  is the acoustic pressure scaled by the square root of the spatially dependent density, and  $c(x)$  is the spatially dependent speed of sound. To include fluid dynamic nonlinearities in this equation one must go back to a fundamental equation of nonlinear acoustics, the Westervelt equation<sup>4</sup>. The Westervelt equation includes cumulative nonlinear acoustic effects such as nonlinear steepening and harmonic generation, disregarding local nonlinear acoustic effects such as radiation pressure, and this is sufficient for biomedical ultrasound applications. After some lengthy mathematical manipulations, a density scaled wave equation including acoustic nonlinearities is

$$\nabla^2 f - \sqrt{\rho(\bar{x})} f \nabla^2 \frac{1}{\sqrt{\rho(\bar{x})}} - \frac{1}{c^2(\bar{x})} \frac{\partial^2 f}{\partial t^2} = - \frac{\beta}{\sqrt{\rho_0} c_0^4} \frac{\partial^2 (f^2)}{\partial t^2}$$

The additional term of the right hand side gives the nonlinear effect. Notice the  $f^2$ , acting as the source of nonlinearity. Here  $\beta$  is the well known coefficient of nonlinearity, different for each type of fluid or tissue.

The method of solving the above nonlinear density scaled wave equation proceeds similarly to that in the conventional, linear k-space method. The harmonic oscillator equation now takes the form

$$\frac{\partial^2 W2(\bar{k}, t)}{\partial t^2} = (c_0^2 k^2) (VNL2(\bar{k}, t) - W2(\bar{k}, t)) - Q(\bar{k}, t)$$

where  $w2 = f_s + v_{NL2}$  is an auxiliary field (where the subscript s refers to the scattered part of the acoustic field),  $W2(\bar{k}, t)$  is its spatial Fourier transform,

$$v_{NL2}(\bar{x}, t) = \left( \frac{c_0^2}{c^2(\bar{x})} - 1 \right) f - \frac{\beta}{\sqrt{\rho_0} c_0^2} (f_s^2 + 2f_s f_i)$$

(where the subscript i refers to the incident part of the acoustic field) with spatial Fourier transform

$$VNL2(\bar{k}, t) = F \left\{ \left( \frac{c_0^2}{c^2(\bar{x})} - 1 \right) \left[ f_i + w2 - \frac{\beta}{\sqrt{\rho_0} c_0^2} (f_s^2 - 2f_s f_i) \right] - \frac{\beta}{\sqrt{\rho_0} c_0^2} (f_s^2 - 2f_s f_i) \right\},$$

and

$$Q(\bar{k}, t) = F \left\{ c_0^2 \sqrt{\rho(\bar{x})} \nabla^2 \left( \frac{1}{\sqrt{\rho(\bar{x})}} \right) [f_i - w2 - v_{NL2}] \right\}.$$

This solution procedure is only slightly modified from that of the linear k-space method. One merely needs to form the scattered field  $f_s = w_2 - v_{NL2}$  at every time step. This is required in the new nonlinear algorithm since the nonlinearity acts on the total field, not just the scattered field. In this method it is also important to make sure the absolute magnitude of the field is correct, since linear amplitude scaling throughout the field no longer applies. Hence, the sources will have to be calibrated for the nonlinear k-space method.

This new approach could be viewed a type of multidimensional Pestorius algorithm<sup>4</sup>, albeit with spatial instead of temporal Fourier transforms. The nonlinear effects are included at every time step in the time domain and slowly accumulate. To test the new algorithm, one-dimensional nonlinear acoustic waves will be propagated, and the computational results will be tested in the coming months against well-known analytical results for steepening and harmonic generation. The new approach can then be applied to the multidimensional hyperthermia propagation problems of interest in this project.

### 2.2.2 "Fresnel-lens-like" Transducer

As described in last year's report, a secondary technique—a "Fresnel-lens-like" transducer—which we believe to be novel, is being pursued for prostate hyperthermia treatment. The idea has evolved further since the last report. As described before, its design is motivated by several goals for a practical prostate hyperthermia treatment. The first is to heat the entire prostate, if possible, by 6°C for 30-60 minutes. If it is not possible to heat the entire prostate, then it is especially important that the back (toward the rectum) and sides of the prostate should receive the treatment, as that is where 80% of the cancers are found. There should be no hot or cold spots in the treatment. Because the effective thermal dose doubles for every degree above 6°C, and decreases by a factor of four for every degree below 6°C, the maximum range for the temperature rise can be taken to be  $\pm 1^\circ\text{C}$ , although a tolerance of  $\pm 0.5^\circ\text{C}$  would be considerably better. Finally, the treatment should not take too long, perhaps no more than an hour, because of patient comfort and cost of the treatment. The desirability of a quick overall treatment and the need to heat nearly the entire prostate essentially dictates that all parts of the prostate need to be heated simultaneously in a clinically fielded ultrasonic system.

The frequency of the system is constrained by the anatomy in the neighborhood of the prostate and the absorption of sound. Figure 7 shows the sagittal, coronal and axial views through the center of the prostate. As can be seen by the white circle, the prostate is roughly 3 cm in diameter and is also about 3 cm from the center of the rectum. (This circle and this format of the three views will be used for orientation in several other figures, below.) The ultrasonic frequency must be picked high enough that there is sufficient absorption of sound as it travels the 3 cm through the prostate. However, the frequency must also be low enough that the absorption is low enough that sufficient acoustic energy makes to the prostate as it travels the roughly 3 cm from the rectum to the prostate. A good compromise is in the range of 1-2 MHz where the attenuation is about 0.5 to 1 dB/cm. Thus at 1 dB/cm attenuation, for example, about half the power of the sound (3 dB) will be lost going to the prostate, and about half of what is left will be deposited within the prostate.

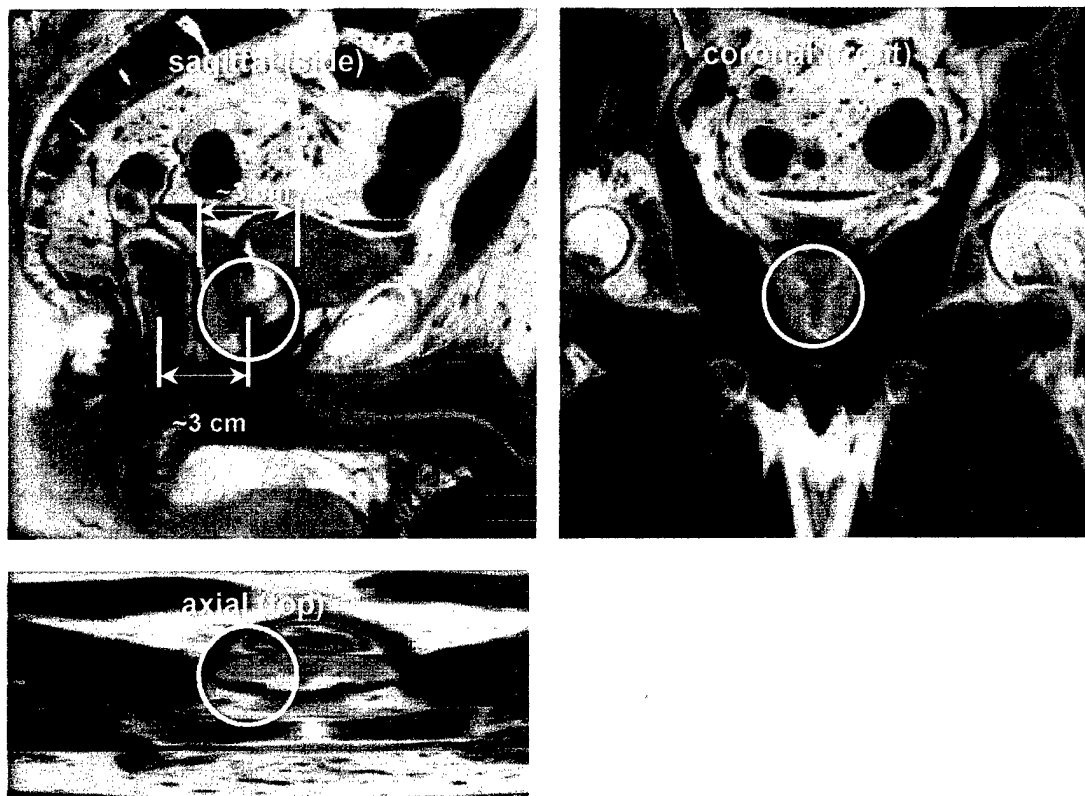


Figure 7. Three views of the anatomy in the neighborhood of the prostate, which is highlighted by the white circle.

Because so much acoustic power is lost on the way to the prostate, the total acoustic power passing through the rectal wall needs to be about double the power that goes through the prostate. But at the same time, the power per area near the rectum must not be greater than the power per area at the prostate in order to avoid overheating the rectal wall. Therefore, if the prostate is to be heated all at once so that the treatment is economical and reasonably comfortable for the patient, the transducer must have an area about a factor of two larger than the cross sectional area of the prostate.

One approach to heating the entire prostate would be to construct a 2-D steerable planer array. By quickly moving the focus of the beam over the entire prostate, heat can be deposited as needed to bring the prostate to the desired uniform temperature. As long as the beam moves around quickly enough (a few milliseconds per spot) the temperature fluctuations from the temporally uneven heating will be negligible. However, the need for a large transducer operating in the 1-2 MHz range poses a problem for a 2-D planer array. The steering angle from the elements of the array to the various regions of the prostate is quite large, especially for elements on the periphery of a large transducer where the angle can be as much as  $65^\circ$ . To allow the beam to be steered over such a large angle, the elements must be small compared to a wavelength, approximately 0.86 mm.

To fill the total transducer area with such small elements requires 2400 individually wired elements, making it difficult to construct a practical probe.

An approach to lowering the total number of elements that was being considered at the time of last year's report was to give up planner construction techniques and individually aim elements toward the center of the prostate. This would reduce the angle over which each individual element would have to radiate sound allowing for fewer, larger elements. But the range of angles is still large enough as to require 1100 elements. They would still need to be individually wired and driven with different phases to quickly steer the focus to any spot in the prostate.

During this reporting period, however, a variation on the first year's work was found that is much simpler and looks promising. The idea of individually aiming elements is taken further to use relatively few larger elements. The elements are several wavelengths across so that each one forms a collimated beam on its own. The beams are aimed such that each element is responsible for heating a different portion of the prostate. There is no electronic steering of the array. Instead, incoherence between the beams is maximized by driving neighboring elements with slightly different frequencies. As shown in Fig. 8, the present design is to use 44 elements arranged in a honeycomb-like pattern. The elements are split into three groups—colored red, green and blue in the figure. Each group is driven at a different frequency in the 1-2 MHz band, nominally three frequencies near 1.5 MHz. Each element is 3.2 mm in diameter and sits in a 3.3 mm hole machined into a substrate at the desired angle for that element. In all there are only three small coaxial leads that need to pass into the rectum to power the three groups, contributing to patient comfort and simplicity of the driving electronics

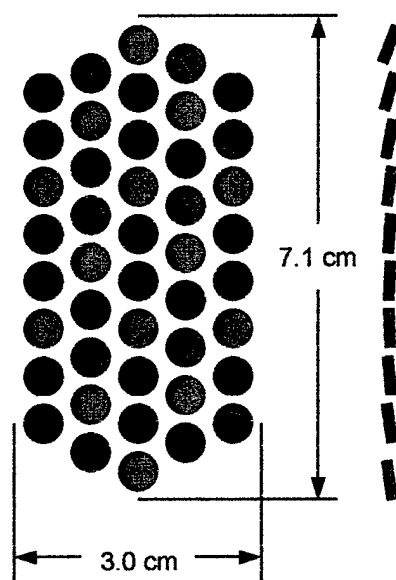


Figure 8. Plan and side views of a Fresnel-lens-like transducer, showing 44 individually aimed circular elements broken into three interspersed groups.

This concept has been subjected to simulations. The complex acoustic pressure beam pattern for a single circular 3.2 mm piston element driven at 1.5 MHz is calculated

and stored in a lookup table. Wave propagation is assumed to take place in a homogenous medium with absorption taken to be an average of values found in the literature for the tissue types that are in the neighborhood of the prostate. The calculated beam pattern is valid in the near, transitional and far field regimes. A table of the transducer element positions, aiming directions, and group number is then constructed. These values can be iteratively changed for simulating different probe configurations. Separately, for each of the three groups of elements, the beams of sound radiating from that group's elements are projected into a large three dimensional space and allowed to interfere with each other. The real part of the complex pressure for the first group—the “red” elements of Fig. 8—is shown in Fig. 9. This figure can be interpreted as a snapshot of the sound field for one of the three frequencies, red showing the positive pressure swing and blue showing the negative pressure swing. Similar calculations and plots are made for the other three frequencies as well, but are not shown. The position of the sagittal, coronal, and axial slices can be changed interactively to help visualize and study the 3-D results, which works out well. Slices through the center of the prostate, indicated by the circle, are what is being shown in the figure.

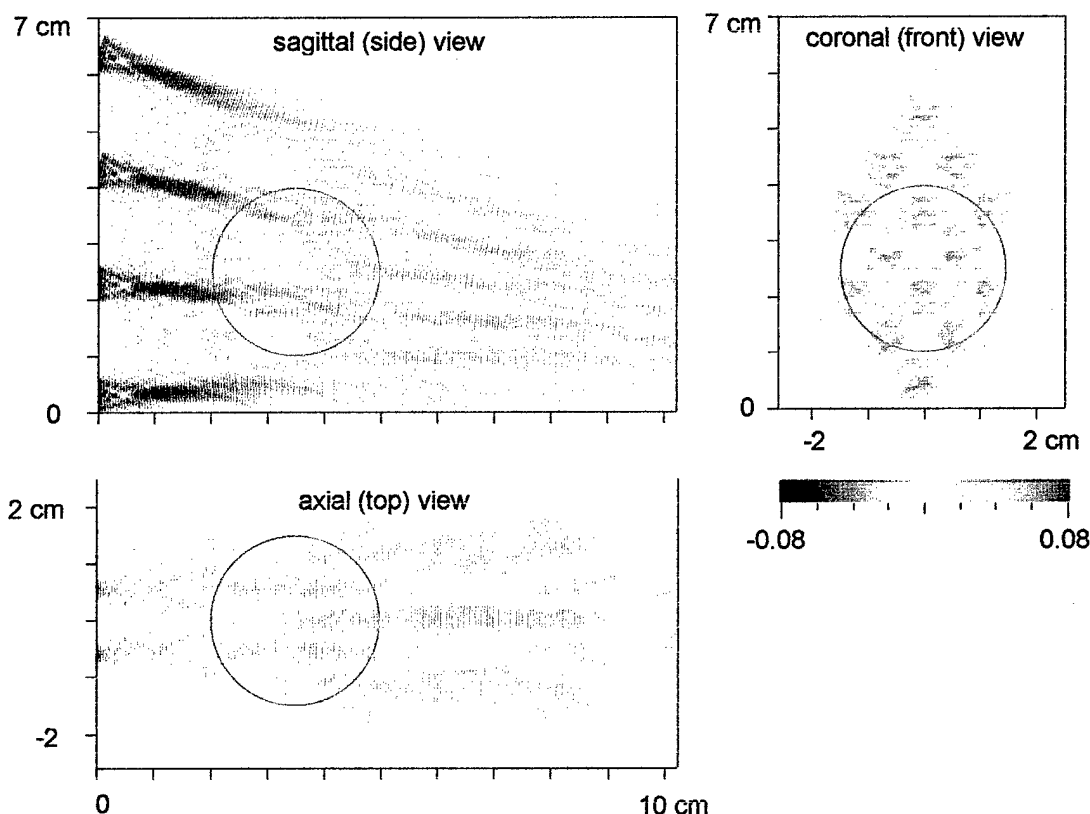


Figure 9. Real part of the complex acoustic pressure from the first group of elements (arbitrary pressure units). The transducer is on the left edge of the sagittal and axial views. The prostate is positioned at the circle.

The deposition of heat is assumed to be proportional to the square of the magnitude of the pressure wave. Although the acoustic fields at the three frequencies interfere independently of each other, their contributions to the heating add together. The beams are aimed to minimize interference within one group of elements of the same frequency, while being aimed such that the heating from each of the three groups compliments the others, filling in the spaces the others miss. The contribution to the heating for the first group is shown in Fig. 10, which is a plot of the square of the magnitude of the complex pressure wave for the first frequency. The depletion of sound that occurs from attenuation and beam spreading is compensated by the converging of the beams toward the far side of the prostate (away from the rectum). More elements point toward the far side of prostate to make sure it is heated as much as the near side.

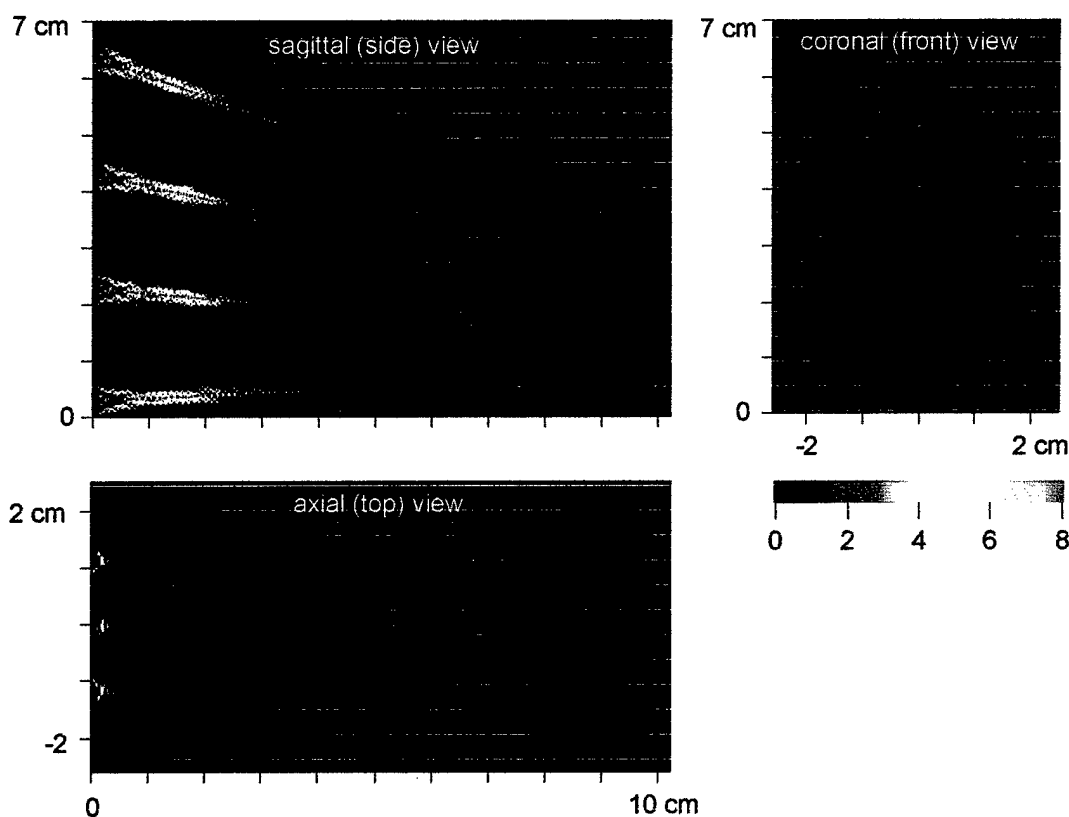


Figure 10. The magnitude squared of the acoustic pressure field, proportional to the heat deposition, of the first group of elements (arbitrary pressure squared units).



The bioheat transfer equation (BHTE)<sup>3</sup>, is used to calculate the temperature rise  $T$  from the heat deposition per unit volume  $q$ , which is taken to be proportional to the pressure amplitude squared. The thermal conductivity  $\kappa$ , the blood perfusion rate  $w$  and

$$\rho c_p \frac{\partial T}{\partial t} = \kappa \nabla^2 T - w c_p T + q,$$

the heat capacity of blood  $c_p$  together define a characteristic length  $\delta$  given by

$$\delta = \sqrt{\frac{\kappa}{w c_p}} = 5.25 \text{ mm},$$

using literature values for  $\kappa$ ,  $w$ , and  $c_p$ . In the steady state the left hand term of the BHTE is zero. The remaining terms are Fourier analyzed, filtered in the wavevector  $k$  space, and inverse Fourier transformed to give the temperature rise

$$T = (\text{const.}) \mathfrak{F}^{-1} \left[ \frac{1}{1 + \delta^2 k^2} \mathfrak{F}(q) \right],$$

which is essentially the convolution, or blurring, of the heating  $q$  over a length scale  $\delta$ , the result of which is shown in Fig. 11. It can be seen that the region within the prostate is predicted to be quite uniform in temperature, but that there are serious hot spots on either side of the prostate.

The hot spots between the transducer and the prostate are caused by the contraction of an acoustic beam in the near field of a circular source. The problem is not as bad as it might seem, however, because the first centimeter or so of propagation from the transducer face will be through chilled water, held in a condom in the rectum, rather than in tissue, and so the hot spot will not do any damage there. The chilled water should also protect the rectal wall and tissue that is one or two characteristic lengths  $\delta$  deep into the body, about 5-10 mm. Nevertheless, the hot spots come too close to the prostate to be assured that important tissue is not being killed. It remains a task for 2004 to simulate the use of a reduced element size, with an increased number of elements, which shortens the near field regime and should bring the hot spots into the safe region under the influence of the chilled water.

The hot spots on the opposite side of the prostate are caused by interference between the overlapping beams of sound within each of the three frequency groups. For some reason that is not yet understood, these regions of constructive interference for each of the groups happen to land on top of each other. Another task for 2004 will be to find a way to mitigate this problem. The positions of these bands of constructive interference should depend on the frequency, in which case they should be able to be moved around to different positions, equalizing the heating, by quickly sweeping the drive frequency for the transducers. Another possibility is to break up the transducers into more than three groups of frequencies. A third possibility is to break the circular elements into partitions, as shown in Fig. 12. The beam angles can be swept vertically by varying the relative phase of the drive on two partitions, or the beam angles can be gyrated circularly by using three partitions. This would bring the number of leads entering the rectum to 6 or 9, respectively, which is still far less than is needed for a traditional phased array.

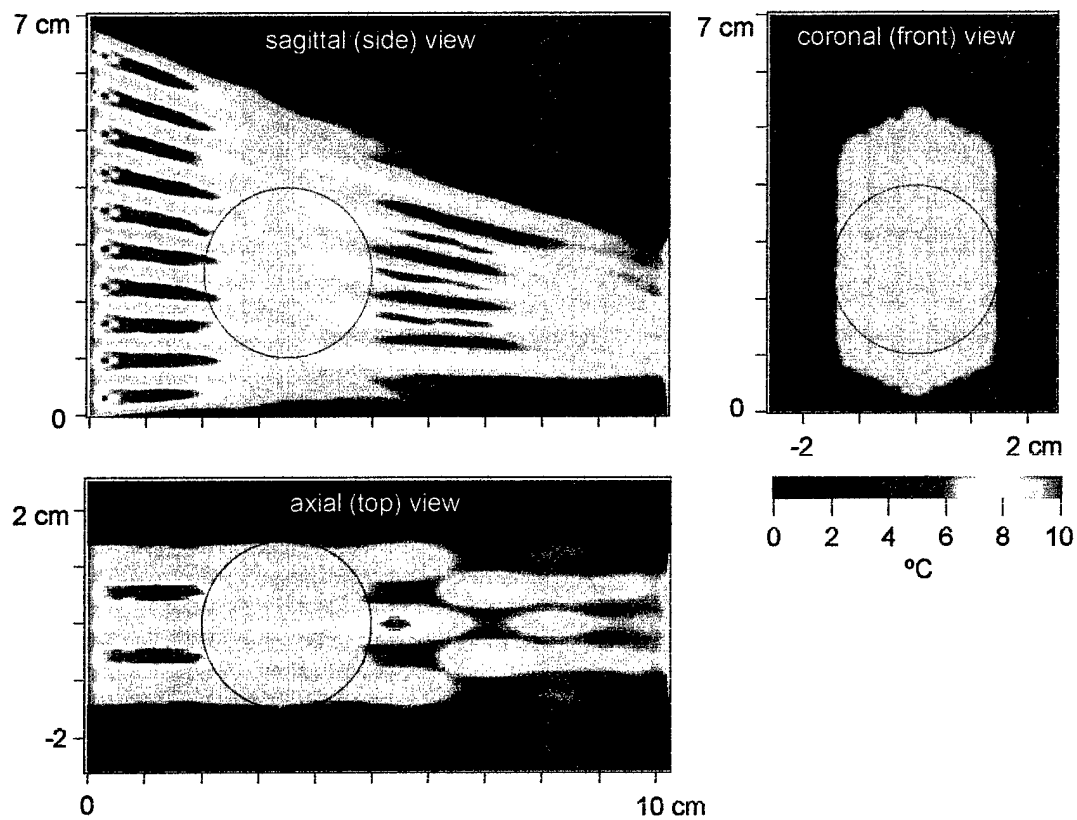


Figure 11. The temperature rise due to heating from all the elements.



Figure 12. Partitioning of an element into two (left) or three (right) segments to allow electronic steering of the beams.

### 2.2.3 Wave Propagation Using the *k*-Space Method

In order to optimize and control the driving parameters of the phased array to uniformly heat the entire prostate, an anatomically and acoustically accurate model was constructed utilizing the data from the Visible Human Project <sup>5</sup>. The appropriate photographs were located and downloaded into local storage area in order to collect the required three-dimensional (3D) prostate model. Slice number 1900 is shown in Fig. 13; the prostate gland is shown bounded on the upper side by the rectum and by the bladder on the lower side; an added blue color is shown filling the cavity of the rectum. A sheet of connective tissue is shown surrounding the rectum and embedded in a triangular shaped fat area. Forty seven slices were chosen that include the prostate gland. A 359 x 359 x 47 point three-dimensional human prostate model is shown in Fig. 14 which represents a volume of 89.5 x 89.5 x 46.0 mm<sup>3</sup> with 1 mm slice thickness. The 1 mm sampling thickness of the Visible Human Project data was a poor choice for simulation of wave propagation of megahertz waves—for this reason the model was modified to reduce this thickness to 0.25 mm. Figure 15 shows the creation of three extra averaged slices between each consecutive one. The centered slice was created by averaging the outer slices as shown in the figure; both slices #1880 and #1881 were averaged to produce another slice located 0.50 mm away from them. Two extra slices, located at 0.25 mm and 0.75 mm from slice #1880, were produced by averaging the centered averaged slice with the outer ones.



Figure 13. Photograph showing slice #1900. The prostate gland is surrounded by skeletal and smooth muscles; the rectum is located above the gland while the bladder is beneath it.

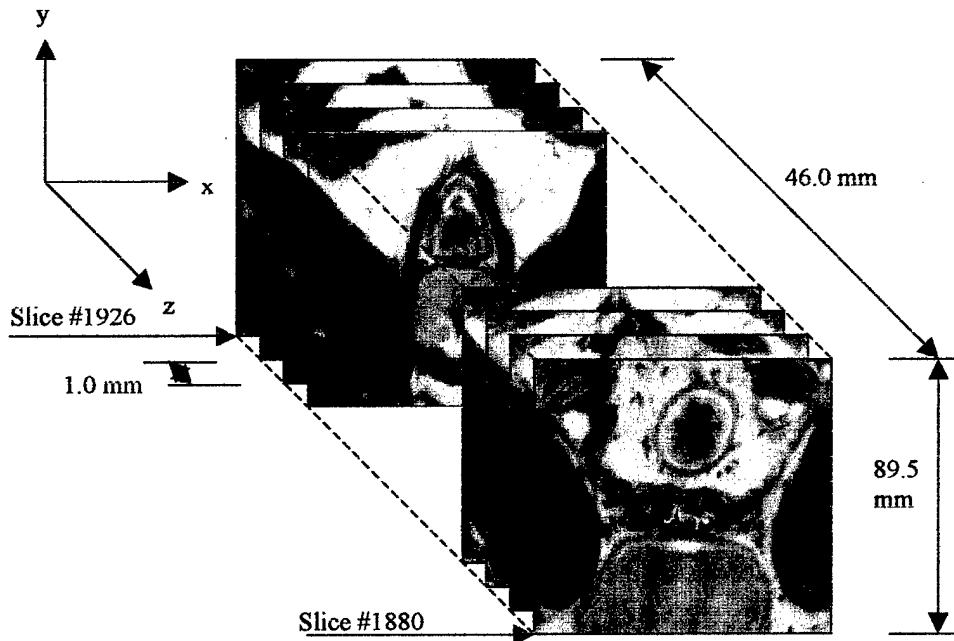


Figure 14. The three-dimensional photograph of the prostate showing 47 slices of  $89.5 \times 89.5 \text{ mm}^2$  dimension with 1.0 mm distance between each slice. The model starts with slice #1880 and ends with slice # 1926.

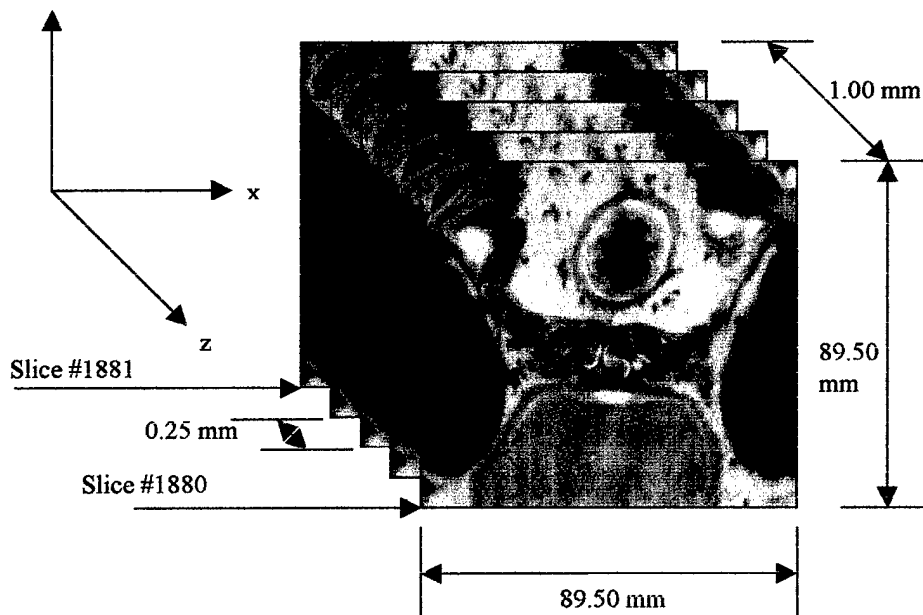


Figure 15. Three averaged slices are shown between slices 1880 and 1881 to reduce the distance between consecutive slices to 0.25 mm. The centered slice was produced by averaging the outer images, while the other two slices were produced by averaging the centered averaged slice with the outer ones.

A 3-D acoustical model was created based on the optical parameters of each pixel in the actual and averaged images. As shown in Fig. 13, the surrounding tissue of the prostate gland consists of fat, muscle and connective tissues. The prostate gland consists of compound tubular-alveolar glands embedded in a mass of smooth muscle and dense connective tissue<sup>6</sup>. The 3-D acoustical model uses the optical parameters that define the fractional fat, connective, glandular and muscle content of each pixel. Table 1 summarizes the actual acoustical values of these tissues when measured at 37°C. The 3-D photographic data was used to create three additional sets of 3-D acoustical data, which are the sound speed variation, density distribution and absorption parameters. Sound speed of each pixel was estimated based on the fractional optical constituents of water, muscle, fat and connective tissues<sup>7</sup> while mass density and absorption parameters were mapped using empirical linear relations with sound speed.

Table 1. The acoustical parameters (i.e. sound speed, density and absorption) of connective tissue, muscle, fat and water, determined at 37°C.

Tissue type	Sound Speed (mm/ $\mu$ s)	Density (g/cm <sup>3</sup> )	Absorption @ 1.2 MHz (dB/mm)
Connective	1.613	1.120	0.1030
Muscle	1.580	1.050	0.0890
Fat	1.450	0.950	0.0340
Water	1.524	0.992	0.0003

Each slice in the original photographic data, which represents a JPEG type image, was converted to a HSV (hue, saturation and value) image in order to calculate the amount of each tissue constituent for each pixel. The volumetric image (Figs. 14 and 15) was mapped to sound speed, density and absorption, as shown in Figs. 16 for slice #1908. For example, Fig. 16(b) shows the sound speed mapping of slice #1908. The sound speed varies through the soft tissue of that image from about 1.4 to 1.6 mm/ $\mu$ s. The blue-colored material was translated into water, as shown from the color bar that gives a sound speed of 1.5 mm/ $\mu$ s of that area. The skeletal muscle tissue that surrounds the prostate gland is shown to have sound speed of about 1.55 mm/ $\mu$ s. The prostate gland itself was mapped to connective tissue and some fat and muscle tissues. This mapping was found to be consistent with the description of the gland that describes it as tubular and alveolar tissues imbedded in smooth muscle and connective tissues<sup>6</sup>. The rectal wall was translated into muscle and fat tissues as shown in Fig. 16(b). The connective tissue that surrounds the rectum is shown to have a sound speed of about 1.61 mm/ $\mu$ s, which resembles connective tissue as expected. The fat area that surrounds the rectum is shown to have some areas that contain connective tissues scattered all over that area. Sound speed of that fat area is found to vary from 1.4 to 1.5 mm/ $\mu$ s. The translation was acceptable when compared to the data found in Table 1.

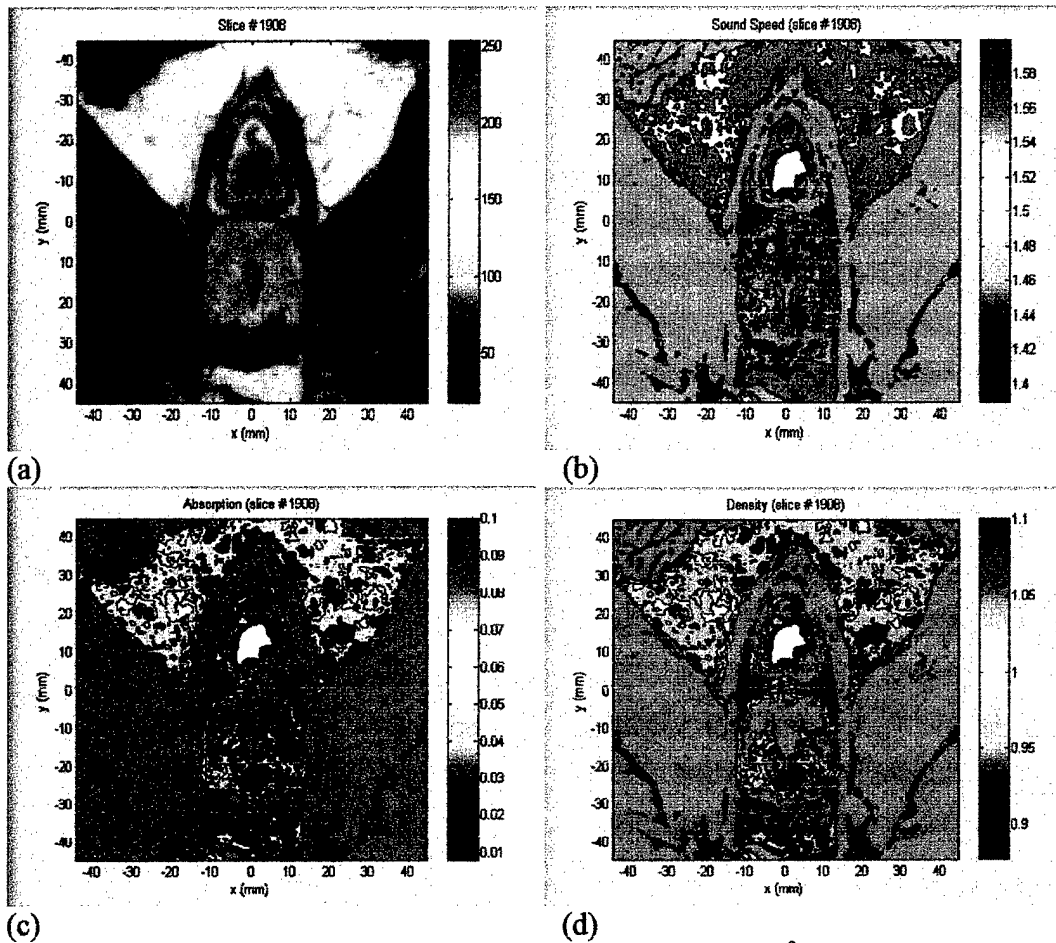


Figure 16. The acoustical mapping of (a) slice #1908 to (b) density in  $\text{g/cm}^3$ , (c) absorption in nepers/mm and (d) sound speed in  $\text{mm}/\mu\text{s}$ . The added blue colored material in the (a) rectum translated to about  $1.00 \text{ gm/cm}^3$ ,  $0.06 \text{ nepers/mm}$  and  $1.54 \text{ mm}/\mu\text{s}$  representing density, absorption and sound speed, respectively. Fat and muscle, as shown in the slice, were translated with good agreement to its acoustical parameters, as compared to Table 1.

Figure 16(c) shows the density variations through slice #1908. The density is found to vary from about  $0.9$  to  $1.1 \text{ gm/cm}^3$ . When compared to the sound speed map this figure is found to discriminate each soft tissue accurately and is found to have good agreement for skeletal muscle, fat, connective tissue and water. Figure 4(d) shows the absorption variations of the soft tissue of the same slice. The absorption is found to vary from  $0.01$  to  $0.1 \text{ nepers/mm}$ . The absorption parameters of water, fat, connective and skeletal muscle tissues were found to match those values summarized in Table 1 measured at  $37^\circ\text{C}$ . Comparing the values of sound speed, density and absorption of various tissues in Fig 16(b), (c) and (d), respectively, to the standard values of these soft tissues, a good agreement was found for this mapping over the whole three-dimensional model.

The  $k$ -space method<sup>8,9</sup> was found to be appropriate in simulating wave propagation in inhomogeneous mediums using coarse grids while maintaining accuracy. The linear wave equation was used for this simulation incorporating the mass conservation, momentum conservation and state equations to produce the first order coupled propagation equations<sup>10</sup>

$$\frac{\partial p(x, y, z, t)}{\partial t} + \rho(x, y, z)c^2(x, y, z)\nabla \cdot v(x, y, z, t) = -\alpha(x, y, z)p(x, y, z, t)$$

$$\rho(x, y, z)\frac{\partial v(x, y, z, t)}{\partial t} + \nabla p(x, y, z, t) = 0$$

these two equations produce the linear wave equation as follows:

$$\nabla \cdot \left( \frac{1}{\rho(x, y, z)} \nabla p(x, y, z, t) \right) - \frac{1}{\rho(x, y, z)c^2(x, y, z)} \frac{\partial^2 p(x, y, z, t)}{\partial t^2} = \alpha(x, y, z) \frac{\partial p(x, y, z, t)}{\partial t}$$

which represents the linear wave equation in an inhomogeneous medium with absorption parameters included as a virtual source that depend on the time derivative of the pressure multiplied by a frequency independent absorption factor. In order to use the  $k$ -space method to solve for the propagation of sound, the linear wave equation in an inhomogeneous medium will be simplified to separate the spatially dependent sound speed and density parameters from the second order derivatives of the pressure with respect to spatial and temporal variables. The derivation of the  $k$ -space mathematical model produces:

$$\frac{\partial^2 W(k, t)}{\partial t^2} = k^2 c_0^2 [W(k, t) - V(k, t)] - Q(k, t)$$

where

$$V(k, t) = \mathbb{F} \left[ \left( 1 - \frac{c^2(x, y, z)}{c_0^2} \right) (\psi_i(x, y, z, t) + w(x, y, z, t)) \right]$$

$$Q(k, t) = c_0^2 \mathbb{F} \left[ \sqrt{\rho(x, y, z)} \nabla^2 \rho^{-1/2}(x, y, z) [\psi_i(x, y, z, t) + w(x, y, z, t) - v(x, y, z, t)] \right]$$

A non-standard finite difference approach was used to solve this equation. The discretization of the time derivative term gives:

$$W(k, t + \Delta t) - 2W(k, t) + W(k, t - \Delta t) = 4 \sin^2 \left( \frac{c_0 k \Delta t}{2} \right) \left[ V(k, t) - W(k, t) - \frac{Q(k, t)}{c_0^2 k^2} \right]$$

This  $k$ - $t$  propagator is the key equation to solve for the propagation in an inhomogeneous medium after setting the initial and boundary conditions.

A Fortran 77 program was used to calculate and simulate wave propagation of sound in a 3-D inhomogeneous medium. A  $6.4 \times 6.4 \times 4.6 \text{ cm}^3$  model that has  $257 \times 257 \times 185$  points was prepared for each acoustical parameter (sound speed, density and absorption); these data were read and processed to be compatible with the mathematically

derived model. A tapered absorption boundary layer was inserted into the absorption data set; 25 points were used to create this layer that surrounded the actual model<sup>8</sup>.

A spherical point source that produced spherical waves was placed into the model at the rectum near the absorbing boundary layer to test the model and the numerical method adapted here. It was produced mathematically as a Gaussian source in both space and time spaces. This source was added to the effective sources that resulted earlier from the derivation and simplification of the  $k$ -space method and the addition of the absorption dependent term as well.

The resulting log-scale gray scale image of the wave propagation in the three-dimensional model is shown in Fig. 17.

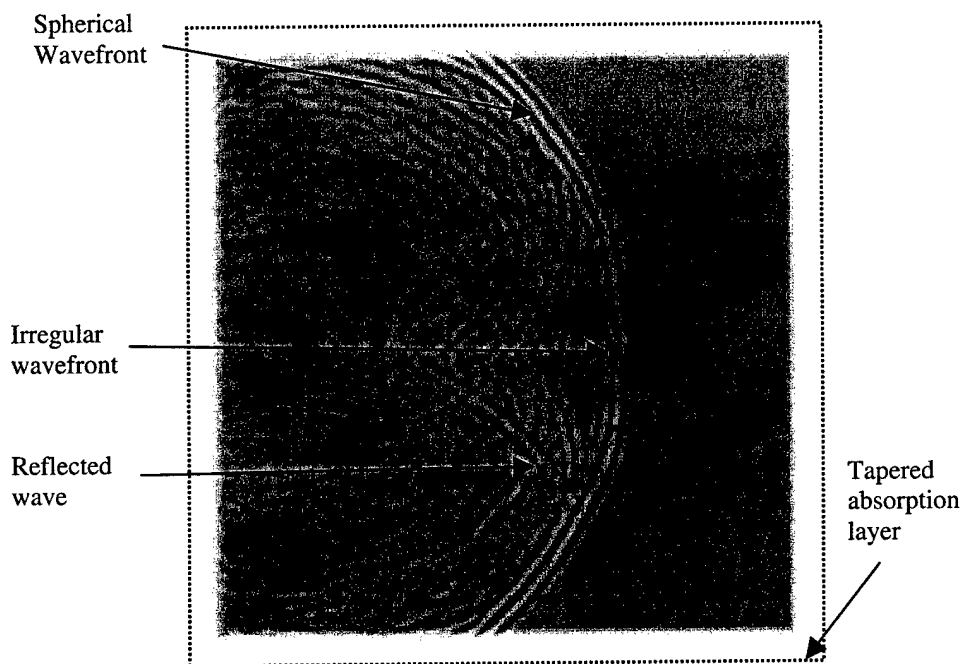


Figure 17. A two dimensional gray scaled image showing a background layer of the absorption distribution through the middle slice of the 3-D prostate model. The tapered absorption boundary layer is shown at the edges with sharp white color. The black dotted line surrounding the image shows the limits of the absorption layer. A spherically propagated wave is shown superimposed on top of a background image of the prostate, showing the wave propagation from left to right through the 3-D prostate model. The scattered wave shown is the result of a spherical compact Gaussian source at the rectum consisting of the three cycles with a frequency of 1.2 MHz. Due to sound speed and density changes throughout this model, the wave front develops an irregular shape while propagating through the urethra area.

The incident wave is shown leading the scattered wavefield that results from propagation in the inhomogeneous medium. The spherical source was located in the rectum five points away from the absorption boundary layer. The multi-layer image in this figure includes the absorption variations through the central slice of the 3-D model as a background. The tapered absorption boundary layer is clearly shown surrounding the whole image. The 3-D  $k$ -space propagation program was designed to create a 2-D gray



scaled image of the wave every 10 milliseconds. These images were then saved as a JPEG image to facilitate their use with Photoshop or any other photo editors. The scattered as well as the incident waveforms are shown and labeled. At the boundaries of the prostate a reflected wave can be seen. Some irregularity of the shape of the wave while crossing the urethra region is also seen. This kind of irregularity will complicate the focusing of sound in such an inhomogeneous medium. However, this figure was produced to test the accuracy of the model and the computational method rather than focusing issue. The inclusion of the phased array as a sound source into this model will allow us to predict and optimize the pressure wavefield for thermal therapy of the prostate.

### 2.3. MRI Thermometry Using the Ultrasound Array; *In Vitro* and *In Vivo* Results

To determine the temporal and spatial temperature from one of the prototype multielement phased arrays, both *in vitro* and *in vivo* experiments were performed using magnetic resonance imaging (MRI). Ten *in vitro* experiments were conducted with bovine muscle phantoms using the intracavitary ultrasonic probe. The ultrasonic probe was driven by a multi-channel ultrasound phased-array power amplifier (Advanced Surgical System Inc., Tucson, AZ), which is capable of delivering 60W per channel continuously from 1.1 MHz to 1.8 MHz. The outer active surface of the ultrasonic probe is a latex condom filled with circulating water, which forms a "bolus" of water that shows up in the MR images. The tissue was coupled to the water bolus with ultrasound gel (Clear Image, Sonotech, Inc., Bellingham, WA). The bovine muscle, as well as the degassed water circulated through the bolus, was kept at room temperature to impose a constant temperature at the interface of the ultrasonic probe and the phantom. One fiber optic probe was inserted into the tissue using a 2.1 x 133 mm catheter (Angiocath, Becton, Dickinson and Company, Franklin Lakes, NJ) to monitor the tissue temperature at the hot spot. Two other fiber optic probes were placed at the surface of the muscle facing the ultrasonic probe to monitor for overheating at the future location of the rectal wall.

A temperature increase of 8°C at the hot spot simulated a temperature rise from 37°C to 45°C. The sonication time was 30 minutes, with the initial power set to 0.1W/channel. The tissue was allowed to return to room temperature before each experiment. The temperatures at the hot spot and the surface of the tissue, and the electrical power to each channel were recorded. During *in vitro* experiments, the tissue was heated initially from room temperature (~25°C) to 33°C (8°C above room temperature). The temperature change within each phantom was monitored to follow the target temperature evolution (Fig. 18). Very similar results were obtained for the ten experiments with no overshoot, no oscillation, and 10 minutes rise time. The maximum temperature at the surface of the tissue did not exceed 30°C which is desirable for the future safety of the rectal wall.

Five New Zealand white rabbits (3-4 kg, male) were used for 10 separate *in vivo* hyperthermia experiments. The rabbits were anaesthetized and later euthanatized by a protocol approved by the Penn State Institutional Animal Care and Use Committee (IACUC). A combination of ketamine (40mg/kg intramuscularly, Fort Dodge Animal Health, Fort Dodge, IA) and xylazine (10mg/kg intramuscularly, Phoenix Scientific, Inc.,

St. Joseph, MO) were injected to anaesthetize the animals. After shaving the thigh, hair removal cream was applied to the skin to eliminate any remaining hair. The rabbit's vital signs (ECG, SpO<sub>2</sub>, HR) were monitored by SurgiVet monitoring system (SurgiVet, Inc., Waukesha, WI). The *in vivo* experiments were performed in the same manner as the *in vitro* experiments. The results while using a fiber optic temperature probe to monitor the temperature change in the *in vivo* rabbit thigh muscle is shown in Fig. 19. For these results, the temperature profile indicates no oscillation, no overshoot and a fast rise time for these hyperthermia experiments.

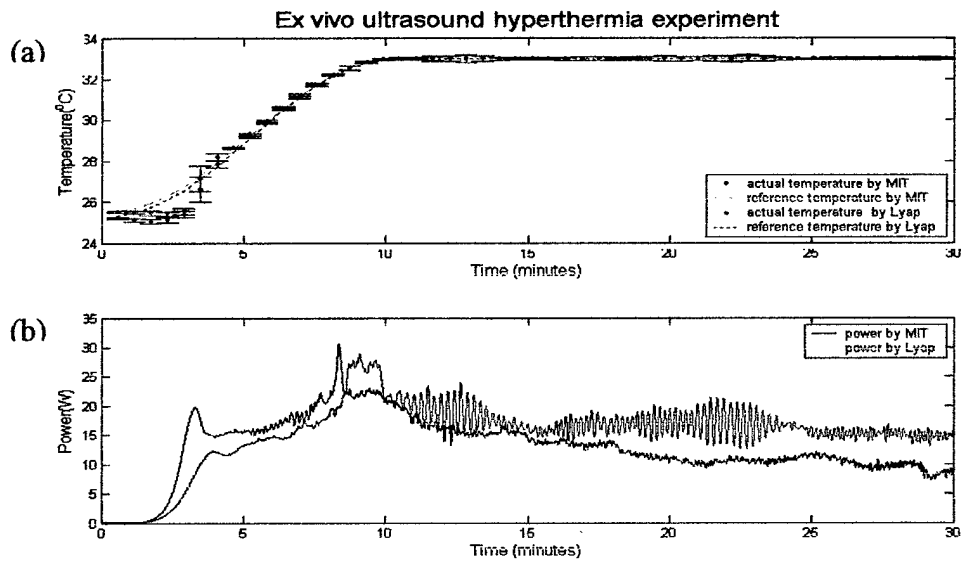


Figure 18. *In vitro* ultrasound hyperthermia experiment using bovine muscles. (a) Temperature evolution and target temperature trajectory. (b) Electrical power transmitted to the applicator.

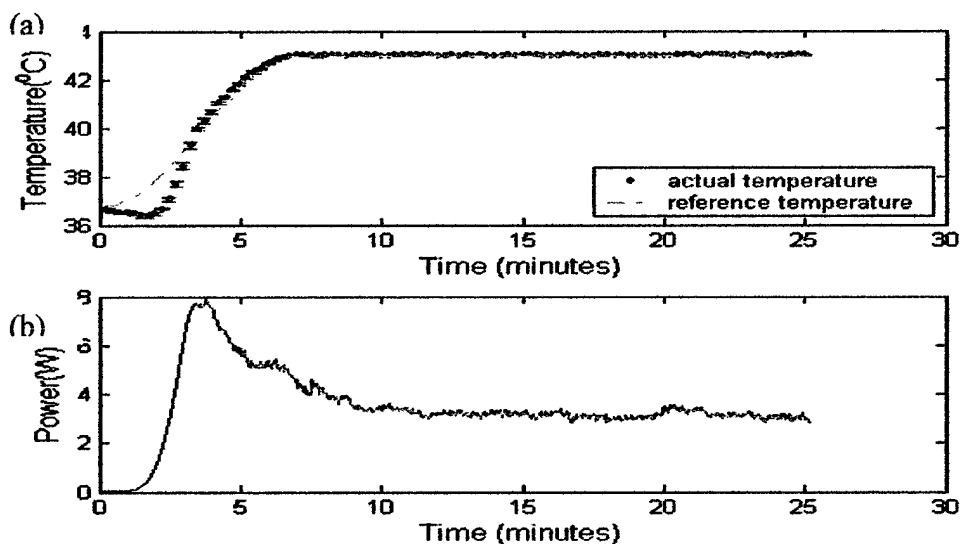


Figure 19. Typical *in vivo* ultrasound hyperthermia experiment results using rabbit thigh muscle. The (a) temperature elevation and reference temperature trajectory is plotted as a function of time over 25 minutes. From the amplifier system, the (b) electrical power transmitted to the applicator is also plotted over the same time.

Using noninvasive MRI thermometry, nine additional *in vitro* ultrasound hyperthermia experiments were conducted using bovine muscles within a 3 Tesla Bruker S-300 MRI scanner at the Penn State College of Medicine heated by the ultrasound array. Thermometry data consisted of MR temperatures in a region of interest (ROI) that was selected from the tissue from pre-treatment images. The proton resonant frequency (PRF) shift was evaluated by using a spoiled gradient echo (SPGR) sequence with the following imaging parameters: TR = 100 ms, TE = 15 ms, flip angle =  $30^\circ$ , data matrix 64 x 64, field of view (FOV) = 16 x 16 cm, slice thickness = 8 mm and bandwidth = 61.7 kHz. These parameters were chosen to maximize the temperature dependent phase shift, while maintaining a high temporal resolution. A baseline scan was acquired before ultrasound heating and subsequent temperature measurement scans were obtained every 19.7 seconds. Phase subtraction was conducted on-line in real-time to calculate the PRF shift. The temperature elevation was obtained by averaging temperatures within a 4 x 3 pixel region located at least 1 cm above the bolus-tissue interface and using a temperature dependence of the proton phase shift for muscle of  $-0.00909 \text{ ppm}/^\circ\text{C}$ .

Using rabbit thigh muscle, *in vivo* animal experiments were conducted using a similar procedure as the bovine muscles phantom experiments with the animal anesthetized by the combination of ketamine (40 mg/kg) and xylazine (10 mg/kg). Figure 20 is an axial view of the MR temperature map, showing the rabbit thigh muscle above the ultrasound array surrounded by its water filled bolus. Both the animal and phantom experiments used head-sized birdcage coil with a length of 29 cm and inner diameter of 26 cm. For rapid hyperthermia heating, the time constant of the target temperature was selected to be less than 2 minutes for a total experimental time of 25 minutes.

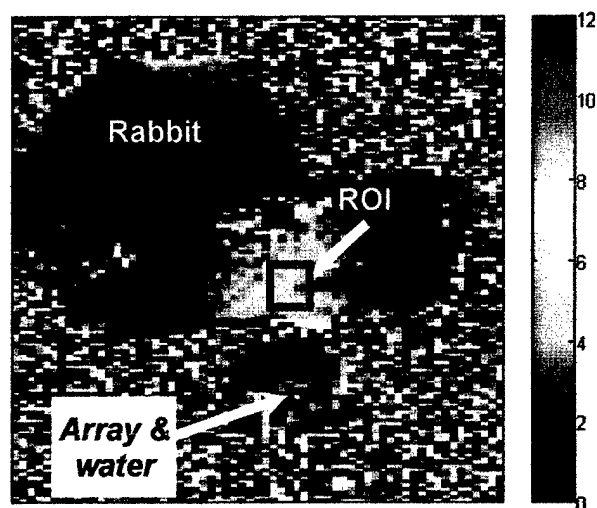


Figure 20. The temperature map (temperature change indicated by the color bar on the right of the figure in  $^\circ\text{C}$ ) of the axial view of the MRI-guided *in vivo* ultrasound hyperthermia experiments setup.

Ultrasound hyperthermia results have been demonstrated for both the *in vitro* and *in vivo* experiments. Fig. 21(a) shows the results of the nine *in vitro* experiments, plotting the target temperature (solid line) and the MR temperatures with a steady state temperature of  $38^\circ\text{C}$ . Starting at an initial phantom temperature of  $28^\circ\text{C}$ , the temperature reaches the steady state within 6.0 minutes; deviation from the target profile was no

greater than  $\pm 1.37^{\circ}\text{C}$ . Similar to the *in vitro* results, *in vivo* temperature can be seen in Fig. 21(b) where the rabbit thigh muscle was heated initially from  $36.5^{\circ}\text{C}$  for 25 minutes. For this experiment the target temperature was  $44.5^{\circ}\text{C}$  and was achieved in 8.0 minutes. The maximum variation from the desired temperature profile was  $-3.9^{\circ}\text{C}$ ; after reaching steady state, tissue temperature was maintained at  $44.5^{\circ}\text{C} \pm 1.2^{\circ}\text{C}$ .

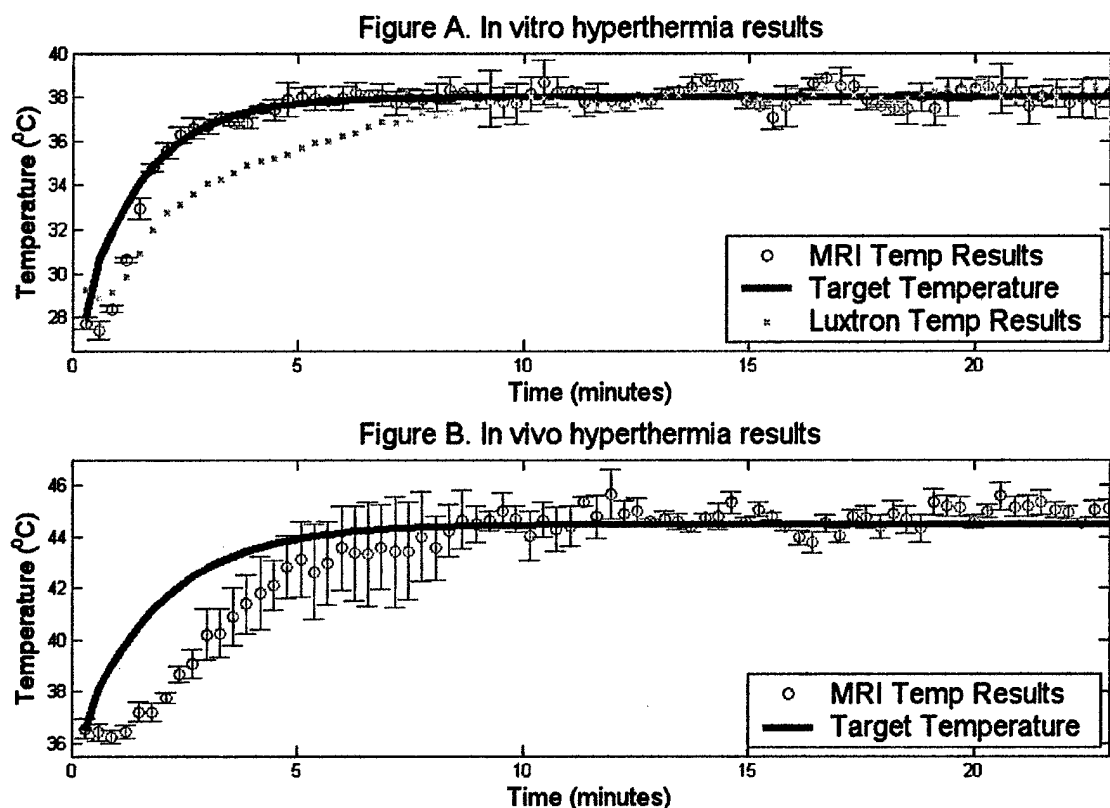


Figure 21. Example (a) *in vitro* and (b) *in vivo* ultrasound hyperthermia experiment temperature rise results in an MRI. The (a) temperature elevation and reference temperature profile is plotted for 25 minutes of ultrasound exposure using bovine muscle as a tissue phantom. An example (b) *in vivo* rabbit hyperthermia temperature profile is also shown.

These results demonstrated that the proton resonant frequency shift is not severely influenced by physiological changes of tissue during a 25 minute hyperthermia treatment. Therefore, the results continue to support that proton resonance frequency shift is suitable for monitoring the temperature elevation during hyperthermia treatments.

### 3. KEY RESEARCH ACCOMPLISHMENTS:

- Transducer constructed and implemented with clinical applicator body design for a working multielement array
- Continuation of the optimization of the array design strategy through modeling the tissue characteristics using:
  - Nonlinear acoustic propagation
  - "Fresnel-lens-like" Transducer with aimed, incoherent beams of sound
  - Wave propagation using the  $k$ -space method
- MRI Thermometry experiments using the hyperthermia ultrasound array
  - In vitro results
  - In vivo results

#### 4. REPORTABLE OUTCOMES:

Funding from this award has been used to produce a published manuscript, manuscripts in progress, conference proceeding and has been sited in several invited talks. In all publications and invited talks using the data resulting from this grant, the Department of Defense Congressionally Directed Medical Prostate Cancer Research Program has been gratefully acknowledged. Copies of the manuscripts, proceedings and presentations are included in the appendix.

##### Manuscripts

Saleh, K. and Smith, N.B., Two Dimensional Array Design for Tissue Ablation for Treatment of Benign Prosthetic Hyperplasia, *International Journal of Hyperthermia*, 2004, (20) 1, pp 7-31.

##### Manuscripts in progress

Al-Bataineh. O.M., Keolian, R.M., Sparrow, V.W., Smith, N.B., "Optimized Hyperthermia Treatment of Prostate Cancer Using a Novel Intracavitary Ultrasound Array," *Journal of Acoustical Society of America*, (to be submitted January 2004).

Keolian, R.M., Sparrow, V.W., Al-Bataineh, O.M., Smith, N.B. "Heating the prostate with aimed, incoherent beams of sound", *Journal of Acoustical Society of America*, (to be submitted July 2004).

##### Presentations

Al-Bataineh. O.M., Smith, N.B., Keolian, R.M., Sparrow, V.W., Optimized Hyperthermia Treatment of Prostate Cancer using a Novel Intracavitary Ultrasound Array, 146th Meeting of the Acoustical Society of America, 10-14 November 2003, Austin, Texas.

Keolian, R.M., Al-Bataineh, O.M., Smith N.B., Sparrow. V.W., , Harpster, L.E.. 2003. A "Fresnel-Transducer" for Prostate Hyperthermia Treatment *Acoustical Society of America*, 146th Meeting of the Acoustical Society of America, 10-14 November 2003, Austin, Texas.

Saleh, K. and Smith, N.B., " Design and evaluation of a 63 element 1.75-dimensional ultrasound phased array for treating benign prostatic hyperplasia," *Acoustical Society of America*, 146th Meeting of the Acoustical Society of America, 10-14 November 2003, Austin, Texas.

Sun L., Al-Bataineh O., Collins C., Smith M.B., and Smith, N.B. Fast adaptive control for MRI-guided ultrasound hyperthermia treatment for prostate disease: in vitro and in vivo results, *International Society of Magnetic Resonance in Medicine (ISMRM) Twelfth Scientific Meeting & Exhibition*, Kyoto, Japan, 15-21, May 2004 (*submitted*).

Smith, N.B. "Therapeutic Applications of Ultrasound: Treatment of Prostate Disease and Noninvasive Drug Delivery", Invited seminars to:

- University of Illinois Urbana Champaign, Bioacoustics Research Laboratory Seminar Series, March 4, 2003
- University of Illinois Chicago – Department of Bioengineering, May 2, 2003
- University of Virginia - Department of Biomedical Engineering, Nov. 7, 2003
- Penn State University, College of Medicine Hershey, Nov. 11, 2003.

## 5. CONCLUSIONS:

For this research in the treatment of prostate disease, the overall goal is produce an ultrasound device to treat cancerous tissue using hyperthermia. Intracavitary ultrasound offers an attractive means of noninvasive localized hyperthermia treatment for prostate cancer with reduced side effects compared to competing modalities. For effective hyperthermia treatment, the goal is to uniformly heat the prostate to 43°C for 30-60 minutes. To achieve this goal, the clinical ultrasound device has been constructed and is currently under critical evaluation in clinical MRI. The transducer was designed such that ultrasonic wavefields were optimized to specifically target prostate tissue, resulting in uniform hyperthermia treatment within the prostate and minimal effects to surrounding tissue.

The second year of this three year research project was focused on the construction of the array based on our Year 1 results of computer simulations of the ultrasound energy interactions with the prostate. In accordance with the specific aims and timetable within our original proposal, the three areas examined during this year were: (a) transducer construction (b) optimization of the transducer array design for easy modifications during the third year, and (c) MRI thermometry experiments (*in vitro* and *in vivo*) using the hyperthermia ultrasound array. Previously, much research in this area has treated the prostate and surrounding tissue as homogeneous media. For our currently constructed applicator, supplementary simulations are used to refine our array pattern and can be easily and quickly implemented in the applicator based on our MRI thermometry results. These simulations take into account the inhomogeneity of the prostate to produce a uniform heating pattern using k-space propagation and application of the non-linear bioheat transfer equation to determine the optimal thermal treatment.

Using the intracavitary array transducer, noninvasive magnetic resonance imaging thermometry methods were used to determine the spatial and temporal temperature field pattern from the ultrasound using initially bovine tissue as a phantom and *in vivo* rabbit thigh muscle. The third year goals will use the optimized array to heat the prostate of a canine while the temperature change is monitored using MRI to determine the clinical efficacy of this device. To date, there are no deviations from the original research plan and this research is progressing on schedule.

So what is the impact of this research? Previous and recent clinical studies of hyperthermia using intracavitary ultrasound arrays have shown promising results for the clinical treatment of prostate cancer<sup>2;11</sup>. With the increasing aging population within the US, there are increasing incidents of prostate cancer. With an estimated 37,000 deaths per year, prostate cancer is the second leading cause of cancer death in men. Although age is perhaps the most important risk factor, the incidence and mortality rate is twice as high for African-American men as for Caucasian men<sup>12;13</sup>. Moreover, the knowledge gained from this research can further be applied to noninvasive treatment of other cancers such as breast cancer or cancers of the liver or kidney.

## 6. REFERENCES (*Science* format)

### Reference List

1. Hurwitz, M. D., Kaplan, I. D., Svensson, G. K., Hynynen, K. H., and Hanson, J. L. Preliminary report of the feasibility and patient tolerance of a novel transrectal ultrasound hyperthermia system for the treatment of prostate cancer. 21. 1999. 4-8-1999.
2. Hurwitz, M. D., Kaplan, I., Svensson, G. K., Hansen, J., and Hynynen, K. H. Feasibility and patient tolerance of a novel transrectal ultrasound hyperthermia system for treatment of prostate cancer. *International Journal of Hyperthermia* 17(1), 31-37. 2001.
3. H. H. Pennes, *Journal of Applied Physiology* 1, 93-122 (1948).
4. M. F. Hamilton and D. T. Blackstock, *Nonlinear Acoustics* (Academic Press, San Diego, 1998), pp. pp. 54-55.
5. National Library of Medicine (US) Board of Regents. Electronic Imaging: Report of the Board of Regents. NIH Publication , 90-2197. 1990.
6. E. H. Maurieb, *Human Anatomy & Physiology* (Addison Wesley Longman, New York, ed. 5th, 1999).
7. Mast, T. D. Empirical relationships between acoustic parameters in human soft tissues. *Acoustics Research Letters Online* 1(2), 37-42. 2000.
8. Mast, T. D., Souriau, L.P., Liu, D., Tabei, M., Nachman, A.I., and Waag, R. C. A k-space method for large-scale models of wave propagation in tissue. *IEEE Trans.Ultrason., Ferroelect., Freq.Contr.* 48(2), 341-354. 2001.
9. Tabei, M., Mast, T. D., and Waag, R. C. A new k-space method for coupled first-order acoustic propagation equations. *Journal of the Acoustical Society of America* (submitted). 2001.
10. T. D. Mast, L. M. Hinkelman, L. A. Metlay, M. J. Orr, R. C. Waag, *J.Acoust.Soc.Am.* 106, 3665-3677 (1999).
11. H. Fosmire et al., *International Journal of Radiation Oncology Biology and Physics* 26, 253-259 (1993).
12. P. A. Wingo, L. A. Ries, S. L. Parker, C. W. Heath, *Cancer Epidemiol.Biomarkers Prev.* 7, 271-282 (1998).
13. R. T. Greenlee, T. Murray, S. Bolden, P. A. Wingo, *CA Cancer J.Clin.* 50, 7-33 (2000).



## 7. APPENDICES:

List of items in appendix:

### Manuscripts

Saleh, K. and Smith, N.B., Two Dimensional Array Design for Tissue Ablation for Treatment of Benign Prosthetic Hyperplasia, *International Journal of Hyperthermia*, 2004, (20) 1, pp 7-31.

### Manuscripts in progress

Al-Bataineh. O.M., Keolian, R., Sparrow, V., Smith, N.B., "Optimized Hyperthermia Treatment of Prostate Cancer Using a Novel Intracavitary Ultrasound Array," *Journal of Acoustical Society of America*, 2004 (to be submitted January 2004).

Keolian, R., Sparrow, V., Smith, N.B. "Heating the prostate with aimed, incoherent beams of sound", *Journal of Acoustical Society of America*, (to be submitted July 2004).  
(not included in the appendix)

### Presentations:

Al-Bataineh. O.M., Keolian, R., Sparrow, V., Smith, N.B., Optimized Hyperthermia Treatment of Prostate Cancer using a Novel Intracavitary Ultrasound Array, 146th Meeting of the Acoustical Society of America, 10-14 November 2003, Austin, Texas.

Keolian, R., V. Sparrow, Harpster, L., and N.B. Smith. 2003. A "Fresnel-Transducer" for Prostate Hyperthermia Treatment *Acoustical Society of America*, 146th Meeting of the Acoustical Society of America, 10-14 November 2003, Austin, Texas.

Saleh, K. and Smith, N.B., "Design and evaluation of a 63 element 1.75-dimensional ultrasound phased array for treating benign prostatic hyperplasia," *Acoustical Society of America*, 146th Meeting of the Acoustical Society of America, 10-14 November 2003, Austin, Texas.

Sun L., Al-Bataineh O., Collins C., Smith M.B., and Smith, N.B. Fast adaptive control for MRI-guided ultrasound hyperthermia treatment for prostate disease: in vitro and in vivo results, *International Society of Magnetic Resonance in Medicine (ISMRM) Twelfth Scientific Meeting & Exhibition*, Kyoto, Japan, 15-21, May 2004 (*submitted*).

Smith, N.B. "Therapeutic Applications of Ultrasound: Treatment of Prostate Disease and Noninvasive Drug Delivery", Invited seminars to:

- University of Illinois Urbana Champaign, Bioacoustics Research Laboratory Seminar Series, March 4, 2003
- University of Illinois Chicago – Department of Bioengineering, May 2, 2003
- University of Virginia - Department of Biomedical Engineering, Nov. 7, 2003
- Penn State University, College of Medicine Hershey, Nov. 11, 2003.

Note: only one invited speaking seminar power point presentation is included in this appendix since the talks were essentially the similar in content.

## Two-dimensional ultrasound phased array design for tissue ablation for treatment of benign prostatic hyperplasia

K. Y. SALEH<sup>†\*</sup> and N. B. SMITH<sup>†‡</sup>

<sup>†</sup> Department of Bioengineering; <sup>‡</sup> Graduate Program in Acoustics, College of Engineering, The Pennsylvania State University, 206 Hallowell Building, University Park, PA 16802, USA

(Received 11 October 2002; revised 16 April 2003; accepted 11 May 2003)

This paper describes the design, construction and evaluation of a two-dimensional ultrasound phased array to be used in the treatment of benign prostatic hyperplasia. With two-dimensional phased arrays, the focal point position can be controlled by changing the electrical power and phase to the individual elements for focusing and electronically steering in a three-dimensional volume. The array was designed with a steering angle of  $\pm 14^\circ$  in both transverse and longitudinal directions. A piezoelectric ceramic (PZT-8) was used as the material of the transducer, since it can handle the high power needed for tissue ablation and a matching layer was used for maximum acoustic power transmission to tissue. Analysis of the transducer ceramic and cable impedance has been designed for high power transfer with minimal capacitance and diameter. For this initial prototype, the final construction used magnet compatible housing and cabling for future application in a clinical magnetic resonance imaging system for temperature mapping of the focused ultrasound. To verify the capability of the transducer for focusing and steering, exposimetry was performed and the results correlated well with the calculated field. *Ex vivo* experiments were performed and indicated the capability of the transducer to ablate tissue using short sonications. For sonications with exposure time of 10, 15 and 20 s, the lesion size was roughly 1.8, 3.0 and 4.3 mm in diameter, respectively, which indicates the feasibility of this device.

**Key words:** Ultrasound transducer, two-dimensional array, focusing, matching layer, necrosis.

### 1. Introduction

Focused ultrasound surgery (FUS) or high intensity focused ultrasound (HIFU) is a clinical method for treating benign prostatic hyperplasia (BPH), a benign growth of prostatic cells that is not life threatening but can cause blockage to the urine flow as a result of the prostate pushing against the urethra and the bladder<sup>1</sup>. With FUS, tissue is non-invasively necrosed by elevating the temperature at the focal point above 60°C using short sonications (10–30 s) and deep FUS has been reported to successfully ablate prostate tissue without inducing damage to the rectal wall<sup>2–5</sup>. The goal of prostate ablation is mainly to remove a non-desirable growth of the prostate. This can be achieved using FUS that can necrose the target volume by focusing the ultrasound beam at a certain position, and then steer the focus to cover the whole enlarged volume. Since the size of the enlargement is usually much bigger than the size of the ultrasound focus, either a single focus is electronically steered in consecutive sonications or multiple focal points can be used at the same time to generate multiple lesions.

\* To whom correspondence should be addressed. e-mail: kysbio@engr.psu.edu

Existing techniques for treating BPH include hyperthermia, focused ultrasound, transurethral resection, prostatectomy and surgery. Although preferable, surgical techniques have numerous complications that appear in about one in four cases which include impotence, incontinence, urinary tract infections and often require a lengthy hospitalization<sup>6</sup>. With FUS, the ultrasound beam is focused at a specific location in the target volume to be necrosed. Since the tissue volume to be necrosed is larger than the geometric focus of the array, the transducer needs to be physically moved repeatedly to destroy the desired volume and unnecessarily extend the treatment time. Phased arrays overcome this problem by electrically steering the focal point from one location to another by changing the phase and power to the individual elements of the array.

Previous effective prostate ultrasound devices include both mechanically and electrically steered designs. One example of a commercial design is a focused, single element transducer which was mechanically manoeuvred to ablate tissue (Sonablate<sup>TM</sup> 500, Focus Surgery Inc., Indianapolis, IN, USA). Electrically steered include an experimental design which used a one-dimensional (1-D)  $57 \times 1$  aperiodic, linear array ( $87 \times 15 \text{ mm}^2$ ) which reduced grating lobes and could steer the focus in the radial and longitudinal but not the transverse direction<sup>7</sup>. Another experimental design was a  $60 \times 1$  linear array ( $75 \times 15 \text{ mm}^2$ ) with a mechanical translation that could electrically steer the focus in the radial and longitudinal but not the transverse direction<sup>8</sup>. The drawbacks behind these designs are that they can only steer the focus in the radial and longitudinal directions or require complex mechanisms to move the focus. Improvements over 1-D arrays for the treatment of localized prostatic cancer can be achieved. A new spherically curved 1.5-D phased array that used high intensity electronically focused ultrasound to steer a beam along two axes was designed and tested, allowing enough depth to be reached to treat large prostates and eliminating two degrees of mechanical movement<sup>9</sup>. The advantage with a 2-D phased array is that it can electrically focus and steer in the radial, longitudinal and transverse directions, which means that it has the capability of focusing and steering in a 3-D volume without the need to physically move the array.

Issues regarding the construction of an array used for FUS of the prostate initially deal with the frequency and size of the ceramic to be diced into an array. The resonance frequency should be greater than 500 kHz<sup>10</sup>, while the size of the transducer needs to be large enough to be able to deliver high power but small enough to be an intra-cavitary device. Before construction, computer simulations can be performed to determine the acoustic field. Pressure wave and temperature simulations indicated that a tapered array design reduced grating lobes significantly compared to equal element size arrays. Based on the computer model, a tapered array that satisfied grating lobes, frequency, and size limitations was designed. Lead zirconate titanate (PZT) was chosen as the ceramic material of the array, since it has the capability of handling the high electrical powers used in focused ultrasound. To maximize the acoustical power transmission from the elements and improve the structural integrity of the array face, a conductive matching layer was designed and fabricated. Issues regarding the cabling and electrical matching of the elements were also considered. Exposimetry of the acoustic field from the array was performed to compare experimental and calculated theoretical results. *Ex vivo* experiments using porcine kidney were also performed to demonstrate the feasibility of the array to necrose tissue. This research describes the design, construction and

evaluation of a 2-D ultrasound phased array that is capable of focusing and steering in a 3-D volume to be used in the treatment of BPH.

## 2. Materials and methods

### 2.1. Simulations

Computer simulation programs were written to determine the number and the size of the phased array elements in addition to determining the pressure and temperature field from the device. The array was modelled (figure 1) as a 2-D square array in order to have focusing and steering capabilities in both  $x$ - and  $y$ -directions ( $x$ =transverse,  $y$ =longitudinal and  $z$ =radial). The phase of each element was determined such that signals from individual elements were coherent at the shifting focal point. Measuring the difference in path length between each element to the focus in comparison to the path from the centre of the array to the focus determined the element phase calculation. The phase,  $\phi_i$ , (degrees) of element  $i$  was given by:

$$\phi_i = \frac{360^\circ}{\lambda} (d_i - d_o) - 360^\circ n \quad (1)$$

where  $\lambda$  is the wavelength (m),  $d_i$  is the distance (m) from the centre of element  $i$  to the focal point,  $d_o$  is the distance (m) from the centre of the array to the focus and  $n$  is an integer to keep  $0 = \phi_i = 360^\circ$ . Huygen's principle was used to model the pressure field as a summation of simple sources<sup>11</sup>. Thus, the total acoustic pressure at any point in the field can be calculated using:

$$p(x, y, z) = \sum_{i=1}^n \sqrt{\frac{2P\rho}{cA}} \left( \frac{fS}{d_i} \right) \exp \left[ j \left( \phi_i - \frac{2\pi d_i}{\lambda} \right) - d_i \alpha \right] \quad (2)$$

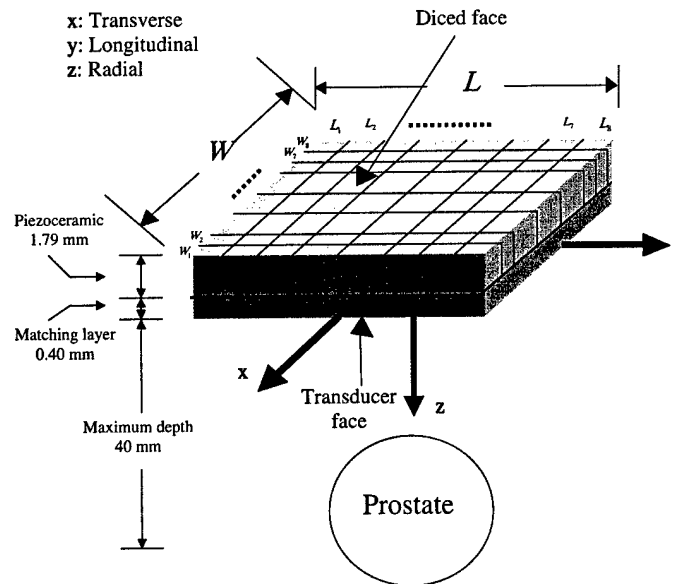


Figure 1. Based on the simulations, a diagram of the 2-D 64 element (8 x 8) tapered array with total size of  $20 \times 20 \text{ mm}^2$  with the proportions of the ceramic and matching layer illustrated. The diced face of the ceramic was cut 70% through and each individual element was attached to the electrical cabling using low temperature soldering material.

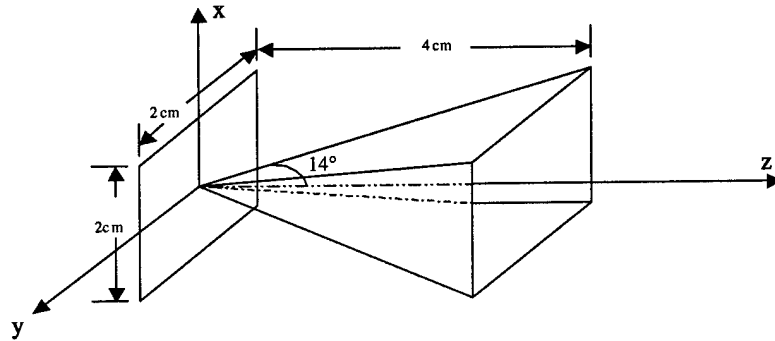


Figure 2. Within the volume shown in front of the transducer ( $2 \times 2 \text{ cm}^2$ ), the array was designed to focus and steer with an acceptable grating lobe level.

where  $p$  is the total acoustic pressure in Pascals (Pa),  $P$  is the total acoustic power emitted by the array in watts (W),  $\rho$  is the density of the medium ( $998 \text{ kg m}^{-3}$ ),  $c$  is the speed of sound in the water ( $1500 \text{ m s}^{-1}$ ),  $A$  is the total surface area of the array ( $\text{m}^2$ ),  $f$  is the resonance frequency ( $1.2 \text{ MHz}$ ),  $S$  is the area of the corresponding element ( $\text{m}^2$ ) and  $\alpha$  is the attenuation in soft tissue ( $10 \text{ Np m}^{-1} \text{ MHz}^{-1}$ ).

This array was capable of focusing and steering with a steering angle of  $14^\circ$  with a maximum focal depth of 4 cm. Figure 2 shows the volume in which the focal point can be focused and steered. Attempting to focus at a point that is out of this angle will result in a significant increase in grating lobes.

Off-axis focusing and the grating lobe level are directly related to each other, since increasing the steering angle causes a non-linear increase in the grating lobe level. For a focal point aimed at 0, 0, 30 mm, the results, which were plotted as a mesh (figure 3(a)) or contour (figure 3(b)), have shown to give a normalized intensity with a grating lobe level at  $\sim -20 \text{ dB}$ . Steering the focal point in the  $x$ -direction by focusing at 3, 0, 30 mm caused the grating lobe level to become  $-14 \text{ dB}$ . The result is shown as a mesh (figure 3(c)) or contour (figure 3(d)). Further increase of the steering angle increased the grating lobe level. For a focus at 6, 0, 30 mm, the grating lobe level was  $-10 \text{ dB}$ , as shown in the mesh (figure 3(e)) or contour (figure 3(f)) plots. Attempting to focus at a point that is outside the steering volume shown in figure 2 resulted in a significant increase of the grating lobe level. A focus at 9, 0, 30 mm (steering angle  $= 17^\circ > 14^\circ$ ) resulted in an unacceptable grating lobe level of  $-1.5 \text{ dB}$ , which is shown in the mesh (figure 3(g)) or contour (figure 3(h)) plots. In figures 3(b), (d), (f) and (h), the contour levels were plotted at 90, 80, 70, 60, 50, 40, 30, 20 and 10% of the maximum intensity.

Reduction of the treatment time can be achieved by generating multi-focal points simultaneously. Four focal points can be generated by dividing the array into four parts, each of which is responsible for generating a single focal point. Figure 4(a) shows a mesh plot for the normalized intensity as a function of  $x$  and  $y$  with four focal points being generated at the locations  $(x, y, z) = (\pm 2, \pm 2, 30) \text{ mm}$ . Reducing the distance between the focal points made them overlap. Focusing at  $(x, y, z) = (\pm 1.5, \pm 1.5, 30) \text{ mm}$  resulted in a partial overlapping as shown in the mesh plot (figure 4(b)) for the normalized intensity. A complete overlap between the four focal points was observed when focusing at  $(x, y, z) = (\pm 1, \pm 1, 30) \text{ mm}$ , as shown in the normalized intensity mesh plot (figure 4(c)).

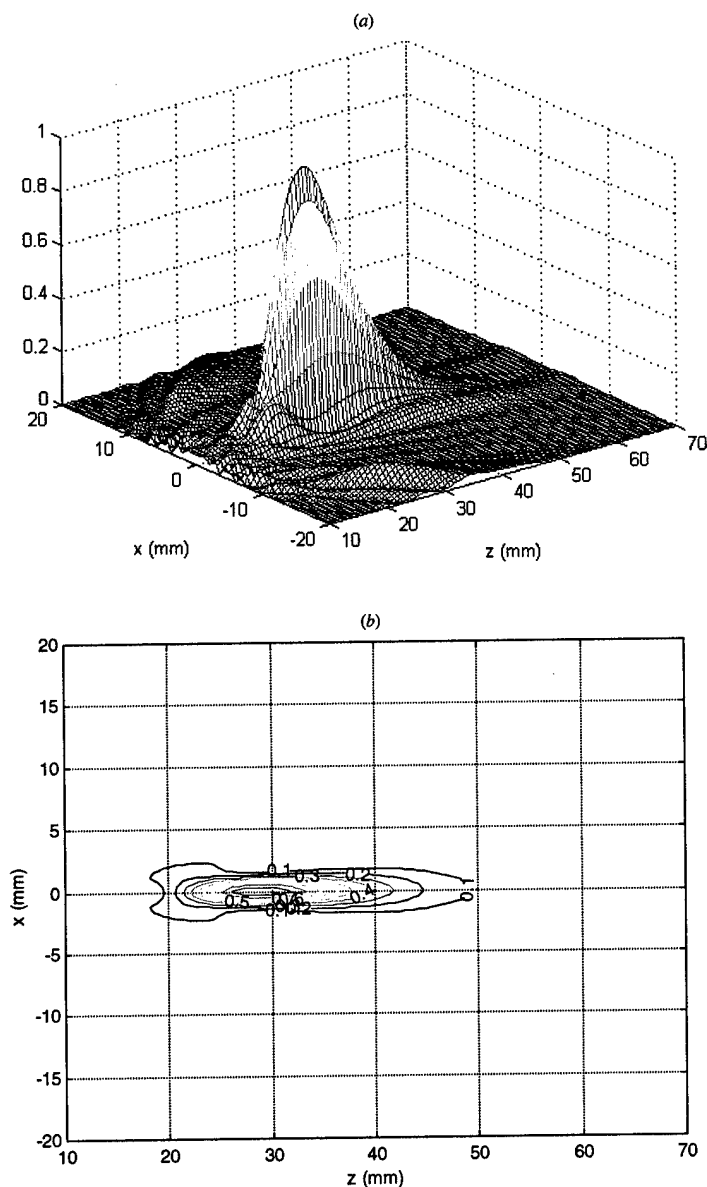


Figure 3. Off-axis focusing has a direct impact on the grating lobe level. Increasing the steering angle caused an increase in the grating lobe level. Shown is (a) a mesh or (b) a contour plot for the normalized intensity in the  $x$ - and  $z$ -directions with a focal point aimed at  $(x, y, z) = (0, 0, 30)$  mm that resulted in a grating lobe level of  $-20$  dB. A focus at  $(x, y, z) = (3, 0, 30)$  mm resulted in a grating lobe level of  $-14$  dB, as shown when plotting the normalized intensity as a (c) mesh or (d) contour. Further increase in the steering angle caused a further increase in the grating lobe level. Focusing at  $(x, y, z) = (6, 0, 30)$  mm caused the grating lobe level to be  $-10$  dB, which is shown in the normalized intensity (e) mesh or (f) contour plot. Attempting to focus outside the volume shown in figure 2 resulted in undesirable grating lobe values. Aiming the focus at  $(x, y, z) = (9, 0, 30)$  mm resulted in a grating lobe level of  $-1.5$  dB. The normalized intensity for this case is shown as a (g) mesh or (h) contour. In (b), (d), (f) and (h), the contour values were taken at 90, 80, 70, 60, 50, 40, 30, 20 and 10% of the normalized intensity.

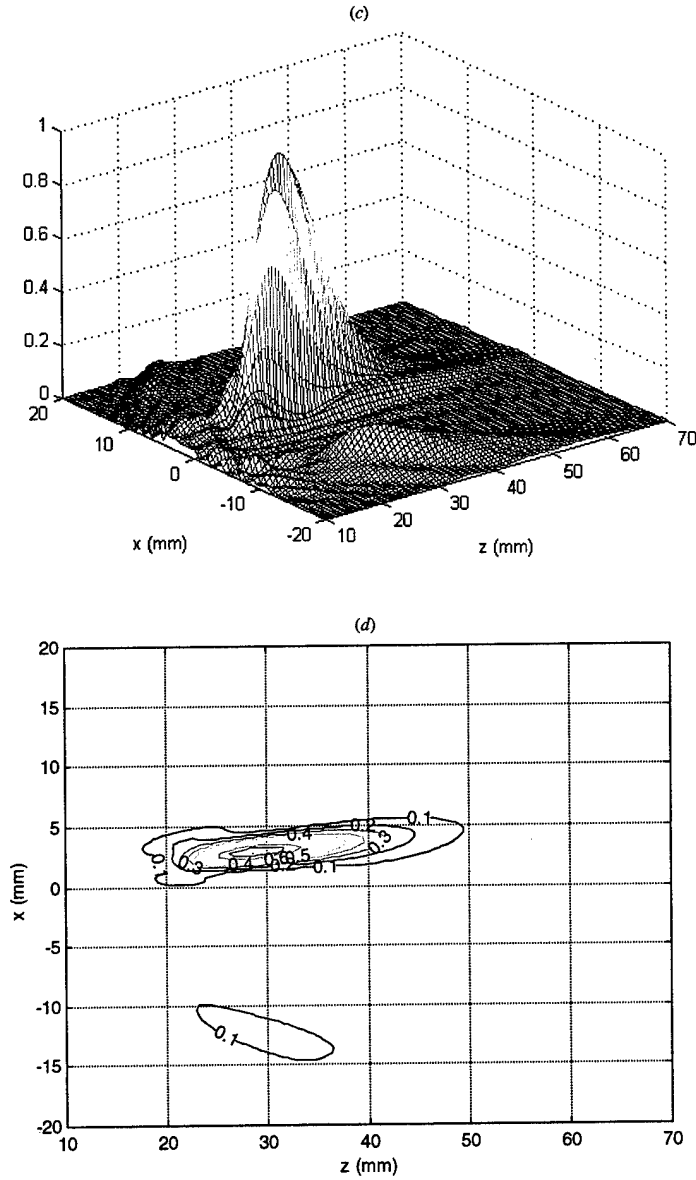


Figure 3. Continued.

From the pressure field of the simulated array, the temperature distribution in the tissue was modelled using the Pennes' bioheat transfer equation (BHTE)<sup>12</sup>:

$$\rho C_t \frac{\partial T}{\partial t} = K \left( \frac{\partial^2 T}{\partial x^2} + \frac{\partial^2 T}{\partial y^2} + \frac{\partial^2 T}{\partial z^2} \right) - w C_b (T - T_a) + q(x, y, z) \quad (3)$$

where  $C_t$  is the specific heat of the tissue ( $3770 \text{ J kg}^{-1} \text{ }^\circ\text{C}^{-1}$ ),  $K$  is the thermal conductivity ( $0.5 \text{ W m}^{-1} \text{ }^\circ\text{C}^{-1}$ ),  $T$  is the temperature at time  $t$  at the point  $x, y, z$  in  $^\circ\text{C}$ ,  $T_a$  is the arterial blood temperature ( $37^\circ\text{C}$ ),  $w$  is the perfusion in the tissue ( $5 \text{ kg m}^{-3} \text{ s}^{-1}$ ),

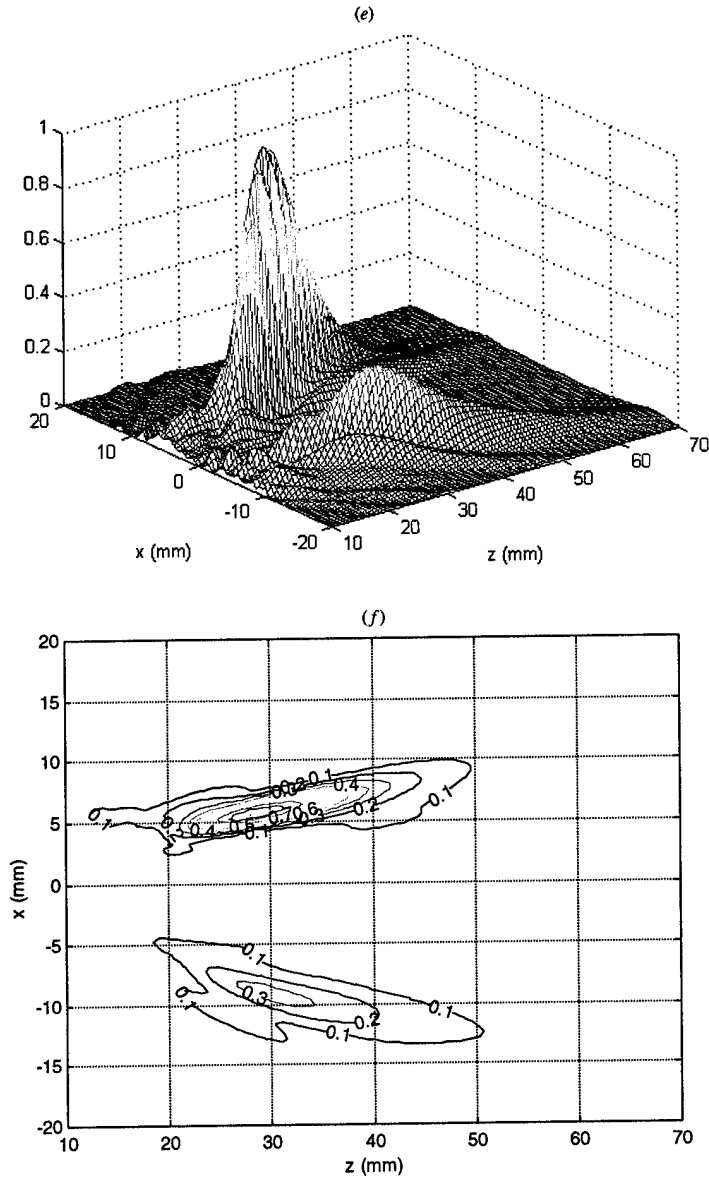


Figure 3. Continued.

$C_b$  is the specific heat of the blood ( $3770 \text{ J kg}^{-1} \text{ } ^\circ\text{C}^{-1}$ ) and  $q(x, y, z)$  is the power deposited at the point  $x, y, z$ . The power was calculated from the pressure field of the array design while the BHTE was determined using a numerical finite difference method with the boundary conditions set at  $37^\circ\text{C}$ . The total intensity at point  $(x, y, z)$  was also calculated from the pressure field of the simulated array and is given by<sup>13</sup>:

$$I(x, y, z) = \frac{p^2(x, y, z)}{2\rho c} \quad (4)$$

where  $I(x, y, z)$  is the intensity at point  $x, y, z$  in  $\text{W m}^{-2}$ .



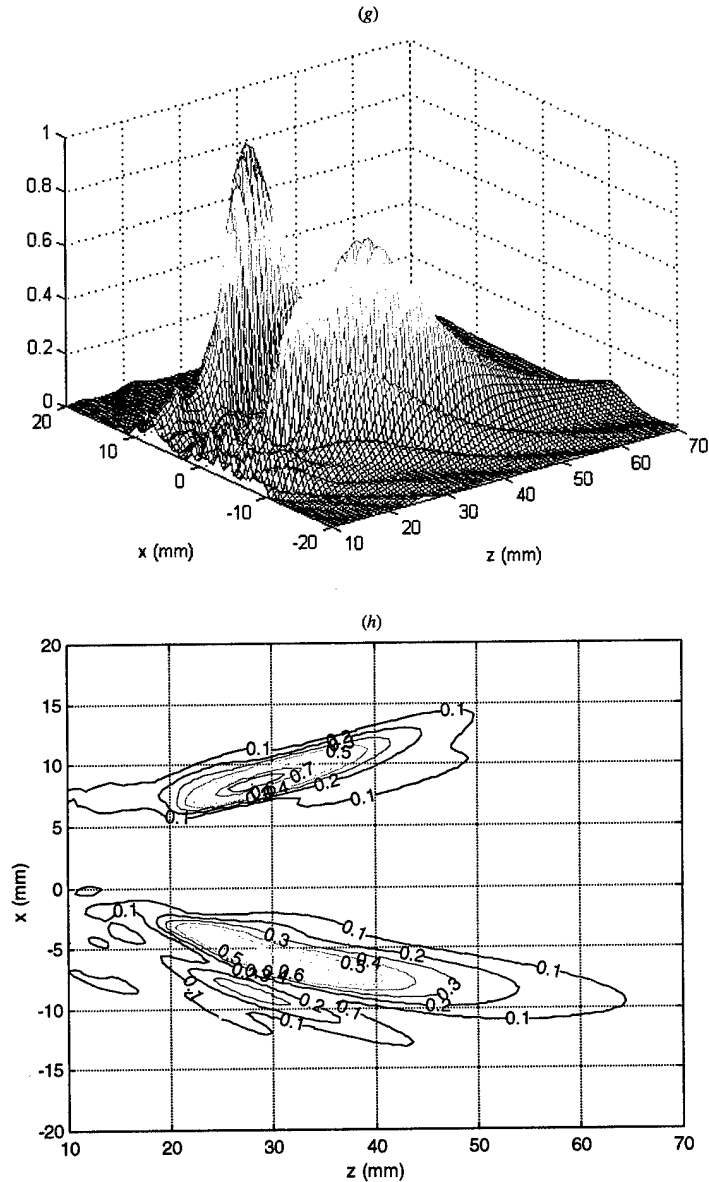


Figure 3. Continued.

Based on previous studies of transrectal probes, the width of the ceramic should be roughly no wider than 23 mm<sup>14</sup>. Initially, the simulated design used equal size elements of  $2.5 \times 2.5 \text{ mm}^2$  and, although it was capable of focusing and steering, it suffered from large grating lobes outside the focus. For example, at a focus of  $(x, y, z) = (5, 0, 30) \text{ mm}$  (i.e. the 0, 0, 0 position is at the centre of the transducer face in figure 1), the grating lobe level was  $-3.47 \text{ dB}$ , which was not desirable since this high level can cause an increase in tissue temperature outside the focus. Removing the periodicity of the array or tapering it has been shown to reduce the grating lobe level<sup>15</sup>. Both dimensions of the array were chosen to be identical in order to

have same focusing and steering capabilities in both  $x$  and  $y$  directions. The maximum possible steering angle was calculated to be  $\tan^{-1}(1.0/4.0) = 14^\circ$ , with maximal focal depth of 40 mm. The improved tapered array design started with a  $20 \times 20 \text{ mm}^2$  piece cut into an  $8 \times 8$  pattern with 64 individual elements with lengths ( $L$ ) and

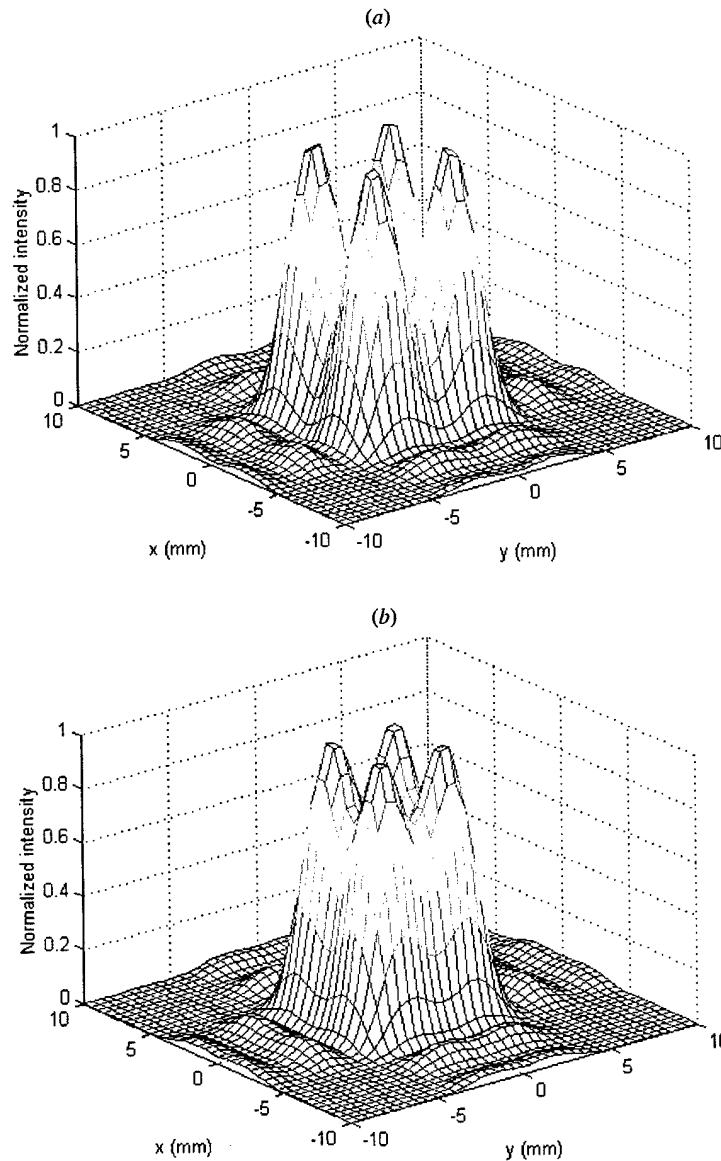


Figure 4. Pressure field simulations were performed to verify the capability of the array in generating four focal points by driving four parts of the array separately. Shown is the normalized intensity in the  $x$ - and  $y$ -directions for four focal points aimed at the locations  $(x, y, z) = (\pm 2, \pm 2, 30) \text{ mm}$  plotted as (a) a mesh. Partial overlapping between the four focal points occurred when focusing at  $(x, y, z) = (\pm 1.5, \pm 1.5, 30) \text{ mm}$ , as shown in the (b) mesh plot of the normalized intensity, while complete overlapping occurred when focusing at  $(x, y, z) = (\pm 1, \pm 1, 30) \text{ mm}$ , which is shown in (c).

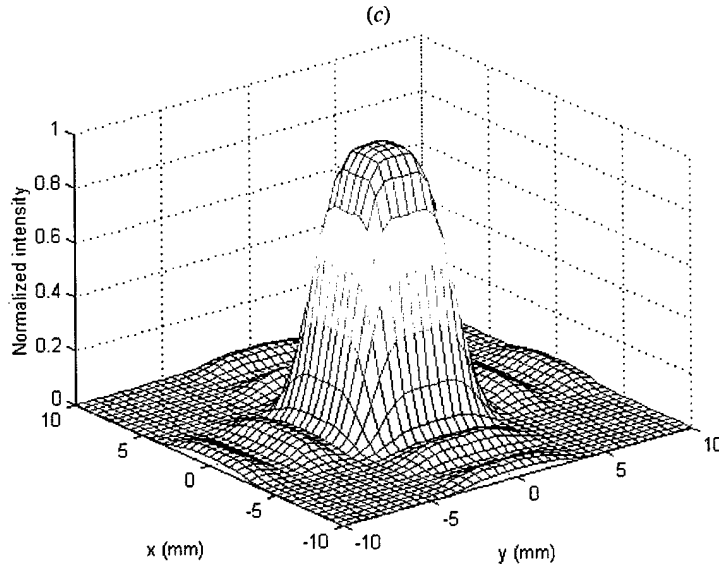


Figure 4. Continued.

widths ( $W$ ) of 2.00, 2.33, 2.66, 3.00, 3.00, 2.66, 2.33, 2.00 mm for elements  $i = 1-8$ , respectively (figure 1). Simulations have shown that the grating lobe level of the tapered design has decreased to  $-8.24$  dB at a similar focus location of 5, 0, 30 mm. Figure 5(a) shows a mesh plot for the normalized intensity as function of  $x$  and  $z$ , while figure 5(b) is the corresponding contour plot with contour levels at 90, 70, 50, 30 and 10% of the maximum intensity. From the simulations, a grating lobe level of 15% of the maximum value was observed which decreased at smaller steering angles. One of the techniques that can be used to reduce the grating lobes is based on the use of sub-sets of elements and de-activation of several elements in the array<sup>16</sup>. Although with this technique the grating lobes could be suppressed as a result of the non-periodicity resulted from activating some elements and de-activating others (usually chosen in random), for an array with a small number of elements a trade-off has to be made between using less elements and the need to drive those elements with higher power to generate the same lesion size with the same time. Temperature simulations were also used to verify the potential to increase the tissue temperature to  $60^\circ\text{C}$  with short sonications. Figure 5(c) shows the temperature distribution corresponding to the pressures for figure 5(a) and an increase in temperature was observed at the intended location of  $(x, z) = (5, 30)$  mm.

As indicated, off-axis focusing has a direct impact on the grating lobe level and, thus, the temperature. Increasing the steering angle leads to increasing the grating lobe level and, thus, causing an undesirable temperature increase at the grating lobe position. Figures 6(a-d) corresponded to the simulated pressure field generated in figures 3(a), (c), (e) and (g), respectively. For a focal point aimed at 0, 0, 30 mm, the temperature distribution plotted as a function of  $x$  and  $z$  (figure 6(a)) shows a  $60^\circ\text{C}$  focus at the intended location with a temperature value of almost  $37^\circ\text{C}$  elsewhere. Off-axis focusing caused a temperature increase at the location of the grating lobe. For a focus at 3, 0, 30 mm, the temperature at the grating lobe location was found to be  $40^\circ\text{C}$ , as shown in figure 6(b). Increasing the steering angle increased the

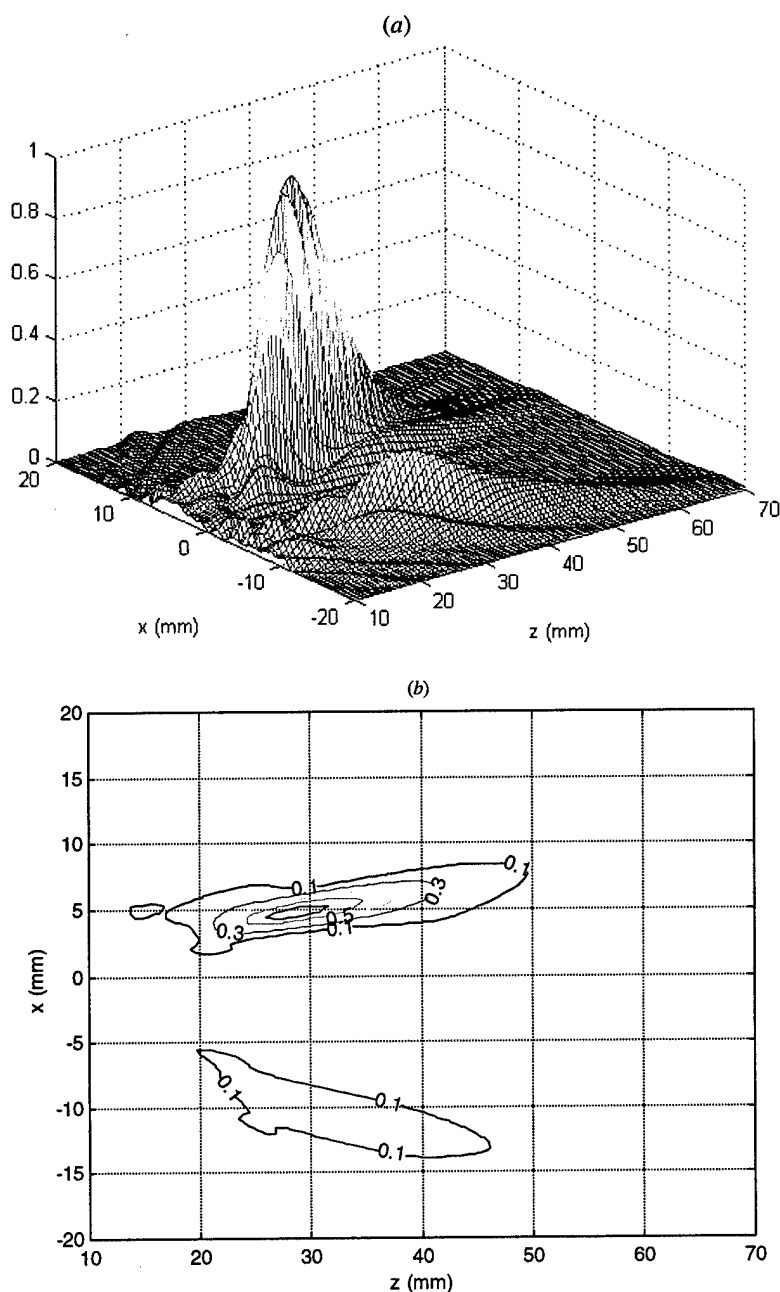


Figure 5. Before the construction of the array, simulations of the acoustic field were performed to evaluate the focusing of the elements and reduce potential grating lobes. Shown is the normalized intensity (a) in the  $x$ - and  $z$ -directions for a focal point at  $(x, y, z) = (5, 0, 30)$  mm along with (b) contour plot values taken at 90, 70, 50, 30, 10% of the normalized intensity with a grating lobe level of 15% of the maximum intensity. A temperature map (c) corresponding to the pressures generated in (a) was numerically solved using the bioheat transfer equation. This simulated figure shows an increase in tissue temperature to the target of  $60^{\circ}\text{C}$  at the focal point using 10 s sonication, while outside the target region the temperatures were normal, as indicated from the temperature colour bar.

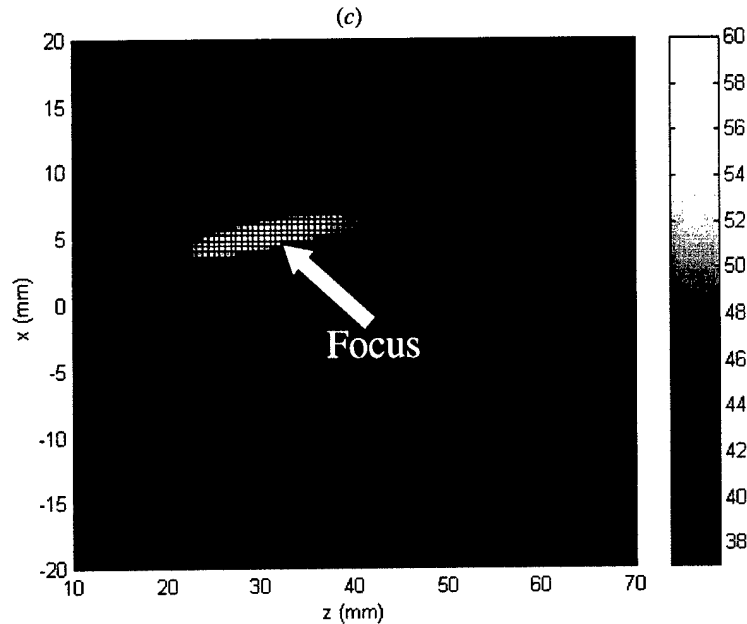


Figure 5. Continued.

grating lobe level and, thus, the undesirable temperature. A temperature of  $43^{\circ}\text{C}$  was observed at the grating lobe location when aiming the focus at 6, 0, 30 mm, as shown in figure 4(c). Trying to steer the focus outside the volume shown in figure 2 resulted in an unacceptable temperature value resulting from the grating lobe. A focus at 9, 0, 30 mm resulted in a grating lobe temperature of  $58^{\circ}\text{C}$ , as shown in figure 6(d).

## 2.2. Transducer construction

Choosing an appropriate piezoceramic material to be used in this application is essential, since it affects both electrical and acoustical properties of the array. Appropriate PZT that can be used include PZT-4, PZT-5H and PZT-8. For ultrasound imaging arrays, PZT-5H has a better performance when compared to the others, from a capacitance point of view, which is due to the fact that it has a large permittivity value, but at the same time it cannot handle the large electrical power that is used in focused ultrasound. With respect to power, PZT-4 and PZT-8 are good candidates with an advantage for PZT-8 over PZT-4, since it has an extremely high mechanical quality and extremely low loss factor. Thus, PZT-8 material (TRS Ceramics, State College, PA, USA) was chosen and diced, in house, into 64 elements forming the complete array. The cuts were made by dicing the material 70% through its thickness with a kerf width of  $96\text{ }\mu\text{m}$  using a dicing saw (Model 780, K & S-Kulick and Soffa Industries, Willow Grove, PA, USA) at the National Institute of Health (NIH) Medical Ultrasonic Transducer Technology Resource Centre located on The Pennsylvania State University campus (University Park, PA, USA).

For maximum acoustical power transfer from the individual elements to the tissue, a conductive matching layer was designed and fabricated. The thickness and material selection of the matching layer were designed based on the solution

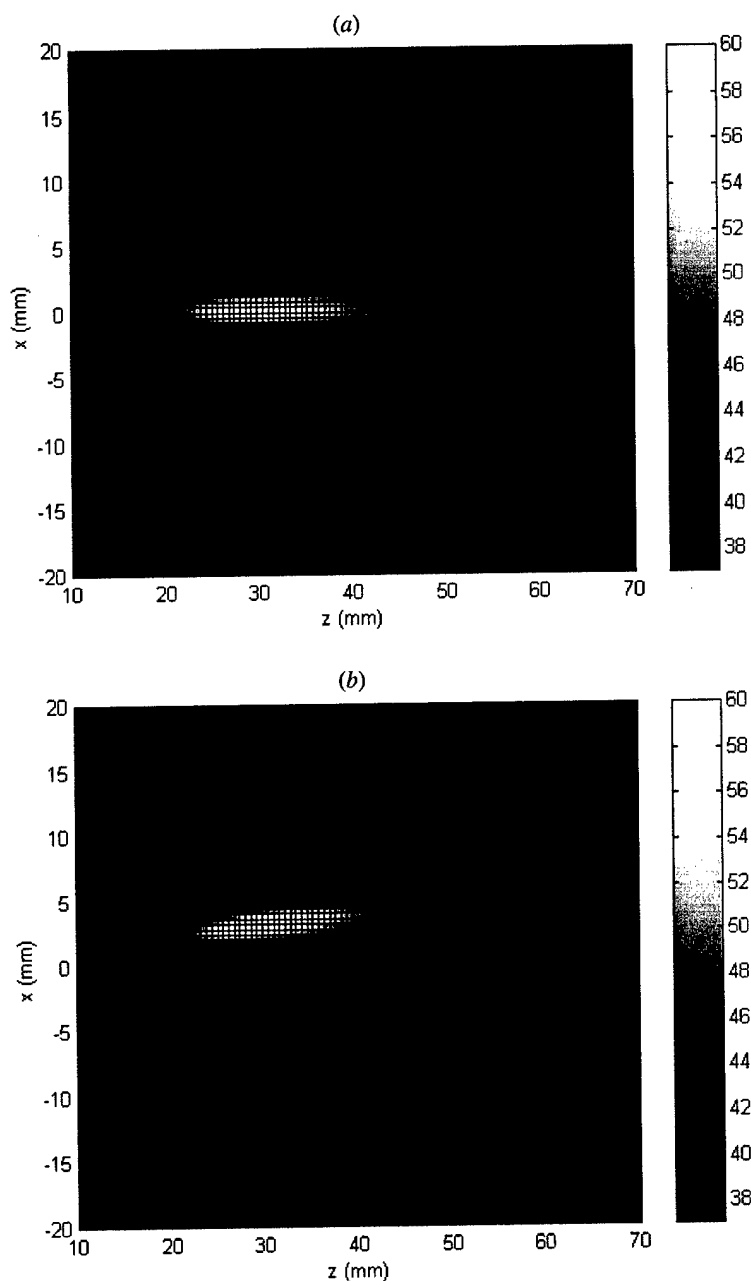


Figure 6. Corresponding to the pressures generated in figures 3(a), (c), (e) and (g), numerical temperature simulations were done using the bioheat transfer equation to plot the temperature maps (a), (b), (c) and (d), respectively. Those temperature maps show the effect of off-axis focusing on the temperature generated by the grating lobes. The temperature at the grating lobe location was found to be 38, 40, 43 and 58°C as a result of aiming the focus at  $(x, y, z) = (0, 0, 30)$ ,  $(3, 0, 30)$ ,  $(6, 0, 30)$  and  $(9, 0, 30)$  mm, respectively, as shown in (a), (b), (c) and (d), respectively.

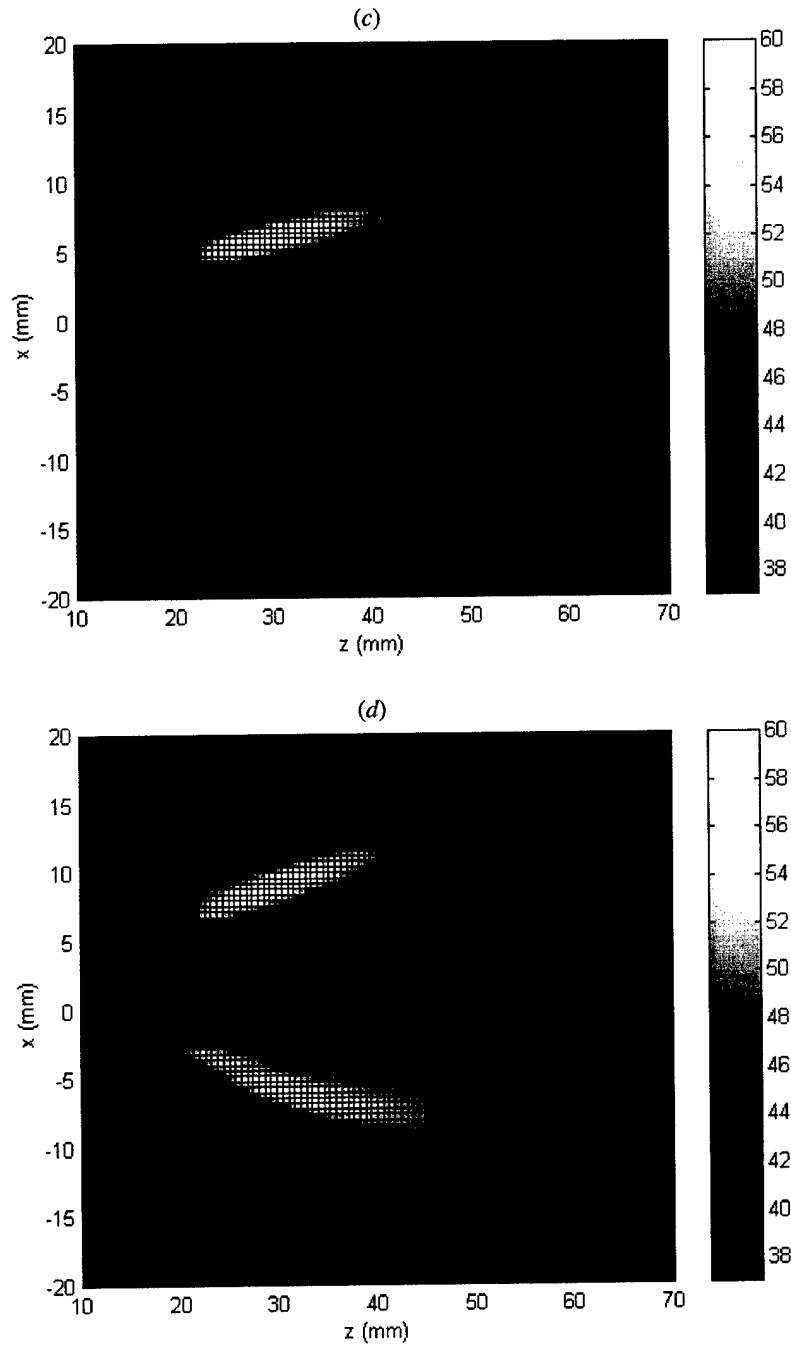


Figure 6. Continued.

to a three layer problem (transducer, matching layer and tissue), which ensured the required maximum power transfer. The PZT-8 material chosen for this design had an acoustic impedance of  $\sim 33 \text{ Mpa s m}^{-1}$  and the human tissue has an acoustic impedance of  $\sim 1.48 \text{ Mpa s m}^{-1}$  <sup>17,18</sup>. Since the input and the load impedances are not

the same, the intermediate matching layer was used between the piezoelectric material and the human tissue. Analysing a three layer problem indicated that the maximum power transmission occurs when the characteristic impedance of the matching layer equals the geometric mean of the piezoelectric characteristic impedance and the tissue characteristic impedance. With the longitudinal velocity in the matching layer material of  $v_L = 1900 \text{ m s}^{-1}$  and since the resonance frequency of the array ( $f_o$ ) was 1.2 MHz, the thickness of the matching layer was determined to be:

$$L = \frac{\lambda}{4} = \frac{1}{4} \left( \frac{v_L}{f_o} \right) = \frac{1}{4} \left( \frac{1900 \text{ m s}^{-1}}{1.2 \times 10^6 \text{ s}^{-1}} \right) = 0.396 \text{ mm}. \quad (5)$$

To construct the matching layer, parafilm was used to affix the piezoceramic to a glass plate with an adhesive primer poured onto the surface of the transducer face. The transducer was surrounded with a rubber dam and the silver conducting matching layer was poured onto the transducer surface. The matching layer, mixed in-housed, was a 2:1, epoxy-to-silver mixture of Insulcast 501 (Insulcast, Roseland, NJ, USA) and 2–3 micron silver epoxy (Aldrich, Milwaukee, WI, USA). The whole assembly was centrifuged for 10 min and cured overnight. After the rubber assembly was removed, the surface was sanded and lapped to the designed thickness. For the initial prototype, the specially machined, waterproof applicator housing ( $90 \times 60 \times 60 \text{ mm}^3$ ) was made from magnet compatible acrylic.

The capacitance of each element in the array depends primarily on the thickness, permittivity and the surface area. Since the element surface area is small, the capacitance will be small and, therefore, the element impedance will be large which makes it necessary to find a suitable cable that has a relatively low capacitance per unit length and, thus, high electrical impedance. For wiring the array, a low capacitance cable ( $75 \Omega$ , 15 pF/ft and 42 AWG) was used. The choice of such a cable was made based on the difficulty to electrically match small array elements to  $50 \Omega$  using high capacitance cables. Figure 7 shows a photograph of the final array.

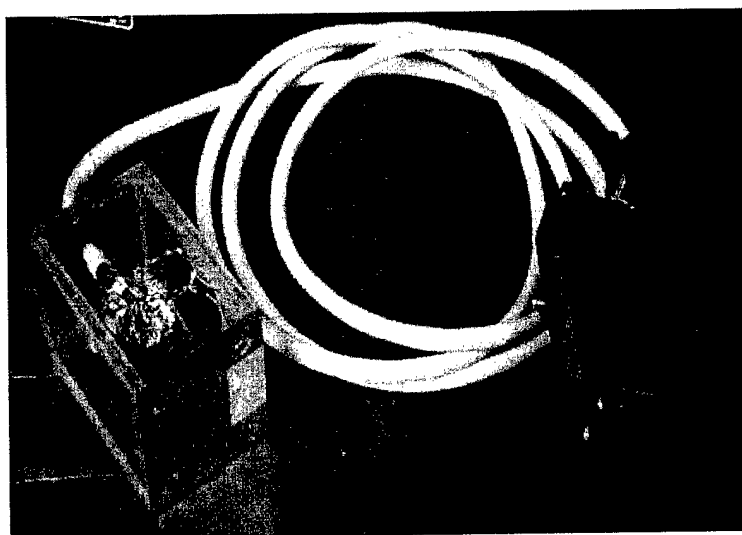


Figure 7. Photograph of the constructed, waterproof array machined from acrylic with 2.3 m low capacitance cable which connected to the amplifier system.



The connector between the cable and the amplifier used loose crimp contacts (PEI Genesis, Philadelphia, PA, USA), while the soldering between the cable and the 64 individual array elements used Indalloy #1E (Indium Corporation of America, Utica, NY, USA). This low temperature soldering material ensured that the temperature during soldering did not exceed the curie temperature for PZT-8 material. To drive the array, a specially built amplifier driving system (Advanced Surgical Systems Inc., Tucson, AZ, USA) was used<sup>19</sup>. Briefly, this amplifier system was a multi-channel high power, ultrasound phased-array transducer driver for 64 elements, which is capable of delivering 60 W per channel with  $\pm 1^\circ$  phase resolution each. To match the impedance of the elements to the amplifier, individual LC (L = inductor and C = capacitor) circuits were built for each of the 64 elements to match each one to the common value of  $50 \Omega \angle 0^\circ$ .

### 2.3. *Exposimetry*

To determine the acoustic field generated by the array, an automated computer controlled positioning system, which could translate an hydrophone throughout the acoustic field of the array placed in a water tank, was used. The transducer was submerged in water (room temperature,  $\sim 20^\circ\text{C}$ ) in a tank ( $120 \times 50 \times 52 \text{ cm}^3$ ) made almost anechoic with sound absorbing rubber. A custom-made degasser, built in-house, was used to reduce the dissolved oxygen content of the distilled water to 1–2 ppm to reduce cavitation. The system was controlled using a personal computer connected to a four-motor positioning system (Velmex Inc., Bloomfield, NY, USA) via the RS232 serial port and also connected, via the general purpose interface bus (GPIB), to a digital oscilloscope (Agilent 54622A, Agilent Technologies, Palo Alto, CA, USA), which recorded the voltage amplitudes detected by the hydrophone. Custom written, Quick Basic (Microsoft Corporation, Redmond, WA, USA) programs were used for automated control of the motors and data acquisition from the oscilloscope. Initially, multiple on-axis (i.e. where the focus is along the major z-axis,  $z_f$ ) exposimetry experiments were performed. With the focus set to 0, 0,  $z_f$  mm,  $z_f$  was varied from 10–40 mm, with a step size of 2 mm. To determine the repeatability of the focusing, 5–10 experiments were performed at each location. For off-axis studies (i.e. where the focus was not on z but aimed toward the x or y axis,  $x_f$  or  $y_f$ , respectively), the focus was located at  $x_f, y_f, 30$  mm, while the steering angle was adjusted to the desired value by choosing appropriate values for  $x_f$  and  $y_f$ . The steering angle was varied from  $-14^\circ$  to  $+14^\circ$  with a step size of  $2^\circ$  in both x and y directions with multiple experiments (5–10) performed at each angle. In both the on-axis and off-axis experiments, the scanning step size was 0.5 mm, while the scanning area was  $20 \times 20 \text{ mm}^2$ . The hydrophone voltage recordings were used to calculate the normalized intensities based on the pressures that were plotted as the mean and standard deviation of the results ( $\bar{x} \pm \text{SD}$ ) and compared against the calculated values<sup>20,21</sup>.

### 2.4. *Ex vivo experiments*

To test the feasibility of the array to ablate tissue, the array was submerged 3 cm in the tank aimed perpendicular to the surface of the water. Fresh porcine kidney was obtained, placed in the tank and held in front of the transducer face using metal clamps to ensure that it did not move during the experiments. A distance of 1 cm was maintained between the face of the array and the kidney to mimic the distance of a water bolus used in clinical treatments<sup>22</sup>. Sonication experiments drove

each element at an average electrical power of 8 W for 10 s for both on- and off-axis focusing. For the off-axis focusing, the steering angle was at  $5.7^\circ$  in the  $x$ -direction and  $13.1^\circ$  in the  $y$ -direction. To examine the effects of sonication time, subsequent sonications used exposures of 15 and 20 s. At the end of the sonications, the kidney was carefully removed and sliced with a scalpel to evaluate the ablated areas. Lesions were recorded several times for size using a digital caliper and digitally photographed.

### 3. Results

To test the correlation between experimental and theoretical results, exposimetry experiments were performed. As an example of a typical result at the location  $(x, y, z) = (0, 3, 30)$  mm, figure 8(a) shows a comparison plot along the  $x$ -axis of the calculated and experimental normalized intensities. Figure 8(b) plots similar theoretical and experimental data but along the  $y$ -axis for the same focus. For both plots, the theoretical intensity data correlated well with the experimental results. From multiple experiments to evaluate the feasibility of the array to steer the focus, a typical 3-D normalized intensity result from a focal point was aimed at  $-2, -0.7, 30$  mm. The results were plotted as a mesh (figure 9(a)) or contour (figure 9(b)), with contour levels at 90, 70, 50, 30 and 10% of the maximum intensity and the grating lobe levels at  $\sim -7.0$  dB or less.

*Ex vivo* experiments were also performed to verify the feasibility of the array to generate foci that are capable of ablating tissue. In the first sonication experiment, the elements were driven at an average power of 8 W for 10 s for on-axis focusing. In the plane that was 30 mm deep in tissue and parallel to the face of the array, a cigar shaped lesion with a length of 4.5 mm, along the  $z$ -axis, and a diameter of

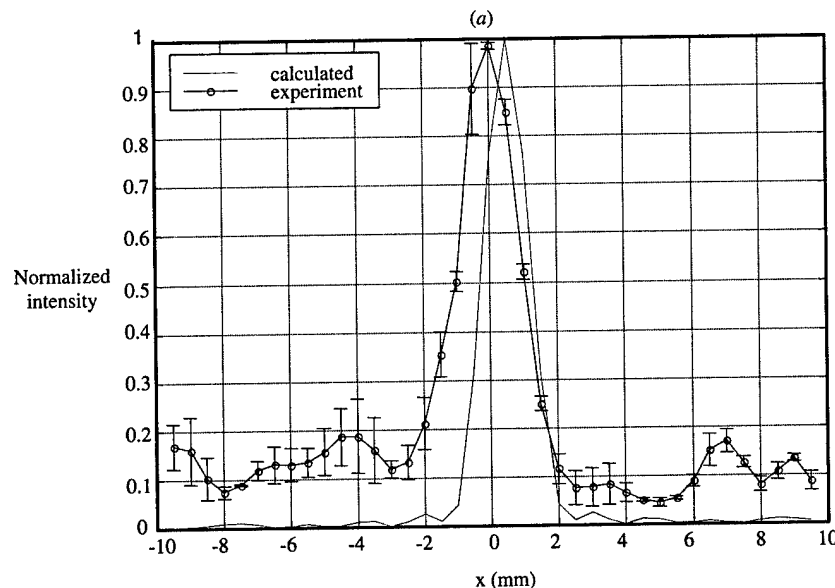


Figure 8. Comparison of calculated and experimental normalized intensities for a focus at 0, 3, 30 mm plotted along the (a)  $x$ -axis and (b)  $y$ -axis.

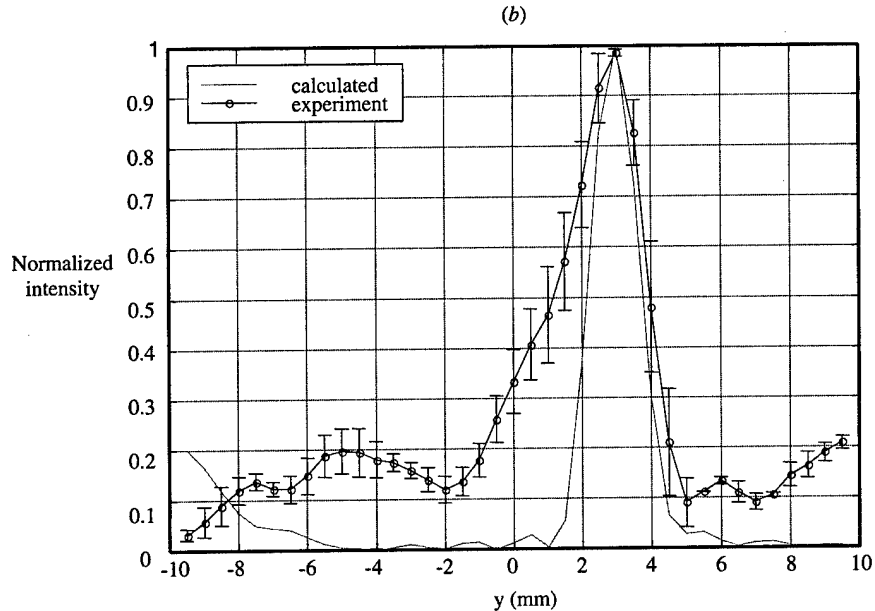


Figure 8. Continued.

2 mm was observed (figure 10(a)). Evaluation of the off-axis steering also used an average power of 8 W for 10 s to generate three separate lesions at locations  $(x, y, z) = (-3, -7, 30)$ ,  $(0, 0, 30)$  and  $(3, 7, 30)$  mm. Figure 10(b) shows a digital photograph of three lesions, each  $\sim 2$  mm in diameter, which corresponded to the intended locations. To determine the effects of sonication time, the location and exposure time was focused at 0, 0, 30 mm for 10 s, 0, 0, 34 mm for 15 s and 0, 0, 39 mm for 20 s at 8 W per element. Three lesions were observed with a diameter of 2, 2.9 and 4 mm that corresponded to the sonication times of 10, 15 and 20 s, respectively (figure 10(c)).

Further *ex vivo* experiments were performed to verify the capability of the array in generating off-axis lesions. A single 10 s sonication was performed with the elements of the array driven at an average power of 8 W to generate a single off-axis lesion at the location 5, 0, 30 mm. Figure 11(a) is a cross-section that was made in the plane that was  $9.5^\circ$  ( $\tan^{-1}(5/30) = 9.5^\circ$ ) away from the  $z$ -axis, which shows a lesion with  $\sim 4$  mm length along that axis. A cross-section in the plane that was 30 mm deep in tissue and parallel to the face of the transducer shows the shape and size of the lesion in the  $x$ - $y$  plane, which was observed to be 2 mm in diameter, as shown in figure 11(b).

As shown in the simulations from figure 4(c), the array was theoretically capable of generating a single large focal point that resulted from the overlapping of four focal points generated separately at the locations  $\pm 1, \pm 1, 30$  mm. To verify this, the average power was kept at 8 W and the sonication time was increased to 25 s to compensate for the reduction in the overall power per focus. A cross-section was made in a plane that was 30 mm deep in tissue and parallel to the  $x$ - $y$  plane. A large lesion with a diameter of 4 mm was observed (figure 12) using this focal overlapping technique.

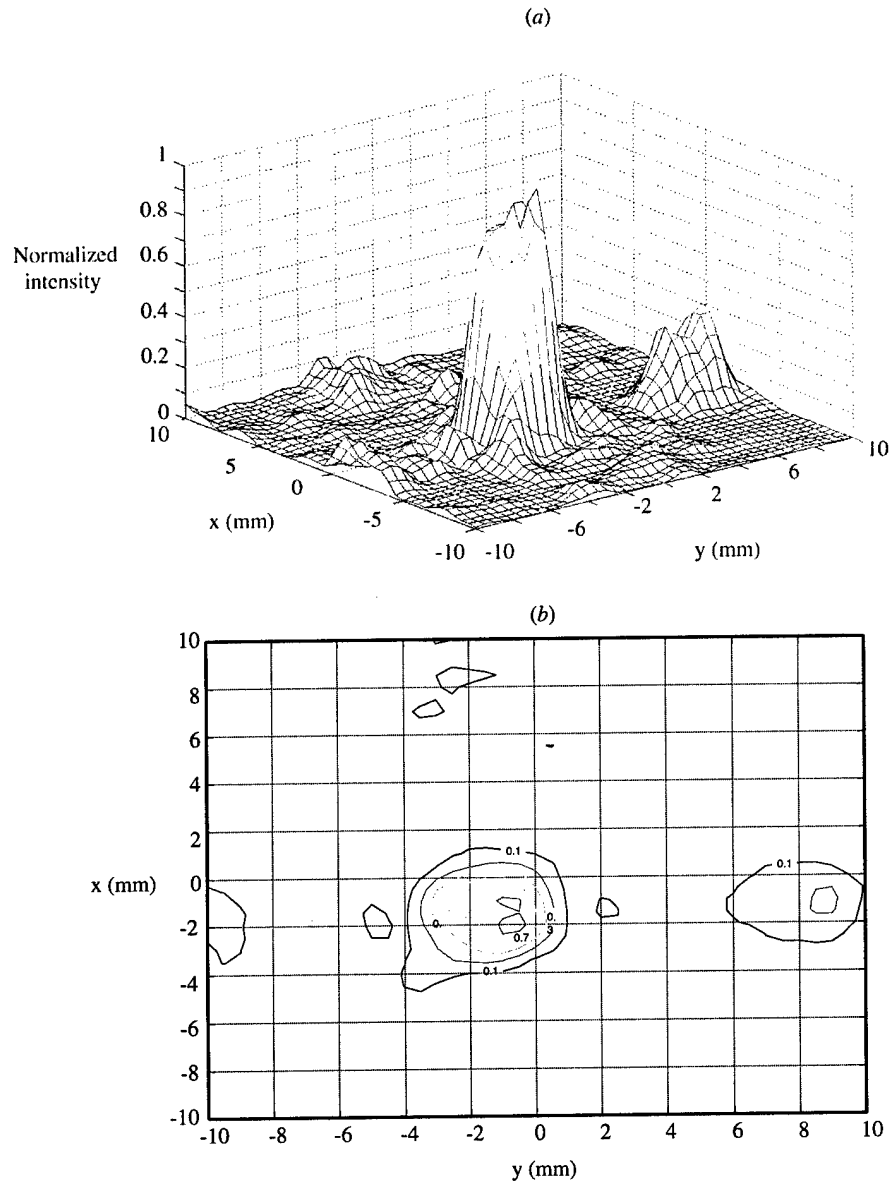


Figure 9. Exposimetry results of the normalized intensity for off-axis focusing with the focal point aimed at  $-2, -0.7, 30$  mm plotted as (a) a mesh or (b) a contour with levels indicated at 90, 70, 50, 30, 10%. These results indicate acceptable grating lobes of less than  $-7.0$  dB.

#### 4. Discussion

Intra-cavitary ultrasound offers an attractive means of focused ultrasound treatment for benign prostatic hyperplasia with significant advantages over other treatment methods due to the relatively short treatment time, its non-invasive nature and reduced complications. One compelling reason for using an intra-cavitary device with focused ultrasound is that the prostate is easily accessible via transrectal applicators, which allow for heating of the target volume in the prostate with

minimal heating of normal tissue. Using phased arrays to electrically focusing the ultrasound beam provides a controlled localized power deposition into tissue and reduces significantly the treatment time since the focus is electronically scanned instead of manually.

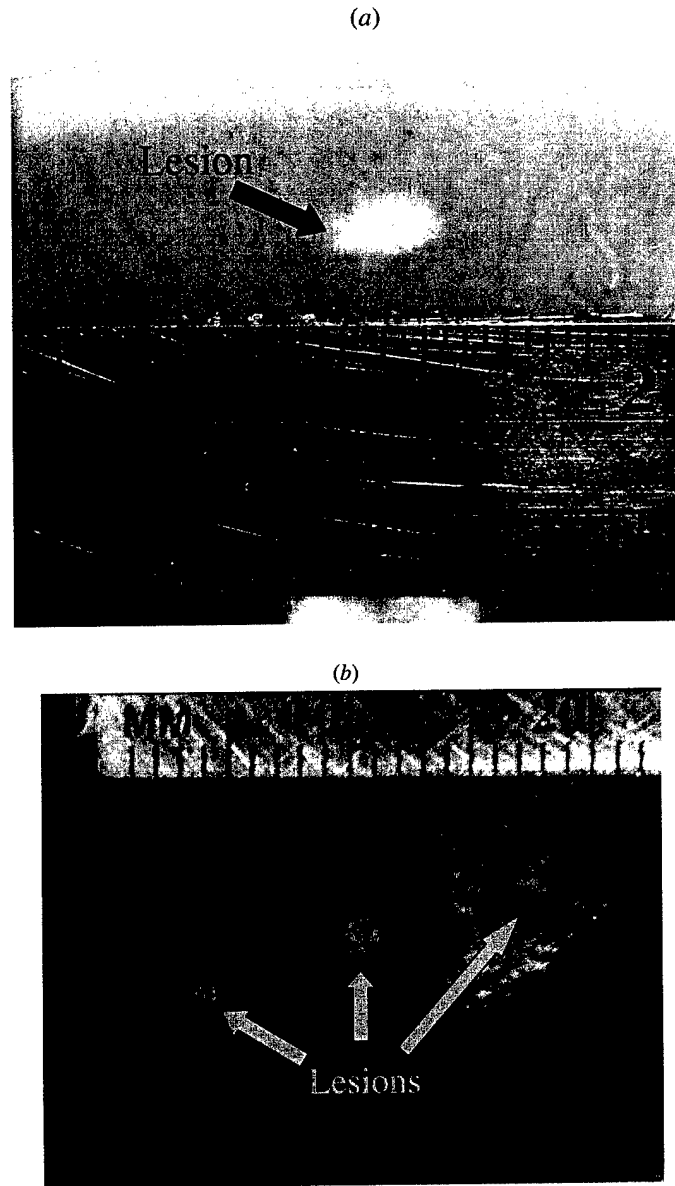


Figure 10. *Ex vivo* experimental results of lesions created with on and off-axis focusing with the array driven at an average of 8 W per element for various sonication times. (a) Focusing 30 mm into the tissue, a cigar shaped lesion was created from a 10 s sonication. (b) Evaluation of the electrical steering at  $(x, y, z) = (-3, -7, 30)$ ,  $(0, 0, 30)$  and  $(3, 7, 30)$  mm created 2 mm diameter lesions. (c) Effects of the sonication time variation are illustrated from exposure times of 10, 15 and 20 s.

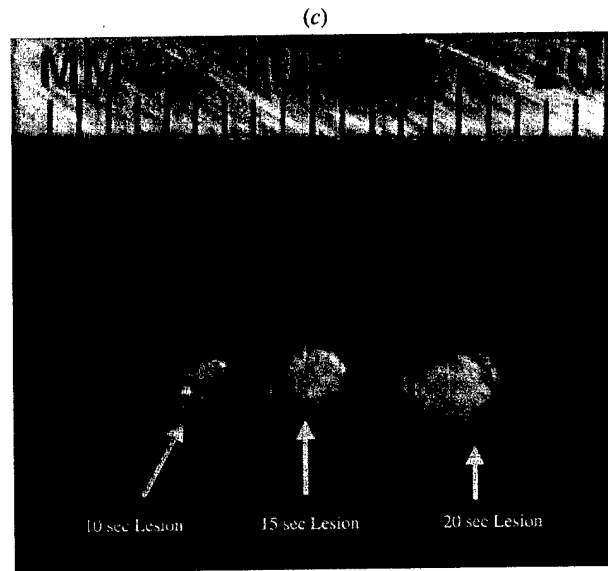


Figure 10. Continued.

Previous focused ultrasound array designs were problematic, since they required complex methods to move the focus, or had linear (1-D) designs that were only capable of focusing along one axis. These drawbacks were the motivation to design a new array that can be used in FUS and, at the same time, be systematically controlled to reposition the focus throughout a specific volume with an acceptable level of grating lobes. Care was taken with this new 64 element,  $8 \times 8$  array to account for capacitance issues between the ceramic and cables by modelling the system and impedance testing with various cables. Further improvement over this array design seems to be feasible due to recent developments in building focused transducers using piezocomposite technology<sup>23</sup>. Using piezocomposites removes the concern of low width to thickness ratios, which was an issue in this array design. A three layer PZT-8 material may also be used to increase the capacitance and, thus, make it easier to electrically match the small elements.

In designing this array, several issues were taken into account to address its application for BPH treatment. The dimensions of the array were designed for an intra-cavitary rectal device. With appropriate housing, a dimension of  $2 \times 2$  cm array is suitable. Although the housing used here does not satisfy this condition, this design was used to evaluate the feasibility of the steering. Another issue concerning this design was the grating lobe level, which was reduced significantly by tapering the elements widths and lengths of the array.

To treat the prostate, this array was aimed toward the intended target volume and the elements were driven at a calculated amplitude and phase to generate either a single focal point with electrical steering or generate multiple focal points simultaneously to increase the necrosed volume per sonication. To generate multiple focal points, the total area of the array was divided into several sub-areas (four, for example), the array was driven in such a way that each one of these sub-areas was responsible for generating a single focal point. Although this reduces

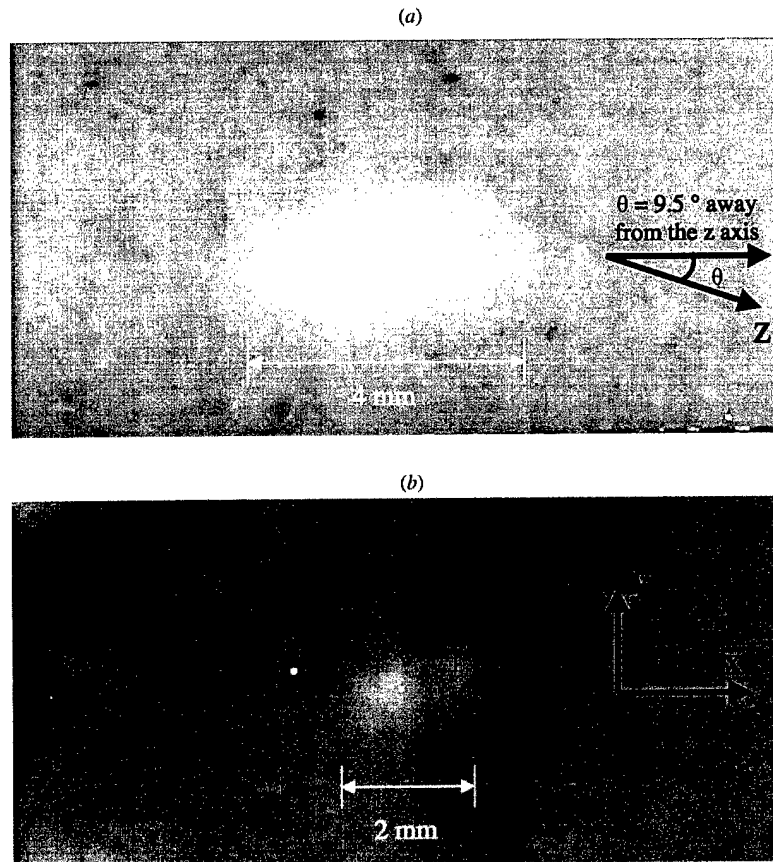


Figure 11. An *ex vivo* experimental result showing orthogonal paired cross-sections of a lesion generated by focusing at 5, 0, 30 mm (steering angle =  $9.5^\circ$  away from the z-axis). Shown is (a) a cross-section made along the focusing plane ( $9.5^\circ$  away from the z-axis) that indicates a 4 mm long cigar shaped lesion and (b) a cross-section made parallel to the x-y plane and 30 mm deep in tissue, showing the size of the lesion in that plane, which was found to be a 2 mm diameter lesion.

the sonication time, it requires more driving power since each sub-area needs to generate a single focal point.

This array is not designed to ablate the whole prostate, although that can be achieved by mechanically moving the array several times depending on the prostate size. As was previously shown in figure 2, this array can necrose a volume that lies in its steering volume. Assuming that the centre of the volume to be necrosed is 3 cm deep, this array is capable of necrosing a volume of at least  $1 \times 1 \times 2 \text{ cm}^3$  without mechanically moving the array. Taking this ( $1 \times 1 \times 2 \text{ cm}^3$ ) as the target volume, two techniques can be used to necrose it; the first one is using a single focal point regime in which the target volume is divided into small volumes. The size of these small volumes is chosen based on the size of the lesion and the sonication time. For a 10 s sonication, the lesion was found to be a 4 mm long cigar shape with 2 mm diameter. Therefore, dividing the  $1 \times 1 \times 2 \text{ cm}^3$  volume into  $5 \times 5 \times 5$  points indicates that 125 sonications are needed to necrose the target based on a single 10 s sonication that is electronically steered between the 125 positions. Starting at the centre of the

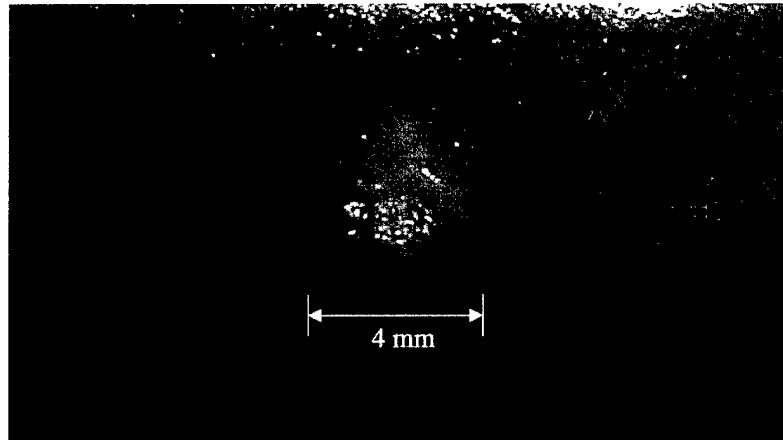


Figure 12. To verify the feasibility of generating a large lesion as a result of four overlapped small lesions, the array was driven at an average power of 8 W for 25 s, with four focal points aimed at  $\pm 1, \pm 1, 30$  mm. A cross-section made parallel to the  $x$ - $y$  plane and 30 mm deep in tissue shows the generation of a single large lesion with a diameter of 4 mm.

target volume, a single focal point is generated there and then electronically steered 125 times to cover the whole volume. To avoid uncontrolled heat buildup and pre-focal heating, the switching between the focal points is done in a way that any two focal points consecutive in time are far away from each other in distance. By doing that, enough time is given to the pre-focal positions to cool down. A second technique to necrose a large volume is by generating multi-focal points at the same time. Dividing the array into four areas, each responsible for generating a single focal point, will result in reducing the overall treatment time by a factor of four. This technique is time efficient, but the drawback behind it is that the driving electrical power per unit area should be increased.

Since the maximum possible steering angle for this array is  $14^\circ$  in both transverse and longitudinal directions, attempting to focus outside this volume will add a significant amount of grating lobes which will cause an unwanted heating. This puts a limitation for this array if the target volume extends beyond the  $14^\circ$  limit. Trying to focus 2 cm deep is feasible, however the maximum off-axis steering at 2 cm deep is 0.5 cm, which adds another limitation if a 1 cm off-axis steering is required to ablate anterolateral prostate tissue.

When coupled with MR temperature mapping, FUS provides an efficient way to treat BPH and at the same time gives a quick feedback about the temperature distribution inside the prostate<sup>8</sup>. Although ultrasound imaging for the prostate has shown to give good results<sup>24,25</sup>, the array described here was designed to be accompanied by an MRI.

Similar to prostate cancer treatment with focused ultrasound, benign fibroadenomas in the breast are currently treated clinically using multiple sonication from a single element transducer which is mechanically scanned<sup>26</sup>. In conjunction, magnetic resonance imaging (MRI) for guidance of thermotherapy of the procedure<sup>27</sup>. Although the treatment has been shown to be effective, the process includes an unnecessary delay due to the mechanical scanning protocol. When closely spaced locations are targeted with focused ultrasound, thermal build-up results from the accumulation of neighbouring sonications and the near field heating. As a result,



a lengthy delay between sonications (cooling time) is required to reduce thermal build-up. Investigators have shown that a cooling time of 50–60 s was necessary to reduce the heat from the near neighbour sonications<sup>28</sup>; however, this can add considerable time to the procedure and initiate inaccuracies to the MR thermometry through patient motion. With phased arrays, a focal pattern can be arranged such that there is enough time for the heat to dissipate by sonicating non-neighbouring regions within the tumour<sup>29</sup>. A treatment planning routine can be plotted over the entire tumour region such that the volume is ablated through distant and non-adjacent ablations to avoid thermal build-up yet destroy the volume in the least amount of time. This research demonstrates the feasibility of an electrically steered array, which can be used to ablate tissue for the intended treatment of benign prostatic hyperplasia. Future plans will advance this design to a clinical model to be used for *in vivo* studies.

### Acknowledgements

This work was supported by the Whitaker Foundation (RG-00-0042) and the Department of Defense Congressionally Directed Medical Prostate Cancer Research Program (DAMD17-0201-0124).

### References

1. Stephens F. *All about prostate cancer*. South Melbourne, Australia; New York: Oxford University Press, 2000.
2. Tan JS, Frizzell LA, Sanghvi NT, Seip R, Wu JS, Kouzmanoff JT. Design of focused ultrasound phased arrays for prostate treatment. *IEEE Ultrason Symp* 2000; 1247–51.
3. Seip R, Sanghvi NT. Comparison of split-beam transducer geometries and excitation configuration for transrectal prostate HIFU treatments. *IEEE Ultrason Symp* 2001; 1343–46.
4. Ebbini ES, Bischof JC, Coad JE. Lesion formation and visualization using dual-mode ultrasound phased arrays. *IEEE Ultrason Symp* 2001; 1351–54.
5. Yao H, Phukpattaranont P, Ebbini ES. Enhanced lesion visualization in image-guided noninvasive surgery with ultrasound phased arrays. *23rd Annual EMBS international conference, IEEE* 2001; 2492–95.
6. Barrett DM. *Mayo Clinic on prostate health*, 1st edn. Rochester, MN; New York: Mayo Clinic, 2000.
7. Hutchinson EB, Hynynen K. Intracavitary phased arrays for non-invasive prostate surgery. *IEEE Trans Ultrason Ferroelectr Freq Control* 1996; 43: 1032–42.
8. Sokka S, Hynynen K. The feasibility of MRI guided whole prostate ablation with a linear aperiodic intracavitary ultrasound phased array. *Phys Med Biol* 2000; 45: 3373–83.
9. Curiel L, Chavrier F, Souchon R, Birer A, Chapelon JY. 1.5-D high intensity focused ultrasound array for non-invasive prostate cancer surgery. *IEEE Trans Ultrason Ferroelectr Freq Control* 2002; 49: 231–42.
10. Buchanan MT, Hynynen K. Design and experimental evaluation of intracavitary ultrasound phased array system for hyperthermia. *IEEE Trans Biomed Eng* 1994; 41: 1178–87.
11. Zemanek J. Beam behavior within the nearfield of a vibrating piston. *J Acoust Soc Am* 1971; 49: 181–91.
12. Pennes HH. Analysis of tissue and arterial blood temperatures in the resting human forearm. *J Appl Physiol* 1948; 1: 93–122.
13. Nyborg WL. Heat generation by ultrasound in a relaxing medium. *J Acoust Soc Am* 1981; 70: 310–12.
14. Smith NB, Buchanan MT, Hynynen K. Transrectal ultrasound applicator for prostate heating monitored using MRI thermometry. *Int J Radiat Oncol Biol Phys* 1999; 43: 217–25.
15. Hutchinson EB, Buchanan MT, Hynynen K. Evaluation of an aperiodic phased array for prostate thermal therapies. *IEEE Ultrasonics Symp* 1995; 1601–04.

16. Gavrilov LR, Hand JW, Abel P, Cain CA. A method of reducing grating lobes associated with an ultrasound linear phased array intended for transrectal thermotherapy. *IEEE Trans Ultrason Ferroelectr Freq Control* 1997; 44: 1010-7.
17. Goss SA, Johnston RL, Dunn F. Comprehensive compilation of empirical ultrasonic properties of mammalian tissues. *J Acoust Soc Am* 1978; 64: 423-57.
18. Goss SA, Frizzell LA, Dunn F. Ultrasonic absorption and attenuation in mammalian tissues. II. *J Acoust Soc Am* 1980; 68: 93-108.
19. Daum DR. A large scale phased array ultrasound system for non-invasive surgery of deep stated tissue. PhD dissertation, Massachusetts Institute of Technology, Cambridge, MA, 1998.
20. AIUM. *Acoustic output labeling standard for diagnostic ultrasound equipment*. Laurel, MD: Author, 1998.
21. IEEE. *Guide for medical ultrasound field parameter measurements*. New York: Author, 1990.
22. Hurwitz MD, Kaplan I, Svensson GK, Hansen J, Hynynen K. Feasibility and patient tolerance of a novel transrectal ultrasound hyperthermia system for treatment of prostate cancer. *Int J Hyperthermia* 2001; 17: 31-7.
23. Fleury G, Berriet R, Le Baron O, Huguenin B. New piezocomposite transducers for therapeutic ultrasound. *Workshop on MRI-guided Focused Ultrasound Surgery* 2002: 39.
24. Sanghvi NT, Foster RS, Bihrl R, Casey R, Uchida T, Phillips MH, Syrus J, Zaitsev AV, Marich KW, Fry FJ. Noninvasive surgery of prostate tissue by high intensity focused ultrasound: an updated report. *Eur J Ultrasound* 1999; 9: 19-29.
25. Chapelon JY, Ribault M, Birer A, Vernier F, Souchon R, Gelet A. Treatment of localised prostate cancer with transrectal high intensity focused ultrasound. *Eur J Ultrasound* 1999; 9: 31-8.
26. Hynynen K, Pomeroy O, Smith DN, Huber PE, McDannold NJ, Kettenbach J, Baum J, Singer S, Jolesz FA. MR imaging-guided focused ultrasound surgery of fibroadenomas in the breast: a feasibility study. *Radiology* 2001; 219: 176-85.
27. Quesson B, de Zwart JA, Moonen CT. Magnetic resonance temperature imaging for guidance of thermotherapy. *J Magn Reson Imaging* 2000; 4: 525-33.
28. McDannold NJ, Jolesz FA, Hynynen KH. Determination of the optimal delay between sonications during focused ultrasound surgery in rabbits by using MR imaging to monitor thermal buildup in vivo. *Radiology* 1999; 211: 419-26.
29. Daum DR, Hynynen K. Thermal dose optimization via temporal switching in ultrasound surgery. *IEEE Trans Ultrason Ferroelectr Freq Control* 1998; 45: 208-15.

**Optimized Hyperthermia Treatment of Prostate Cancer Using an Intracavitary  
Ultrasound Array**

Osama M. Al-Bataineh<sup>1</sup>, Robert M. Keolian<sup>2</sup>, Victor W. Sparrow<sup>3</sup>, Douglas Mast<sup>2</sup> and  
Nadine Barrie Smith<sup>1,3</sup>

<sup>1</sup>Bioengineering Department  
<sup>2</sup>Applied Research Laboratory,  
<sup>3</sup>Graduate Program in Acoustics  
The Pennsylvania State University  
University Park, PA 16802

To be submitted to the Journal of Acoustical Society of America in January 2004.

Please send correspondence to:  
Osama M. Al-Bataineh, M.S.  
Department of Bioengineering  
The Pennsylvania State University  
313 Hallowell Building  
University Park, PA USA 16802  
TEL: 001-814-865-8087 FAX: 001-814-863-0490  
omabio@engr.psu.edu

## **1. Introduction**

Prostate cancer causes about 30,000 deaths with more than 200,000 new patients in 2003 as reported by the American Cancer Society. Most of the new patients are elderly men that can not withstand surgical procedures to remove the tumor in its early phases. Radiation and chemotherapies are still the treatment of choice for these patients. Radiation therapy attacks the cancerous cells using external focusing techniques or internally using permanent seed implants (brachytherapy) while chemotherapy delivers the lethal drug to the tumor cells directly using the blood stream. However, the anatomy of tumors and cancer environment reveals that the core of the tumor is deprived of blood supply; that delivers oxygen and nutrition that maintain the biological activities of the cancerous cells (Overgaard et al. 3-20). These cells are acidic, hypoxic and do not proliferate like the cells at the periphery of the tumor. The acidic microenvironment of the core of the tumor is caused by the switching of these cells to anaerobic energy production in order to survive in this harsh environment. The acidity has direct effect on the normal biological activity of proteins caused by a change of their three-dimensional shape in such an environment. The core of the tumor is found to resist both radiation and chemotherapies because these cells tend not to proliferate and have little blood supply. Compared to the core of the tumor, however, the outer shell has cells that are supplied with many blood vessels which function well to serve the growth of cancer, i.e. proliferation and production of the chemical signals that induce the body to produce additional blood vessels to supply the tumor, diverting blood to the needs of the tumor at the expense of organs such as prostate gland. The outer cells are found to be a good target for both radiation and chemotherapies because of their relatively normal micro-environment.

Temperature has a great effect on the biological behavior of normal cells. Any change in the cell temperature will lead to a dramatic change to the three-dimensional shape of the proteins reducing the biological activity of these proteins and the overall behavior of the cell itself (Maurieb E.N.). The combined effect of acidity and increased temperature will tend to denature the proteins of tumor core cells and prevent them from continuing their survival under such a harsh microenvironment. Intracavitary ultrasound thermal therapy (Buchanan and Hynynen 1178-87;Diederich and Hynynen 626-34;Hurwitz et al. 31-37;Hutchinson E.B. and Hynynen K. 1032-42;Smith, Buchanan, and Hynynen 217-25) has been found to be appropriate in such cases to help in the killing of cancerous cells in conjunction with radiation or chemotherapies. Cancer of the prostate or the benign enlargement of the gland can be targeted using a controlled ultrasound intracavitary phased array to attack the core of the tumor and to weaken its shell as an adjuvant for radiation or chemotherapies. The design of a hyperthermia array to induce these beneficial effects of increased tumor temperature should take in consideration the anatomical and physiological properties for the rectum, prostate gland, seminal vesicles and the surrounding tissue.

The design, construction and optimization of a transrectal intracavitary ultrasound array for the hyperthermia treatment of prostate cancer will be introduced in this paper. Four linear phased arrays are arranged in a special geometry that insures the effectiveness of the therapy, as determined by an anatomical computational model based on data from the Visible Human Project. The  $k$ -space computational method is used to simulate wave propagation in an inhomogeneous large scale three-dimensional human prostate model that takes into consideration sound speed, density and acoustic absorption variations of each soft tissue type that compose the prostate gland and the surrounding tissue.

## **2. Materials and Methods**

### **2.1 Three-dimensional Human Prostate Model**

In order to optimize and control the driving parameters of the phased array to uniformly heat the entire prostate, an anatomically and acoustically accurate model was built utilizing the photographic data from the Visible Human Project. The appropriate photographs were located and downloaded into local storage area in order to collect the required three-dimensional (3D) prostate model. Photoshop software was used to read the RAW images and to save them into an appropriate format (i.e. JPEG format). Forty six slices were chosen that include the prostate gland. A proper area from each slice was cut out to build the required 46 images of the 3D model. The actual distance between each slice for the male subject is 1 mm; this distance was found to be unsuitable for simulation of sound wave propagation in megahertz frequencies range. To overcome this problem; three extra slices were created between the consecutive 1 mm slices by averaging the two adjacent images to reduce the distance between consecutive images to 0.25 mm. This resolution was found to be adequate for wave propagation simulations in inhomogeneous mediums for frequencies in the range of 1.2 to 1.8 MHz. One hundred eighty five square images were produced to create the 3D image of the prostate. Each slice has 257 x 257 points.

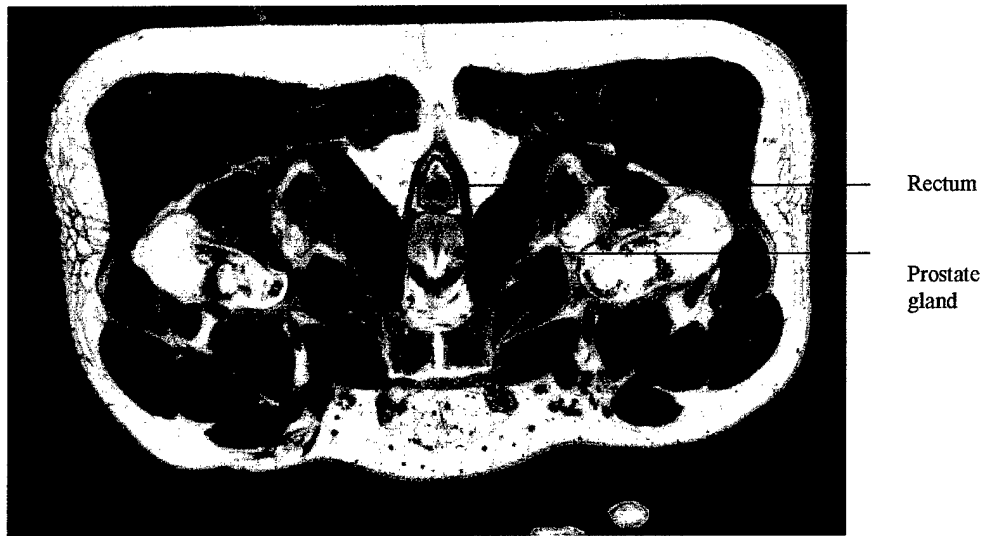


Figure 1. A slice picture from the Visible Human Project showing the rectum and the prostate gland with the surrounding tissue.

The 3D acoustical model was created depending on the optical parameters of each pixel in the actual and averaged images. As shown in figure 1; the surrounding tissue of the prostate gland consists of fat, muscle and connective tissues. Prostate gland consists of compound tubular-alveolar glands embedded in a mass of smooth muscle and dense connective tissue (Maurieb E.N.). The 3D mapped model reads the optical parameters that define the fractional fat, connective, glandular and muscle content of each pixel. Table 1 summarizes the actual acoustical values of these tissues when measured at 37°C. The sound speed in fat and skeletal muscle were found to be 1450 and 1580 m/s respectively measured at 37°C while the density values were found to be 950 kg/m<sup>3</sup> and 1050 kg/m<sup>3</sup> consecutively measured at the same temperature (ICRU). The sound speed in water was calculated depending on this equation; which is valid for fresh distilled water (L.E.Kinsler et al.):

$$c(T) = 1402.7 + 488T - 482T^2 + 135T^3$$

where  $T = 37/100$ .

Sound speed in fresh water found to be 1524 m/s at 37°C and equilibrium atmospheric pressure (1 atm). The density of the fresh water was calculated using this relation (Pierce A.D.):

$$\rho ( 37^{\circ}\text{C} ) = 999.7 - 0.088\Delta T - 0.007(\Delta T)^2$$

where  $\Delta T = 27.0$ ; the density was found to be  $992.0 \text{ kg/m}^3$  at atmospheric pressure and 37°C. These values were compared to the values reported in mast et.al. for fresh water at 37°C an agreement between these data for sound speed was reported, a slight difference in the reported values for water density was shown. Water acoustical values were important to distinguish some of the added blue colored material in the rectum area as shown in figure 1. Sound speed and density values for connective tissue were reported as 1613 m/s and  $1120 \text{ kg/m}^3$  consecutively (Mast et al. 3665-77).

Absorption parameters were calculated for fat and muscle tissues using (ICRU):

$$\alpha ( \text{dB/m} ) = a f^b;$$

the data for a and b at 37°C for fat were 29, 0.9 and for muscle were 74 and 1.0 as reported in ICRU report 61 Table A2. The frequency dependence ( f ) of absorption requires choosing a specific frequency to calculate the absorption; 1.2 MHz frequency was chosen for simulation and design parameters. The absorption values for fat and muscle at 37°C and 1.2 MHz were found to be 0.034 dB/mm and 0.089 dB/mm respectively. The absorption parameter for fresh water calculated at 37°C and 1.2 MHz was calculated using this equation (L.E.Kinsler et al.):

$$\alpha_{\text{water}} = (\omega^2/2\rho_0 c^3) (4.3\mu)$$

where  $\omega$  is the radian frequency;  $\rho$ : density of fresh; c: is sound speed in fresh water;  $\mu$ : coefficient of shear viscosity ( Pa.s ).



As shown in table 1 the absorption of water at 37°C and 1.2 MHz is 0.0347 Np/m which is .0003 dB/mm. The absorption coefficient of connective tissue was found by assuming linear relation between sound speed and absorption coefficients formed using the values of fat and muscle by the least square fitting method; the value was found to be 0.103 dB/mm. The 3D photographic data was used to create three extra sets of 3D acoustical data; which include sound speed variation, density distribution and absorption parameters. Sound speed of each pixel was estimated depending on the fractional optical constituent of water, muscle, fat and connective tissues. The fractional constituent of water was mapped depending on the hue and value of each pixel; while muscle and connective tissues were mapped depending on a combination of saturation and value parameters as follows; these relations were explained elsewhere (Mast T.D. 37-42):

$$\text{Water} \rightarrow W = 1 - [u(0.4 - H) + u(H - 0.8)] + u(0.1 - V)$$

$$\text{Muscle} \rightarrow P = (1 - W) u(0.67 - V)$$

$$\text{Connective} \rightarrow C = (1 - W) u(S - 0.45) - P$$

$$\text{Sound speed } (c) = c_F + (c_0 - c_F)W + (c_P - c_F)P + (c_C - c_F)C$$

where  $u$  is a smoothed step function defined as:

$$u(x) = 0.5 - 0.5\cos[\pi(x+\epsilon)/(2\epsilon)] \text{ for } -\epsilon < x < \epsilon$$

$$u(x) = 0 \text{ where } x < -\epsilon$$

$$u(x) = 1 \text{ where } x > \epsilon$$

$$\epsilon = 0.1$$

Tissue type	Sound speed (mm/ $\mu$ s)	Density (g/cm <sup>3</sup> )	Absorption @ 1.2 MHz (dB/mm)
Connective	1.613	1.120	0.1030
Muscle	1.580	1.050	0.0890
Fat	1.450	0.950	0.0340
Water	1.524	0.992	0.0003

Table 1. The acoustical parameters (i.e. sound speed, density and absorption) of connective tissue, muscle, fat and water when measured 37°C.

Each slice in the original photographic data; which represent a JPEG type image was converted to HSV (hue, saturation and value) image in order to calculate the amount of each tissue constituent for each pixel to apply the previous mentioned relations. Mass density values were mapped depending on empirical linear relations between sound speed and mass density of the values shown in Table 1. Figure 2 shows the relation between sound speed and density for fat, water, muscle and connective tissue; the linear relationship was clearly shown from this figure. Least square fitting method was used to find the linear equation of this relation. The line equation was found to be:

$$\rho = 0.995c - 0.506$$

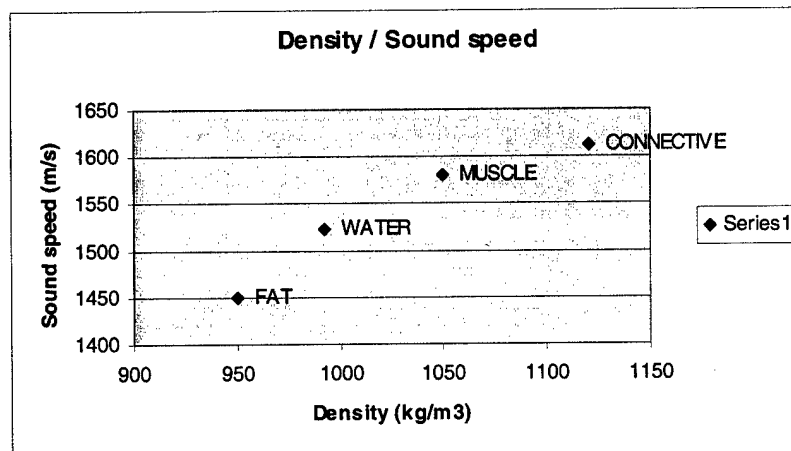


Figure 2. The sound speed and density relationship for fat, water, muscle and connective tissue, a linear relationship could be obtained to relate sound speed and density depending on this figure.

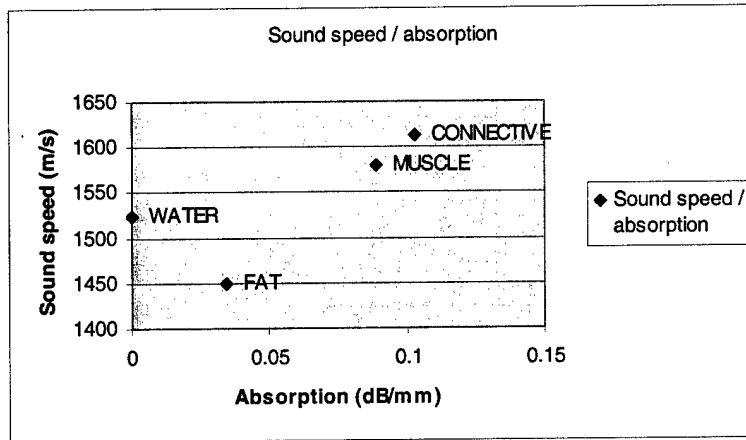


Figure 3. The sound speed and absorption relationship for fat, water, muscle and connective tissue, a linear relationship could be obtained between fat, muscle and connective tissues to relate these acoustical parameters.

Figure 3 shows the relationship between sound speed and absorption parameters for water, fat, muscle and connective tissue; the relation between fat, muscle and connective tissue was clearly shown to have linear relationship. The line equation for these three points was found using the least square fitting method; the equation was found to be:

$$\alpha = 0.423c - 0.58$$

the above equations were used to create three 3D data sets for sound speed, density variations and absorption parameter depending on an anatomically accurate 3D photographic image of the prostate and the surrounding tissue. These acoustical parameters were used to propagate spherical pulse sound wave to test the model.

## 2.2 Wave propagation using the k-space method

The *k*-space method (Mast et al. 341-54; Tabei, Mast, and Waag 53-63) was found to be appropriate in simulating wave propagation in inhomogeneous mediums using coarse grids while maintaining accuracy. The linear wave equation was used for this simulation depending on the mass conservation, momentum conservation and

state equation to produce the first order coupled propagation equations (Mast et al. 3665-77):

$$\frac{\partial p(x, y, z, t)}{\partial t} + \rho(x, y, z)c^2(x, y, z)\nabla \cdot v(x, y, z, t) = -\alpha(x, y, z)p(x, y, z, t) \quad (1)$$

$$\rho(x, y, z)\frac{\partial v(x, y, z, t)}{\partial t} + \nabla p(x, y, z, t) = 0 \quad (2)$$

from (2), a simplified equation could be written as:

$$\frac{\partial v(x, y, z, t)}{\partial t} = \frac{-\nabla p(x, y, z, t)}{\rho(x, y, z)}$$

by differentiating (1) with respect to time and taking the divergences of (2) the resulted equations are:

$$\frac{\partial^2 p(x, y, z, t)}{\partial t^2} + \rho(x, y, z)c^2(x, y, z)\frac{\partial}{\partial t}\nabla \cdot v(x, y, z, t) = -\alpha(x, y, z)\frac{\partial p(x, y, z, t)}{\partial t} \quad (1')$$

$$\rho(x, y, z, t)\frac{\partial}{\partial t}\nabla \cdot v(x, y, z, t) + \frac{\partial v(x, y, z, t)}{\partial t}\nabla \cdot \rho(x, y, z) + \nabla^2 p(x, y, z, t) \quad (2')$$

rearranging (1') the result is:

$$\frac{\partial}{\partial t}\nabla \cdot v(x, y, z, t) = -\left(\frac{\alpha(x, y, z)}{\rho(x, y, z)c^2(x, y, z)}\frac{\partial p(x, y, z, t)}{\partial t} + \frac{1}{\rho(x, y, z)c^2(x, y, z)}\frac{\partial^2 p(x, y, z, t)}{\partial t^2}\right)$$

substituting the above equation into (2'), the resulted equation after some algebraic steps is:

$$-\alpha(x, y, z)\frac{\partial p(x, y, z, t)}{\partial t} - \frac{\partial^2 p(x, y, z, t)}{\partial t^2} - \frac{c^2(x, y, z)}{\rho(x, y, z)}\nabla p(x, y, z, t)\nabla \rho(x, y, z) + c^2(x, y, z)\nabla^2 p(x, y, z, t) = 0$$

the above equation will be referred as equation (3). To write this equation in a form similar to the wave equation, extra algebraic manipulations are needed. The derivation of the divergence of the gradient of the pressure divided by the density is shown bellow:

$$\nabla \cdot \left(\frac{\nabla p(x, y, z, t)}{\rho(x, y, z)}\right) = \nabla^2 p(x, y, z, t) - \frac{\nabla p(x, y, z, t)\nabla \rho(x, y, z)}{\rho(x, y, z)} \quad (4)$$

substituting equation (4) into equation (3) the resulted equation is:

$$\nabla \cdot \left( \frac{1}{\rho(x, y, z)} \nabla p(x, y, z, t) \right) - \frac{1}{\rho(x, y, z) c^2(x, y, z)} \frac{\partial^2 p(x, y, z, t)}{\partial t^2} = \alpha(x, y, z) \frac{\partial p(x, y, z, t)}{\partial t}$$

the above equation will be referred as equation (5), represents the linear wave equation in inhomogeneous medium with absorption parameters included as a virtual source that depend on the time derivative of the pressure multiplied by a frequency independent absorption factor. In order to use the  $k$ -space method to solve for the propagation of sound, equation (5) will be simplified to separate the spatially dependent sound speed and density parameters from the second order derivatives of the pressure with respect to spatial and temporal variables. The next derivation will neglect the absorption term and include it in the effective source terms after the simplification.

The startup equation will be:

$$\nabla \cdot \left( \frac{1}{\rho(x, y, z)} \nabla p(x, y, z, t) \right) - \frac{1}{\rho(x, y, z) c^2(x, y, z)} \frac{\partial^2 p(x, y, z, t)}{\partial t^2} = 0 \quad (6)$$

define the normalized pressure as:  $\psi(x, y, z, t) = \frac{p(x, y, z, t)}{\sqrt{\rho(x, y, z)}}$ , by substitution in eq 6

the result

$$\text{is: } \nabla \cdot \left( \frac{1}{\rho(x, y, z)} \nabla \rho^{1/2}(x, y, z) \psi(x, y, z, t) \right) = \frac{\rho^{1/2}(x, y, z)}{\rho(x, y, z) c^2(x, y, z)} \frac{\partial^2 \psi(x, y, z, t)}{\partial t^2}. \quad \text{This}$$

equation simplifies to:

$$\begin{aligned} \nabla^2 \psi(x, y, z, t) - \rho^{1/2}(x, y, z) \psi(x, y, z, t) \nabla^2 \rho^{-1/2}(x, y, z) &= \frac{1}{c^2(x, y, z)} \frac{\partial^2 \psi(x, y, z, t)}{\partial t^2} \\ \nabla^2 \psi(x, y, z, t) - \frac{1}{c_0^2} \frac{\partial^2 \psi(x, y, z, t)}{\partial t^2} &= \\ \frac{1}{c_0^2} [c_0^2 \rho^{1/2}(x, y, z) \psi(x, y, z, t) (\nabla^2 \rho^{-1/2}(x, y, z)) \psi(x, y, z, t) + \left( \frac{c_0^2}{c^2(x, y, z)} - 1 \right) \frac{\partial^2 \psi(x, y, z, t)}{\partial t^2}] \end{aligned}$$

defining  $q(x,y,z,t)$  and  $v(x,y,z,t)$  functions as follows:

$$q(x, y, z, t) = c_0^2 \rho^{1/2}(x, y, z) \psi(x, y, z, t) \nabla^2 \rho^{-1/2}(x, y, z)$$

$$v(x, y, z, t) = \left( \frac{c_0^2}{c^2(x, y, z, t)} - 1 \right) \psi(x, y, z, t)$$

equation (6) simplifies to:

$$\nabla^2 \psi(x, y, z, t) - \frac{1}{c_0^2} \frac{\partial^2 \psi(x, y, z, t)}{\partial t^2} = \frac{1}{c_0^2} \left( q(x, y, z, t) + \frac{\partial^2 v(x, y, z, t)}{\partial t^2} \right) \quad (7)$$

the above equation can be transformed to the frequency domain easily by 3D spatial Fourier transform as follows:

$$k^2 F(k, t) - \frac{1}{c_0^2} \frac{\partial^2 F(k, t)}{\partial t^2} = \frac{1}{c_0^2} \left( Q(k, t) + \frac{\partial^2 V(k, t)}{\partial t^2} \right) \quad (8)$$

where  $F(k,t)$ ,  $Q(k,t)$  and  $V(k,t)$  are the 3D spatial fourier of  $\psi(x,y,z,t)$ ,  $q(x,y,z,t)$  and  $v(x,y,z,t)$  respectively. Equation 7 satisfies the total wavefield -defined as the summation of the incident and the scattered fields ( $\psi(x, y, z, t) = \psi_i(x, y, z, t) + \psi_s(x, y, z, t)$ ) - and the scattered wavefield as well.

However, the incident wavefield is satisfied using the homogeneous wave equation:

$$\nabla^2 \psi_i(x, y, z, t) - \frac{1}{c_0^2} \frac{\partial^2 \psi_i(x, y, z, t)}{\partial t^2} = 0$$

in order to solve for the inhomogeneous medium (i.e. to include both the incident and the scattered wavefields) a new auxiliary source was introduced as  $w(x,y,z,t) = \psi_s(x,y,z,t) + v(x,y,z,t)$ . Substitution of this new term in equation 8 resulted in this simple equation:

$$\frac{\partial^2 W(k, t)}{\partial t^2} = k^2 c_0^2 [W(k, t) - V(k, t)] - Q(k, t) \quad (9)$$

where

$$V(k, t) = \mathbb{F} \left[ \left( 1 - \frac{c^2(x, y, z)}{c_0^2} \right) (\psi_i(x, y, z, t) + w(x, y, z, t)) \right]$$

$$Q(k, t) = c_0^2 \mathbb{F} \left[ \sqrt{\rho(x, y, z)} \nabla^2 \rho^{-1/2}(x, y, z) [\psi_i(x, y, z, t) + w(x, y, z, t) - v(x, y, z, t)] \right]$$

Non-standard finite difference approach was used to solve this equation (Mast et al. 341-54), the discretization of the time derivative term gives:

$$W(k, t + \Delta t) - 2W(k, t) + W(k, t - \Delta t) = 4 \sin^2 \left( \frac{c_0 k \Delta t}{2} \right) \left[ V(k, t) - W(k, t) - \frac{Q(k, t)}{c_0^2 k^2} \right] \quad (10)$$

This k-t propagator (equation 10) is the key equation to solve for the propagation in an inhomogeneous medium after setting the initial and boundary conditions.

A FORTRAN 77 program was used to calculate and simulate wave propagation of sound in 3D inhomogeneous medium. A 6.4 x 6.4 x 4.6 cm<sup>3</sup> model that has 257 x 257 x 185 points was prepared for each acoustical parameter (sound speed, density and absorption); these data were read and processed to be compatible with the mathematical derived model. A tapered absorption boundary layer was created into the absorption data set; simply 25 points were used to create this layer that surrounds the actual model (Mast et al. 341-54).

The laplacian of the inverse square root of density was calculated and stored as data file to reduce repeating this step every time the program runs. A spherical point source that produces spherical waves into the model was placed in the rectum near the absorbing boundary layer to test the model and the numerical simulation method adapted here. It was produced mathematically as a Gaussian source in both space and time spaces, this source was added to the effective sources resulted earlier from the derivation and simplification of the *k*-space method and the addition of the absorption dependent term as well. An FFTW (Fastest Fourier Transform in the West)

library was attached the Fortran program to calculate the 3D spatial Fourier transform and the inverse Fourier transform whenever needed.

## **2.3 Ultrasound phased array design and fabrication**

### **2.3.1 One-dimensional phased array**

The idea of one-dimensional (1D) phased array was used to simulate the pressure field in a homogenous medium (i.e. water). Figure 4 shows a linear phased array that consists of 20 elements each has  $1 \times 14 \text{ mm}^2$  dimension, the distance between the adjacent elements shown in the three dimensional enlargement of the first two elements is 0.12 mm. This distance represents the thickness of the blade used to dice the piezo-electric material. Two acoustical matching layers are shown in the figure with quarter wavelength thickness; these layers improve the efficiency of the transducer and serve to keep the elements aligned and connected together as one unit. The first matching layer was chosen to be conductive to ease the soldering of all elements into one ground point as shown in the figure. Each element was soldered to a wire connected to the positive voltage driving source. The linear phased array enables focusing and steering of the pressure in the elevation direction by changing the phase of each element to compensate for the distance from the center of that element to the focal point. Figure 5 shows the steering and focusing mechanism of the phased array. The distance from the center of each element to the focal point is represented by distances  $d_1$  to  $d_{20}$ . In order to compensate for the differences of each path (i.e.  $d_1$  to  $d_{20}$ ) to the path from the center of the array ( $d_0$ ) to the focal point; the phase of the driving source that translate this difference into time delay or shifts is calculated as follows:

$$\phi_i = 2\pi * \frac{(d_i - d_0)}{\lambda}$$



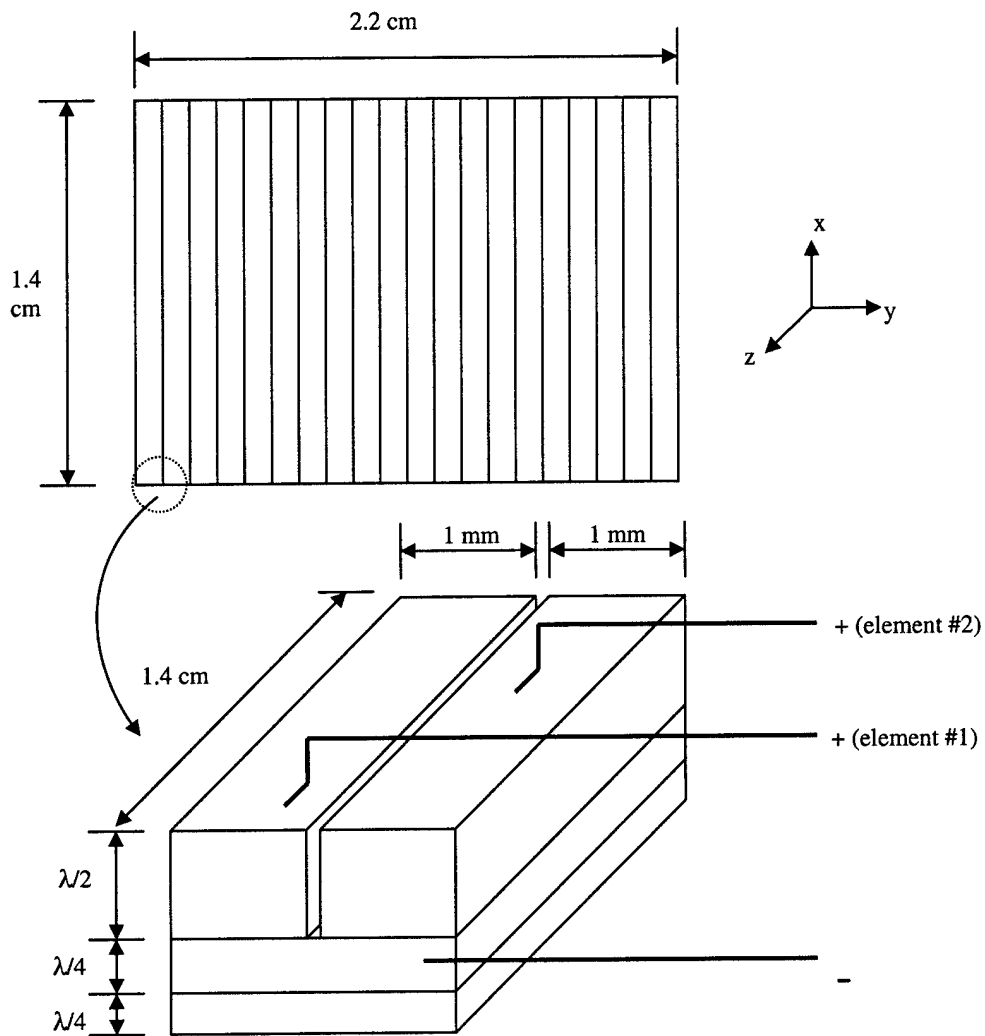


Figure 4. A sketch showing the twenty element linear array (up); an enlarged three dimensional representation of the elements numbered one and two is shown with actual dimensions (down). The distance between these two elements is 0.12 (kerf width); which represents the thickness of the cutting blade.

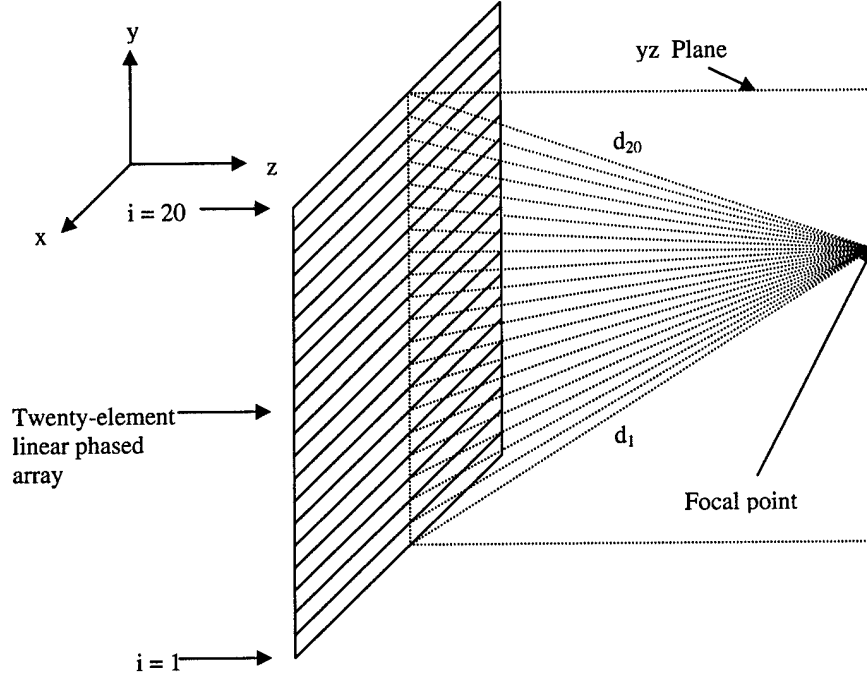


Figure 5. The focusing mechanism is shown for the twenty-element linear phased array. The distances from the center of each element to the focal point ( $d_1$  to  $d_{20}$ ) are used to calculate the phase and time delays for each element to compensate each driving signal in order to have all the propagated sound waves in phase at the focal point to add their amplitudes at that point specifically.

To calculate the pressure distribution in a selected three-dimensional volume, each element of the array was divided into small areas to represent baffled simple sources for pressure calculation at any point in the three-dimensional (3D) volume facing the array. Figure 6 shows the division of each element into small virtual baffled simple sources by equally dividing each element into 50 x 50 sub-elements. The pressure contribution of each baffled simple source is calculated using this equation:

$$p_{imn}(x, y, z) = j\rho c A_{mn} \left( \frac{1}{\lambda d_{mn}} \right) e^{j(\phi_i - kd_{mn})}$$

where;  $p_{imn}(x, y, z)$  : the pressure (Pa) contribution at an arbitrary point (x, y, z) for the baffled simple source of the element  $i$  located at  $mn$  point as represented by Figure 5.

$\rho$  : The density of the medium ( $\text{kg/m}^3$ ).

$c$  : the sound speed in the medium (m/s).

$A_{mn}$  : the area of the baffled simple source ( $\text{m}^2$ ).

$\lambda$  : wavelength of the sound wave (m).

$d_{mn}$  : the length from the center of the baffled simple source ( $mn$ ) to the focal point (m).

$k$  : the wave number (1/m).

$d_0$  : the distance from the center of the array to the focal point (m).

$\phi_i$  : the phase of element  $i$  (rad).

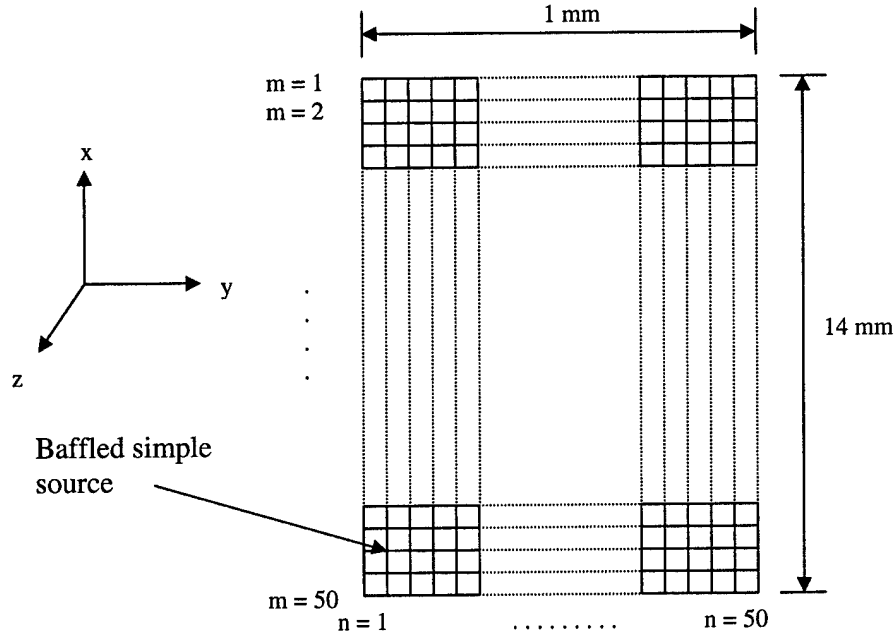


Figure 6. Sketch plot represents one element of the linear array after dividing it into small virtual baffled simple sources. Each element was divided into 50 x 50 sub-elements as shown in xy plane.

Matlab<sup>®</sup> program was written to calculate the phases of each element depending on the previous equations. The program calculates the pressure field in a two-dimensional area facing the transducer after assigning the desired location of the focal point.

### 2.3.2 Ultrasound phased array utilizing the 1D linear array

The proposed design that take in consideration the anatomical measurements of the prostate and the rectal wall is shown in figure 7. Four 1D arrays were arranged as shown; the dimension of the total array including the inactive elements is 56 x 22 mm<sup>2</sup>. This dimension is believed to have the ability to induce the right amount of energy deep inside the prostate gland and at the same time reduces the discomfort for

the patient during the treatment. The inactive elements were added to help fixing the array to an appropriate housing as will be explained later. The inner elements were connected in parallel (i.e. driven with same phases) because of restrictions in the electronics of amplifier system that controls the phase and the power of each element. The array has sixty elements rather than eighty elements that can be controlled during the treatment procedure; the simulation results take in consideration this fact. The focal point of each single one-dimensional array can be controlled separately; while driving power for each sub-element can be controlled independently as well. Many parameters can be controlled for optimization purposes these parameters include amplitude, duty cycle and power changes for each single element as well as phase and time of operation for each individual one-dimensional array. Controlling these parameters for each array and each element individually will enhance this array when optimized for the treatment of prostate cancer.

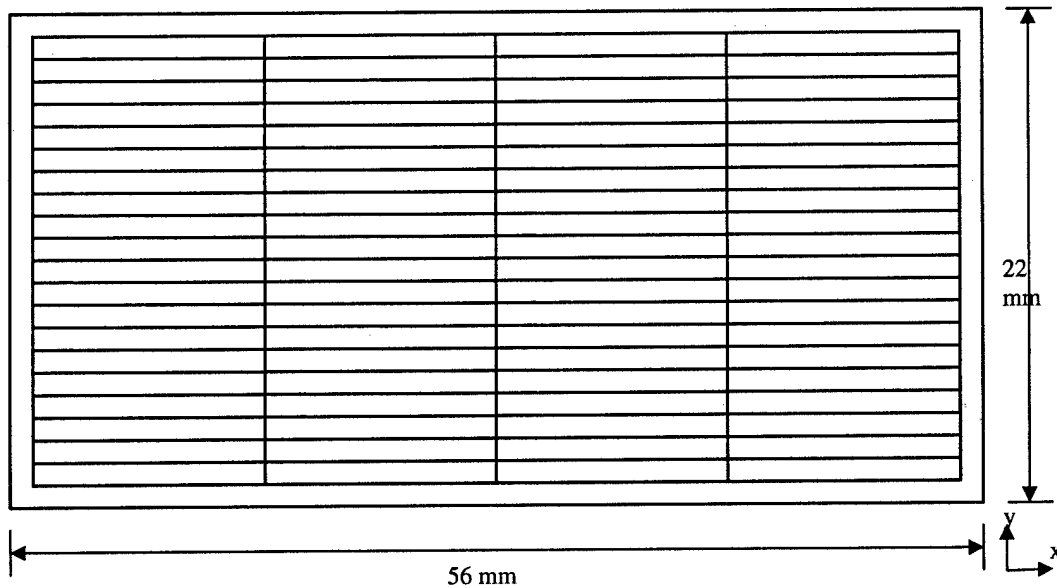


Figure 7. Sketch representation of the 20 x 4 element phased array, the yellow color represents inactive elements while white color represents active ones. The inactive elements were used to fix the array to an appropriate housing.

### 2.3.3 Ultrasound array fabrication

Lead zirconate titanate (PZT-8) (TRS Ceramic, State College, PA, USA) was used to construct the 20 x 4 ultrasound phased array; this kind of PZT is capable of withstanding higher driving electrical powers compared to other materials such as PZT-5a and PZT-4. To increase the transmitted acoustical energy efficiency while delivering sound energy from high acoustical impedance (acoustical impedance of PZT-8 equals 34 Mrayl) to low acoustical impedance of water or soft tissue (acoustical impedance of water is 1.5 Mrayl), two matching layers were built. The choice of these matching layers was done using the KLM model equations that calculate the impedance of quarter wavelength double layers to increase the efficiency of ultrasound transmission between the high acoustical impedance PZT material and soft tissue or water as follows:

$$Z_1 = Z_p^{4/7} \cdot Z_t^{3/7}$$
$$Z_2 = Z_p^{1/7} \cdot Z_t^{6/7}$$

where,  $Z_1$ ,  $Z_2$ ,  $Z_p$  and  $Z_t$  are the acoustical impedances of the first layer, second layer, piezo-electric material and surrounding tissue or medium consecutively. The calculated acoustic impedance for the first layer and second layers assuming water coupling medium are 9.8 and 2.3 Mrayl consecutively.

To construct the double matching layers, parafilm was used to affix an appropriate dimension PZT-8 piece to a glass plate with an adhesive primer poured onto the surface of the transducer face. The piece was surrounded with an epoxy dam and the silver conducting matching layer was poured onto the transducer surface which was prepared using a 2:1 epoxy-to-silver mixture of Insulcast 501 (Insulcast, Roseland, NJ, USA) and 2-3 micron silver epoxy (Aldrich, Milwaukee, WI, USA). The whole assembly was centrifuged for 10 minutes and cured overnight then the

surface of the matching layer was sanded and lapped to the designed quarter wavelength thickness. The second matching layer was prepared in a similar fashion but without any centrifuging mechanism, EPO-TEK 301 part A and part B (Epoxy technology, 14 Fortune Drive, Billerica MA 1821) were mixed using 20:5 mixing ratio to create clear uncured viscous fluid. Another piece of glass was used to spread this mixture on top of the first conductive layer and fixed using appropriate fixtures while cured overnight. The fixture and the second glass piece were removed, another sanding and lapping process was done to reduce the thickness of this layer into the required quarter wavelength thickness. The PZT-8 piece with its two acoustical matching layers was removed from the glass after heating the wax that bonded both of them then diced into 80 elements forming the complete array. The cuts were done by dicing the PZT-8 material 100% through its thickness using a dicing saw (Model 780, K & S-Kulick and Soffa Industries, Willow Grove, PA, USA) at the Ultrasound Therapeutic Application Laboratory on The Pennsylvania State University campus (University Park, PA, USA) with a kerf width of 0.12 mm that represents the thickness of the cutting blade.

Sixty, 28 American Wire Gauge (AWG), 32 ohm miniature coaxial cables (Belden Inc., St. Louis, Missouri, USA), six meter length each and magnetic resonance imaging (MRI) compatible were bundled together to form the connection between the elements of the array and the amplifier system. Each miniature cable was numbered at both sides to ease the soldering and connecting process. Micro-tip soldering pin was used to solder the core of each coaxial cable to its designated element, the soldering temperature was kept below 500°F (less than the Curie temperature of PZT-8) to prevent any damage to the piezo-electric material. With the help of Flux liquid and special soldering material, the soldering of each element was

done for the whole array. Four points of ground were soldered to four different wires directly to the conductive matching layer. These wires then joined together and soldered to the ground points of each coaxial cable to form one ground connection to the whole array.

Special transrectal housing for the array was built in-house (Engineering workshop, University park, PA, USA) using Delrin material that shaped in a cylindrical shape with proper dimensions to fit the array with its 60 coaxial cable and the brass tubes for water and air circulation (figure 7). The water circulation is essential for coupling purposes between the probe itself and the tissue surrounding it; a latex membrane will be used to form a bolus of water surrounding the array. The temperature and flow of the circulated water are controlled using water pump and a chilled icy path within the circulation system.

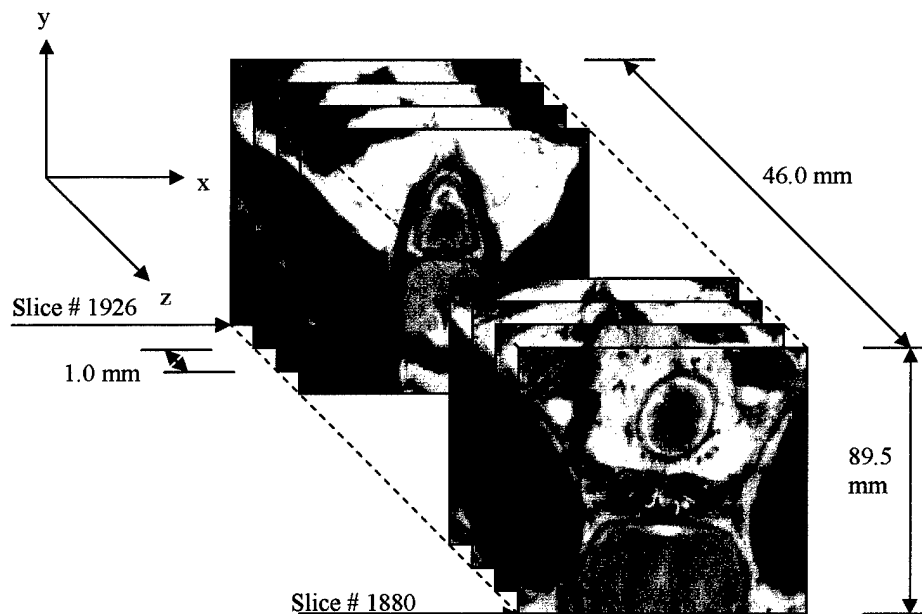


Figure 6. The three-dimensional photograph of the prostate showing 46 slices of 89.5 x 89.5 mm<sup>2</sup> slices with 1.0 mm between each slice. The model starts with slice # 1880 and ends with slice # 1926.

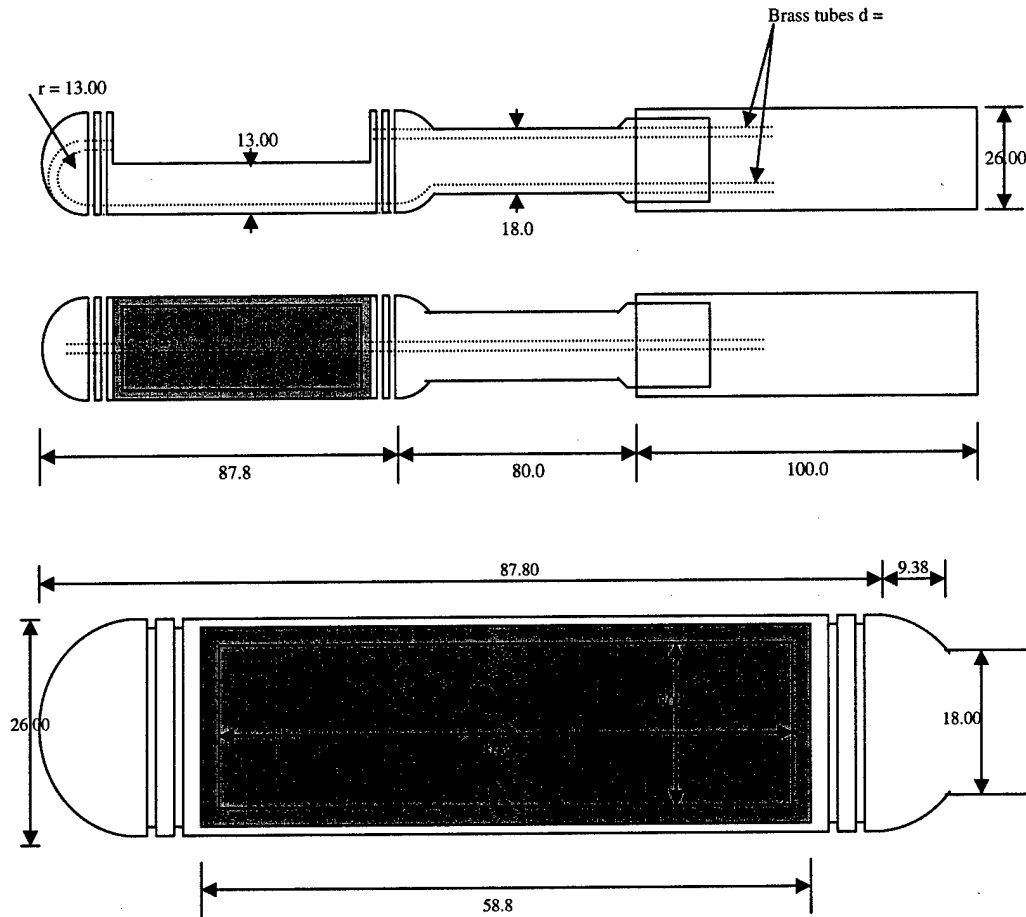


Figure 7. Sketch representation of the transrectal applicator showing side views (up) with enlarged portion (down) that enables fitting of the ultrasound phased array in the colored region.

## 2.4 Temperature simulation

The expected temperature rise caused by the ultrasound energy that absorbed by the tissue was simulated depending on the bioheat transfer equation (Pennes H.H. 93-122):

$$\rho(\vec{r})c_t(\vec{r})\frac{\partial T(\vec{r},t)}{\partial t} = k\nabla^2 T(\vec{r},t) - w(\vec{r})c_b[T(\vec{r},t) - T_a] + q(\vec{r},t)$$

where  $T(\vec{r}, t)$  : tissue temperature ( $^{\circ}\text{C}$ )  
 $c_t$  : specific heat of the tissue ( $\text{J/kg}^{\circ}\text{C}$ )  
 $c_b$  : specific heat of blood ( $3770 \text{ J/kg}^{\circ}\text{C}$ )  
 $\rho(\vec{r})$  : density of the tissue ( $\text{kg/m}^3$ )



$k$  : thermal conductivity ( )

$T_a$  : arterial blood temperature (37°C)

$Q(r, t)$  : power deposited locally in the tissue

$w$  : tissue perfusion ( $\text{kg}/\text{m}^3\text{s}$ ).

The simulation was done in a homogeneous medium (i.e. water) with initial temperature of 37.0°C, the differential equation was solved numerically using finite difference method. A Matlab program was used to simulate the temperature depending on the pressure field generated using the simulated pressure waveform.

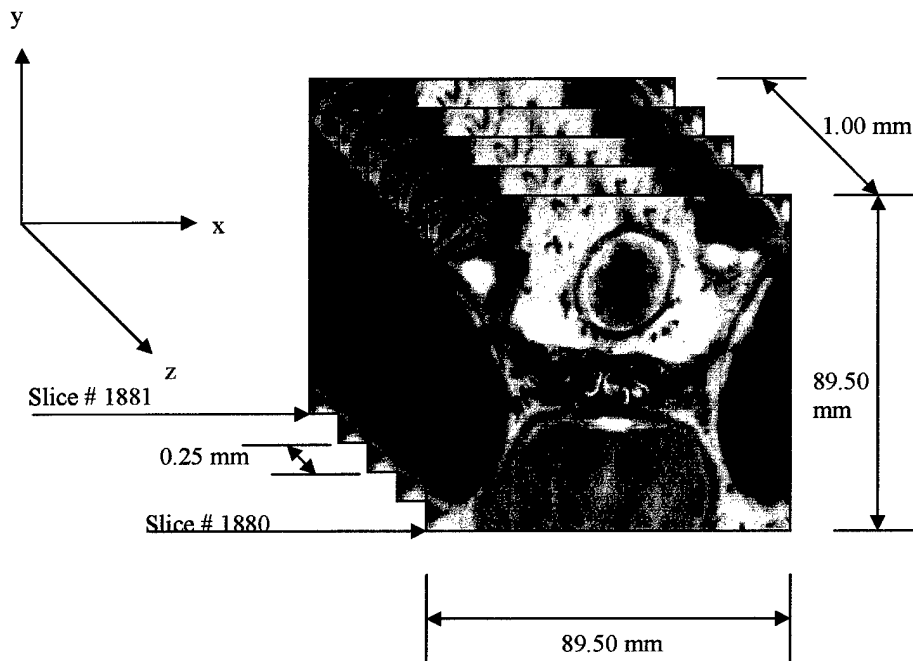


Figure 7. Three averaged slices are shown between slices 1880 and 1881 to reduce the distance between consecutive slices to 0.25 mm. The centered slice was produced by averaging the outer images, while the other two slices were produced by averaging the centered averaged slice with the outer slices.



Figure 8. Slice # 1900, showing the prostate gland with the urethra clearly seen. The gland is surrounded by skeletal and smooth muscles, the rectum is located above the gland while the bladder is beneath it. The rectum is surrounded by connective tissue sheet and embedded in a fat triangular shaped area

### 3. Results

#### 3.1 The 3D human prostate model

A  $359 \times 359 \times 46$  three-dimensional human prostate model is shown in figure 6, this represents a volume of  $89.50 \times 89.50 \times 46.00 \text{ mm}^3$  consisted of 47 slices with 1 mm slice thickness. The 1 mm slice thickness was poor choice for the simulation of wave propagation of megahertz waves, for this reason the model was modified to reduce this thickness to 0.25 mm. Figure 7 shows the creation of three extra averaged slices between each consecutive ones, the centered slice was created by averaging the outer slices as shown in the figure; both slices 1880 and 1881 were averaged to produce another slice located 0.50 mm away from each one. Extra two slices, located at 0.25 mm and 0.75 mm from slice # 1880, were produced by averaging the centered averaged slice with the outer ones. Slice number 1900 is shown in figure 8, the prostate gland with its urethra is shown surrounded from the upper side with the rectum and the urethra from the lower side, an added blue color is shown filling the

cavity of the rectum. A sheet of connective tissue is shown surrounding the rectum and embedded in a triangular shaped fat area. The thigh skeletal muscles are surrounding the prostate gland.

The volumetric image (figures 6 and 7) was mapped to sound speed, density and absorption as shown in figure 9b, c and d respectively. The slice # 1908 is shown in figure 9a, it has dimensions of  $89.50 \times 89.50 \text{ mm}^2$ , Matlab program was executed to generate sound speed, density and absorption depending on the relationships discussed earlier. Figure 9b shows the sound speed mapping of slice # 1908, the sound speed vary through the soft tissue of that image from about 1.4 to 1.6 mm/ $\mu$ s. The blue-colored added material was translated into water as shown from the color bar that gives a sound speed of 1.5 of that area, the skeletal muscle tissue that surrounds the prostate gland is shown to have sound speed of about 1.55. The prostate gland itself is mapped to connective tissue and some fat and muscle tissues, this mapping found to be consistent with the description of the gland that describe it as tubular and alveolar tissues imbedded into smooth muscle and connective tissues (Maurieb E.N.). Some areas of the gland were mapped into fat because of its color that resembles fat rather than any tissue types. The rectal wall was translated into muscle and fat tissues as shown in figure 9b, the connective tissue that surrounds the rectum is shown to have sound speed of about 1.61 mm/ $\mu$ s which resembles connective tissue as expected; the fat area that surrounds the rectum is shown to have some areas that contain connective tissues scattered all over that area. Sound speed of that fat area is found to vary from 1.4 to 1.5. The translation was acceptable when compared to the data obtained in table 1.

Figure 9c shows the density variations through slice # 1908, the density found to vary from about 0.9 to 1.1 gm/cm<sup>3</sup>, compared to the sound speed map this figure

discriminate each soft tissue accurately and found to have good agreement for skeletal muscle, fat, connective tissue and water. Figure 9d shows the absorption variations of the soft tissue of slice # 1908; the absorption found to vary from 0.01 to 0.1 np/mm. The absorption parameters of water, fat, connective and skeletal muscle tissues were found to match those values summarized in table 1 measured at 37°C. Comparing the values of sound speed, density and absorption of various tissues in figures 9b, c and d respectively to the standard values of these soft tissues a good agreement was found through this mapping for the whole three-dimensional model.

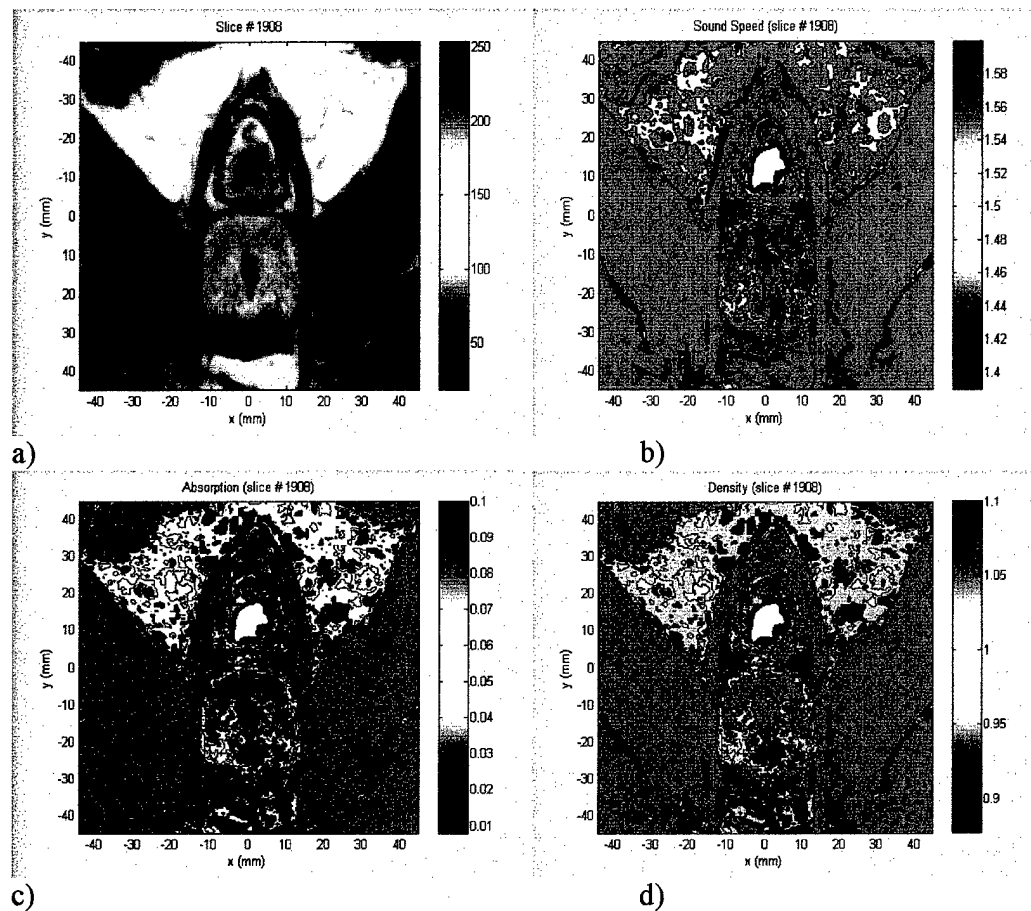


Figure 9. The acoustical mapping of slice # 1908 (a) to density (b) in g/cm<sup>3</sup>, absorption (c) in nipper/cm and sound speed (d) in cm/micros. The added blue colored material in the rectum (a) translated to about 1.00 gm/cm<sup>3</sup>, 0.06 nipper/mm and 1.54 cm/micros representing density, absorption and sound speed respectively. Fat and muscle as shown in the slice were translated with good accuracy to its acoustical parameters compared to table 1.

A smaller three-dimensional acoustical model of the prostate gland was created by reducing the size of each mapped slice from  $89.50 \times 89.5 \times 46.0 \text{ mm}^3$  that has  $359 \times 359 \times 185$  points to  $64.0 \times 64.0 \times 46.0$  that represents  $257 \times 257 \times 185$  points. This reduced model will reduce the amount of memory needed to run the program that propagates sound wave through the whole model.

### **3.2 Wave propagation in inhomogeneous large scale model using the k-space method**

The log-scale gray scale image of the wave propagation in the three-dimensional model is shown in figure 10. The incident wave is shown leading the scattered wavefield produced from the propagation in the inhomogeneous medium. The spherical source was located in the rectum five points away from the absorption boundary layer. The multi-layer image in this figure includes the absorption variations through the central slice of the 3D model as a background. Tapered absorption boundary layer is clearly shown surrounding the whole image. The Fortran program, that produces the 2D gray scaled images of the wave propagation, was designed to create an image every 10 milliseconds. These images then saved as a JPEG image to ease its use using Photoshop or any other photo editors. The calculations were done for the whole model (i.e. 3D calculations), however, to reduce the storage space the middle two-dimensional slice was chosen for image production. The shown image in figure 10 was the middle slice of the model. The scattered as well as the incident waveforms were shown and labeled; at the boundaries of the prostate a noticed reflected wave was shown. Some irregularity of the shape of the wave while crossing the urethra region was shown. This kind of irregularity will complicate the focusing mechanism under such an inhomogeneous medium. However, this figure was

produced to test the accuracy of the model and the computational method rather than focusing issue. The inclusion of the phased array as a sound source into this model will allow us to predict and optimize the pressure wavefield for thermal therapy of the prostate.

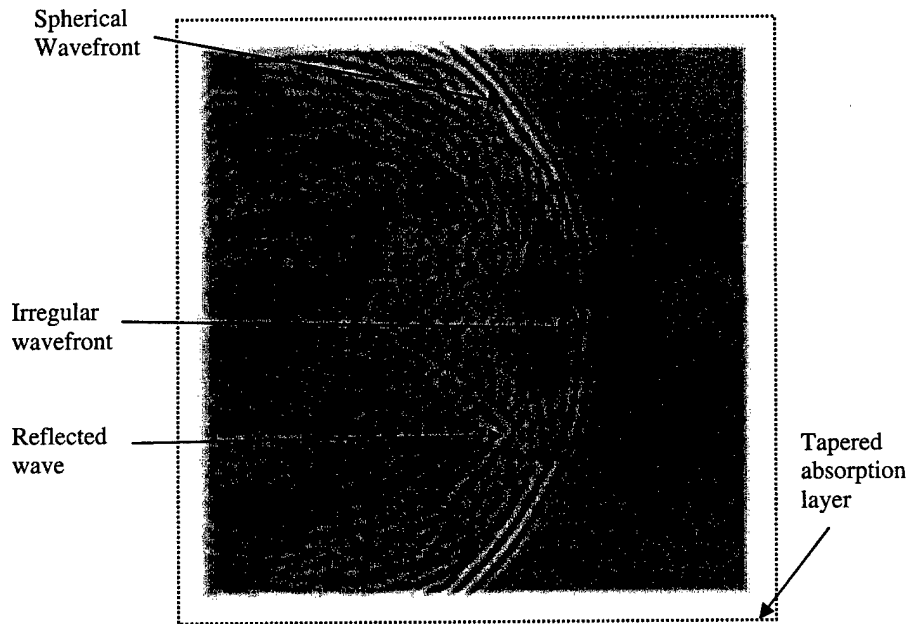


Figure 10: a 2D Gray scaled image showing a background layer of the absorption distribution through middle slice of the 3D prostate model, the tapered absorption boundary layer is shown at the edges with sharp white color. A black dotted line is surrounding the image to distinguish the absorption layer. A spherically propagated wave is shown on top of this background image showing the wave propagation from left to right through the 3D prostate model. The scattered wave is shown following the three cycles wave that has a frequency of 1.2 MHz. Due to sound speed and density changes through this model the wave front is shown with irregular shape while propagating through the urethra area.

### 3.3 Ultrasound array design and fabrication

#### 3.3.1 Pressure and temperature simulation of the array

The pressure wavefield produced by the 20 element 1D phased array is shown in figure 11; while focusing at (0, 0, 4) cm away from the face of the transducer. The figure shows a sketch plot of the 1D phased array with the Cartesian axis shown across the array, two planes are illustrated on that sketch represent the xz and yz planes. The normalized squared pressure distribution is shown in both of these planes. A movie file is included that shows the steering ability of this array, the yz plane was swept with pressure beam while changing the focal point in y-direction. The array is capable of steering from -1.5 to 1.5 cm in that direction; a lower amplitude level grating lobes were shown through the steering process at some specific angles. The destructive interference near the nearfield region was maximized to reduce the thermal effect on the rectal wall and the surrounding tissue while dumping nearly the whole energy deep inside the tissue 4 cm away from the face of the array. However, the grating lobes problem was solved as mentioned earlier by designing a suitable housing of the array that includes water circulation system in order to wash out the effect of these beams and to cool down the rectal wall.

Figure 12 shows the pressure field simulated for the whole array that includes four 1D phased arrays arranged as sketched in the left portion of the figure. The pressure field was simulated while focusing at (0, 0, 4) cm, shown in the right portion are two figures representing the distribution of the normalized squared pressure in xz (up) and yz (down) planes. The whole beam can be steered in the yz plane to help in spreading the required temperature deep inside the prostate gland when placing the whole array inside the rectum. The area near the rectal wall shows the maximum destructive interference that reduces the risk of harming the surrounding tissue. Figure 13 shows contour plots of the normalized squared pressure distribution (up) and the temperature simulation of one minute heating in homogeneous medium (i.e. water)

for the same arrangement shown in figure 12. Many parameters can be varied for this array to achieve an optimal mechanism for the treatment of prostate cancer; these parameters include varying the phases of each linear array separately, altering the power of each array and changing the power of each element disjointedly. These diverse control parameters will improve the treatment and solve many problems when testing the array for *in-vivo* animal experiments under inhomogeneous and variable perfusion tissues.

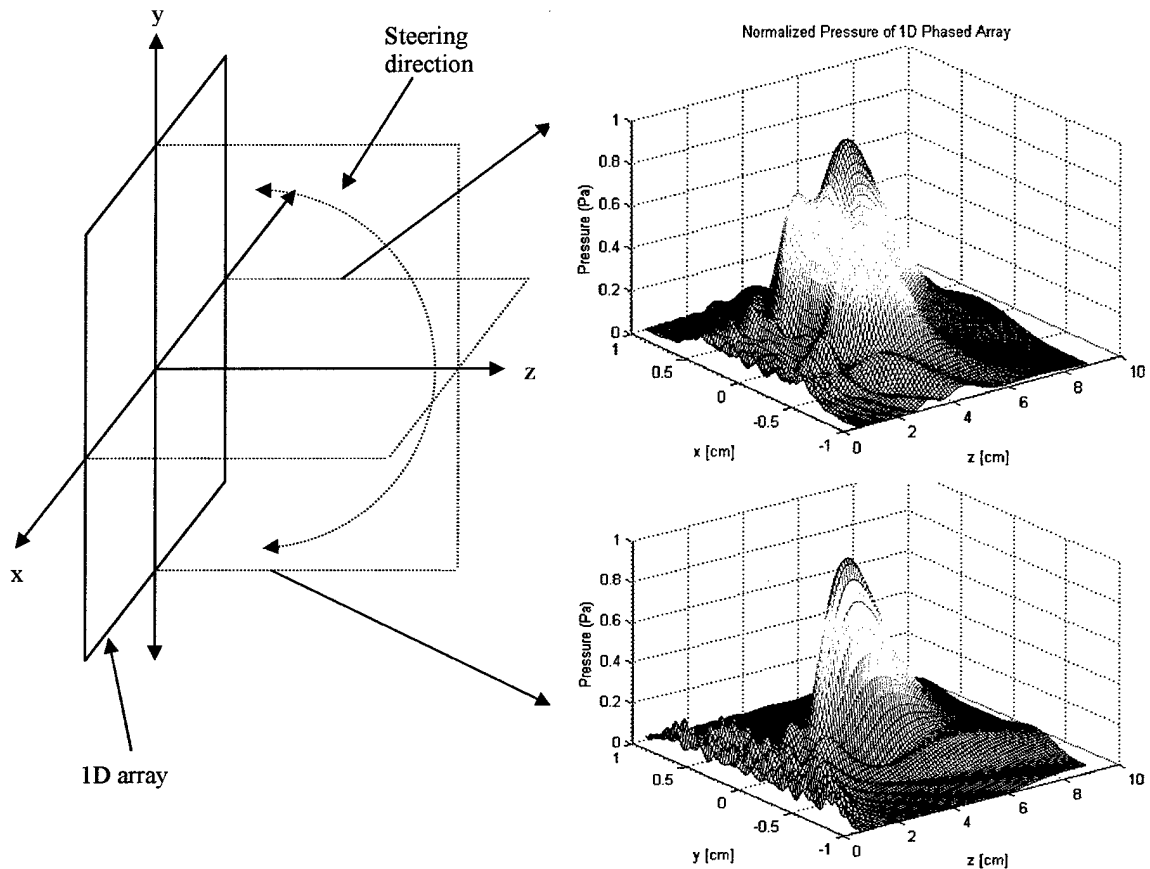


Figure 11: A sketch drawing (left) represents the 1D phased array illustrating the xz and yz planes, the normalized pressure squared distribution through these planes also shown (right). While focusing at (0,0,4) cm, the xy plane pressure distribution is shown in the upper figure and the yz plane pressure distribution is shown in the lower figure.



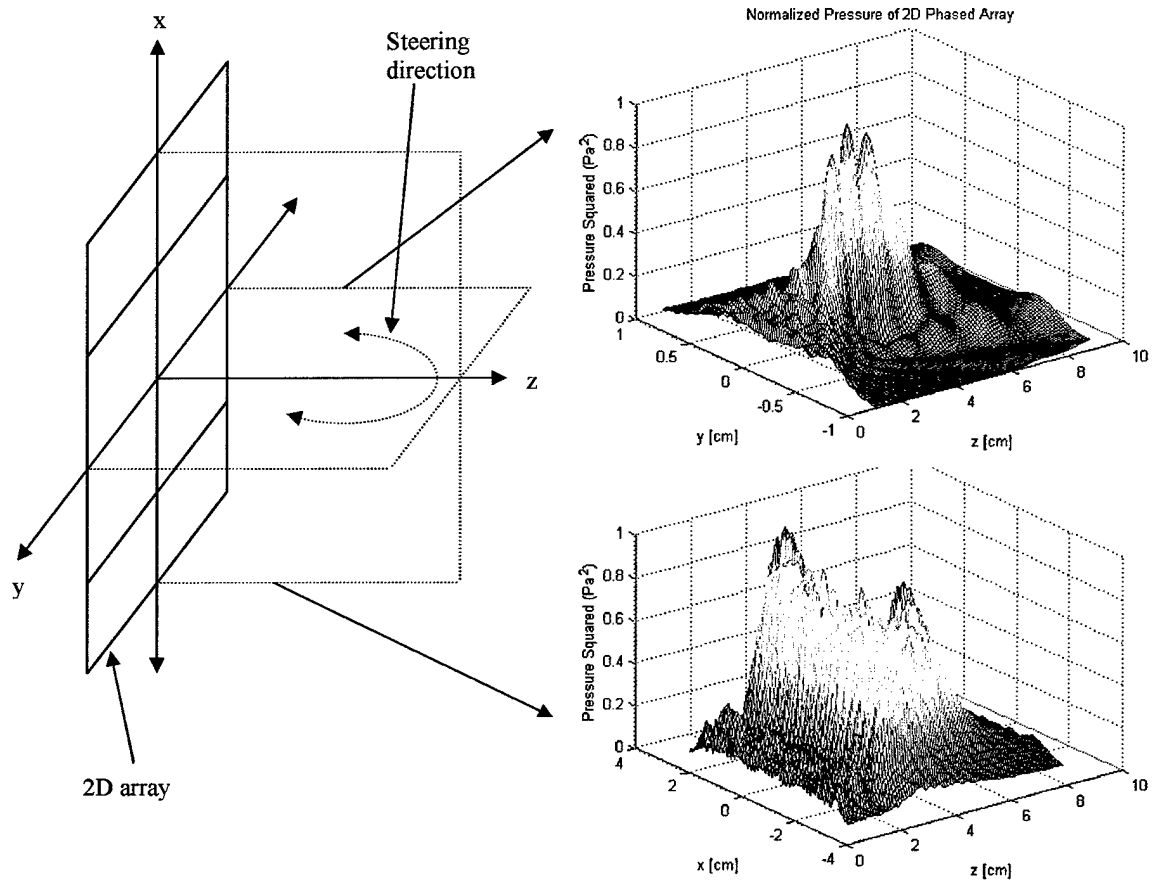


Figure 12: A sketch drawing (left) represents 2D phased array illustrating the xz and yz planes, the normalized pressure squared distribution through these planes also shown (right). While focusing at (0, 0, 4) cm, the yz plane pressure distribution is shown in the upper figure and the xz plane pressure distribution is shown in the lower figure.

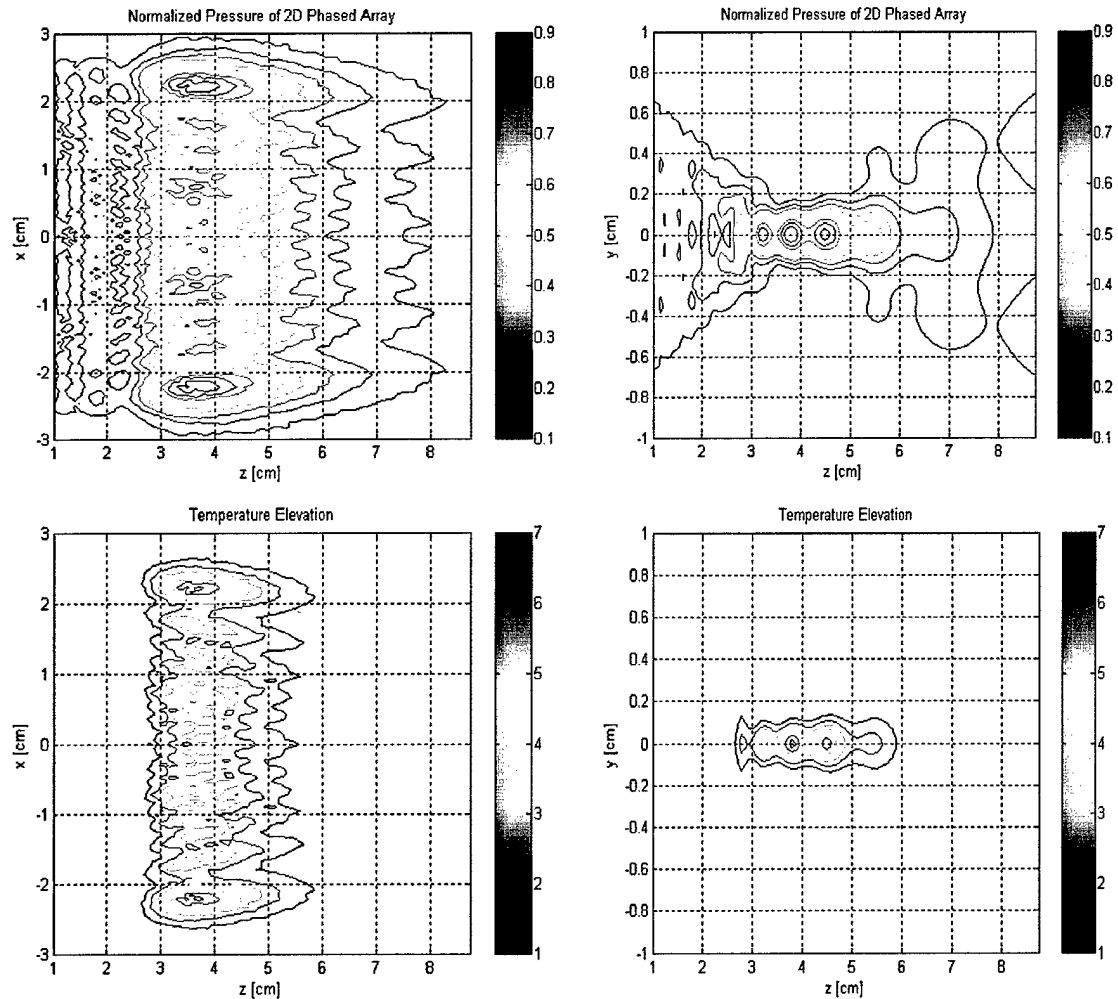


Figure 13: Contour plots showing the pressure distribution in xz and yz planes (up) of the 2D phased array while focusing at (0, 0, 4) cm. Temperature distributions are shown (down) for the mentioned planes after simulating one minute heating of homogenous medium (i.e. water).

### 3.3.2 Ultrasound array fabrication

Figures 14 to 16 show the phased array after building the matching layers and dicing (figure 14) and the soldering of each individual element to a miniature coaxial cable (figure 15). The final product of the transrectal probe is shown in figure 16 that contains 20 x 4 phased array, sixty miniature coaxial cables, four different wires connected to the conductive matching layer that represents the ground connection and suitable brass tubes to complete the water circulation process. The array was snugly

fitted into the housing and bonded using super glue and insulated with water proof insulation material.

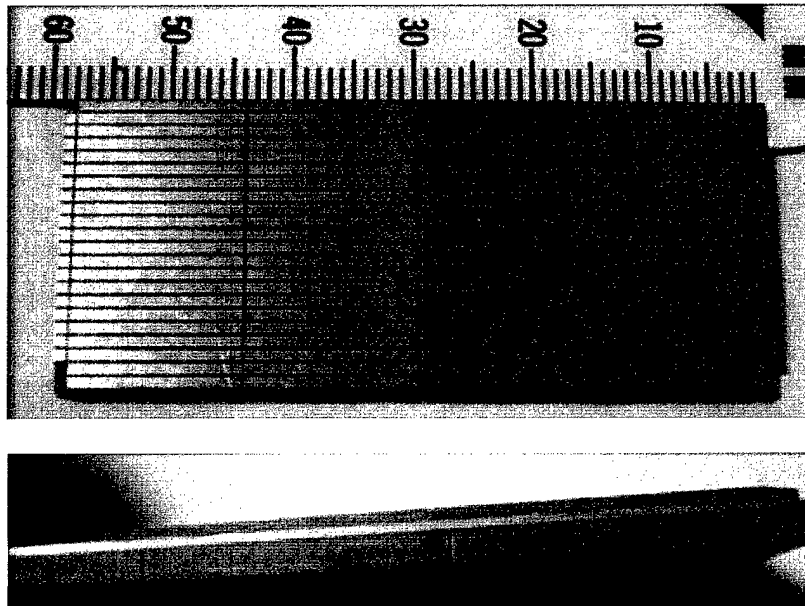


Figure 14: A photo showing the front view (up) of the 20 x 4 element array and the side view (down); the matching layers and the kerf width are shown clearly.



Figure 15: The soldering of sixty miniature coaxial cables is shown; each element of the array was soldered to the core of the coaxial cable. Four points were connected to different points of the conductive matching layer to be soldered to the shield connection of each coaxial cable.

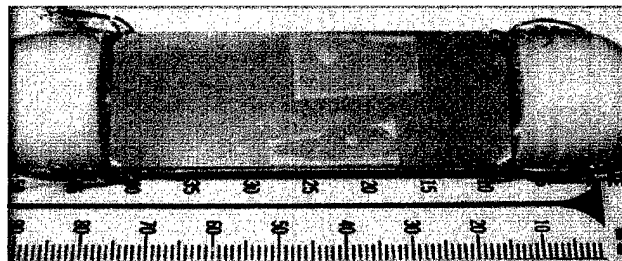


Figure 16: A photograph showing the transrectal probe after assembling the soldered array and the appropriate brass tubes into the MRI compatible housing. The four ground connections are shown at each corner of the array.

#### 4. Discussion

Two main goals were achieved in this study these are the design and fabrication of 20 x 4 element phased ultrasound array and the creation of three-dimensional acoustical model of human prostate for optimization purposes. The designed array is capable of focusing and steering of the pressure deep inside the prostate gland to induce the required thermal dose (see appendix 1) for effective thermal treatment of prostate cancer in conjunction with radiation or chemo-therapies. The optimization of the phased array includes studying the control parameters of the array in an inhomogeneous medium through the simulation of ultrasound wave propagation in the 3D model. However; the tested model needs some modifications to include the designed array as an active source rather than simple spherical one as done for test purposes. The kerf width used in the design of the array was 0.12 mm to enable focusing and steering of the induced pressure beam, this dimension is less than the resolution of the 3D model in which the minimum distance between any consecutive slices was 0.25 mm. To overcome this problem the resolution of the 3D model should be increased to at least 0.125 mm by adding new slice between any consecutive slices. This adjustment could be satisfied by either maintaining the same dimensions of the 3D model while doubling the number of points for the model or by reducing the size of the model while keeping the same number of points of the model. The first solution requires increasing the physical memory of the Dell workstation that handles the calculations (currently 2 GB memory) the calculations time will at least doubled. The second solution may be reasonable for the time being with main drawback that will affect the reality of these calculations when ignoring the surrounding tissue and reducing the size of the array to fit in a reduced model.

Single precision representation of complex and real numbers was used to simulate the wave propagation in the three-dimensional model, for this reason a single precision version of the Fourier transform FFTW also was used. This reduction in number presentation reduces the time of calculations and memory requirements to perform the calculations. The results were acceptable even with this type of representations. The switching to double precision representation of real and complex number put more restrictions on the physical memory used to satisfy this. Single precision works well in such large volume calculations.

Future work will include testing the array in homogeneous medium (i.e. water) by running an exposimetry test to measure the pressure variations in selected two-dimensional areas that face the transducer. These tests will be compared to the simulated pressure fields to verify the accuracy of the design. Ex-vivo experiments will be conducted to measure the temperature increase while changing the amplitude, power and phase of each driving signal. Ultimately, many in-vivo experiments will be carried out while monitoring the temperature elevation using magnetic resonance imaging technique that allows measuring the temperature in an invasive manner. Thermal dose concept will be used to effectively elevate the temperature of the prostate gland to 43°C for thirty minutes to help in destroying the cancerous cells in conjunction of radiation and chemo-therapies.

## **5. Conclusions**

Thermal therapy is good choice to treat prostate cancer adjuvant to radiation and other therapies. Ultrasound phased arrays can achieve this goal in an invasive manner using transrectal probes that takes inconsideration the anatomy and patient comfort in the design. These arrays can be designed and included in realistic computerized models to simulate temperature elevation in a human prostate model. The Visible Human Project is helpful in such cases that provides high resolution images of a sliced cadaver to ease the prostate treatment before even trying the transrectal probe in an animal subjects.

## Appendix 1

### Thermal Dose

The response of cells to heat exposure is exponential relation between temperature and exposure time needed to obtain a given biological effect “from survival curves (Figure 2) (A Westra and W.C.Dewey 467-77)”. In words, a temperature –in most biological systems- rise of 1°C requires halving the exposure time to achieve the same level of effect above 43°C, whereas below this temperature the time must be reduced by a factor of 3-4; this relation could be mathematically modeled as (Sapareto S.A. and Dewey W.C. 787-800)

$$t_1 = t_2 * R^{(T_1 - T_2)}$$

Where;  $R = 0.5$  for  $T > 43^\circ\text{C}$

$R = 0.25$  for  $T < 43^\circ\text{C}$ .

To compare the heat “dose” accumulated by tissues subject to a complex heating regime with the dose they have experienced if the temperature had been held at 43°C, an equivalent time  $t_{43}$  is calculated as (Sapareto S.A. and Dewey W.C. 787-800):

$$t_{43} = \int_{t_1}^{t_f} R^{43 - T(t)} dt$$

Where  $t_1$  and  $t_f$  are the initial and final times of the heating procedure. Thermal doses are often quoted in terms of  $t_{43}$ .

The values of R were found from the thermodynamics of heat inactivation and the absolute reaction rates –i.e. calculating the number of molecules reacting per second- theory; which is stated bellow:

“Every elementary rate process, what ever it’s nature – diffusion, solubility, oxidation, hydrolysis, many excitations, lubrication, etc.- can be treated as an unstable equilibrium between the reactants, in their normal state, and the activated complex, in the activated state. The activated complex is an intermediate molecule with a life of  $10^{-13}$  sec. Once formed, it decomposes with a universal frequency  $kT/h$ , which is the same for all reactions (T: Absolute temperature,  $k$ : Boltsman constant and  $h$  is plank’s constant). The probability that the formation of the activated complex will lead to reaction is designated by the transmission coefficient  $\kappa$  which is often equal to 1.” (F.H.Johnson, H.Eyring, and M.Palissar 3-460)

In many reactions the specific rate constant  $k'$  as accounted for on the basis of a quasi-equilibrium between the normal and the activated state ( $K^\ddagger$ ) and the frequency of decomposition of the activated complex times the probability that the activated complex decomposes to the products (F.H.Johnson, H.Eyring, and M.Palissar 3-460):

$$k' = \kappa(kT/h) K^\ddagger$$

$$K^\ddagger = e^{-\Delta F^\ddagger/RT} = e^{-\Delta H^\ddagger/RT} e^{\Delta S^\ddagger/R}$$

Where,  $\Delta F^\ddagger$  is the free energy

$\Delta H^\ddagger$  is the heat energy (cal/mole)

$\Delta S^\ddagger$  is the entropy of inactivation (cal/degree/mole).

The specific reaction rate  $k'$  is:

$$k' = \kappa(kT/h) K^\ddagger = \kappa(kT/h) e^{-\Delta H^\ddagger/RT} e^{\Delta S^\ddagger/R}$$



Since the survival curves of the experimental data could be represented by Arrhenius equation; which is (F.H.Johnson, H.Eyring, and M.Palissar 3-460; Sapareto S.A. and Dewey W.C. 787-800):

$$k' = 1/D_0 = Ae^{-\mu/RT}$$

Where;

A: Arrhenius constant

$\mu$ : Activation energy

R: universal gas constant

T: absolute temperature

$D_0$ : is the time required to reduce the survival percentage by 1/e on the exponential portion of the survival curve.

By comparing these two equations:

$$A = \kappa(kT/h) e^{\Delta S^\ddagger/R} \cong 2.05(10^{10})T e^{\Delta S^\ddagger/2}$$

$$\mu = \Delta H^\ddagger$$

$1/D_0 = Ae^{-\Delta H^\ddagger/2T}$  (A is constant as the temperature changed from 43°C to 46°C for Chinese Hamster Ovary cells (CHO) where  $\Delta S = 374.5$  &  $\Delta H = 141000$ )

The Arrhenius plot (Figure 2) is relating the inverse of inactivation values to the inverse of absolute temperature values as follows (A Westra and W.C.Dewey 467-77):

$$\ln 1/D_0 = \ln A - \Delta H/2T$$

The relative decrease (R) in  $D_0$  for a 1°C increase in temperature is related as:

$$R = (D_0 \text{ for } T+1)/(D_0 \text{ for } T) = e^{-\Delta H/2T(T+1)}$$

So, for the CHO where  $\Delta H = 141000$  (cal/mole) and T varies between 37°C and 46°C (316 – 319°K) R will be:

$$R \cong e^{-.690} \cong 0.50 \text{ (the change in temperature is not that effective)}$$

Determinations of R have been reported for a number of biological systems and endpoints. The values reported range from 0.4 to 0.8 above 43°C, with 0.5 being the most frequent value. There have been fewer studies below 43°C; however, in general the R-value is approximately a factor of 2 smaller than that above 43°C (W.Dewey et al. 463-74).

The survival curves indicate that the inactivation was sigmoidal in response, i.e. shoulder followed by a straight-line exponential portion. The inactivation rate is equal to  $1/D_0$ , where  $D_0$  is defined as the treatment time required reducing the survival on the exponential part of the curve to 37 per cent (i.e.  $1/e$ ) of an initial value. A comparison of the  $D_0$  values observed for different temperatures indicate that a 1°C increase in temperature resulted in approximately a two-fold increase in the activation rate (E.Atkinson 487-92).

Thermal dose has been identified as one of the most important factors, which influence the efficacy of hyperthermia. Adequate temperature must be delivered for an appropriate period of time to the entire tumor volume in order to achieve optimal therapeutic results. The inhomogeneity of temperature distribution throughout the tumor volume makes difficult accurate correlations with tumor response and subsequent tumor response and subsequent tumor control (G.Nussbaum).

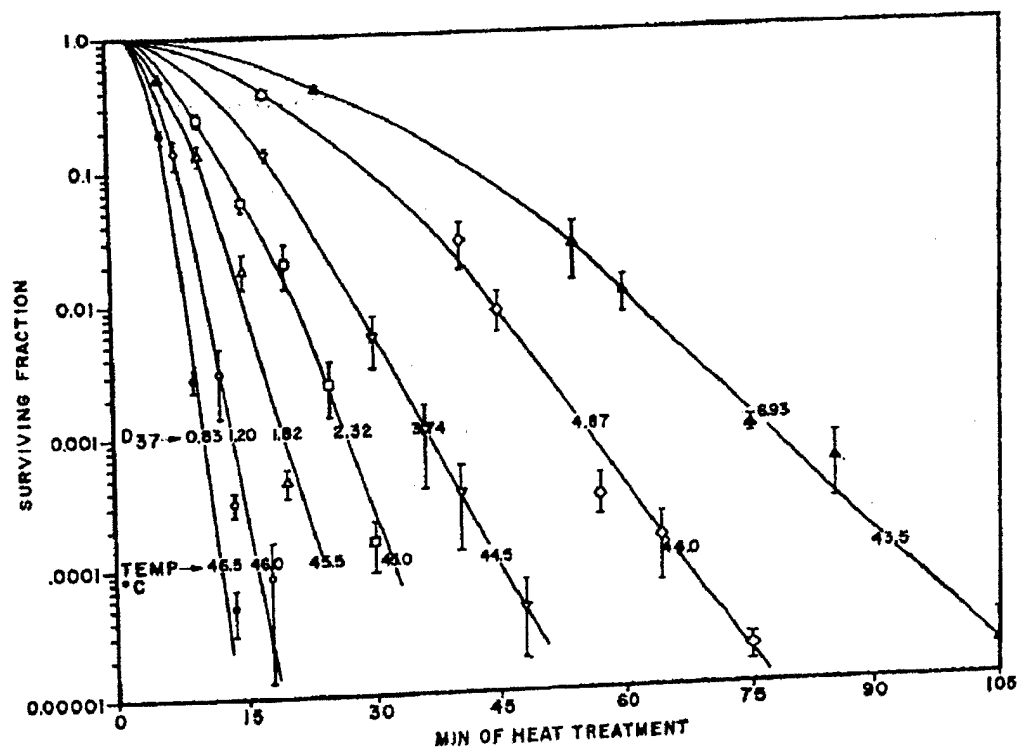


Figure 2. Survival curves for asynchronous hamster cells heated at different temperatures for varying lengths of time. Values for the slopes of the exponential portions of the survival curves are indicated as  $D_{37}$  in minutes of heat treatment.

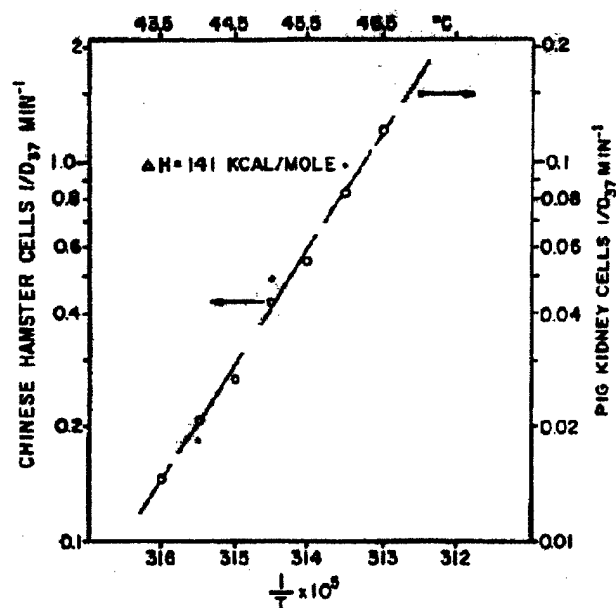


Figure 3. An Arrhenius plot for heat inactivation. On the left ordinate, the reciprocal of the  $D_{37}$  values (inactivation rates) obtained from figure 2 are plotted versus the reciprocal of the absolute temperature. On the right ordinate, similar values are plotted from data obtained by Harris (1967) for pig kidney cells in culture. As calculated in the text, the activation energy,  $\mu$  is 141 kcal/mole for both cell types, but the heat inactivation rates for our hamster cells are a factor of 10 higher than for the pig kidney cells.

## Reference List

- A Westra and W.C.Dewey. "Variations in sensitivity to heat during the cell cycle of Chinese hamster in vitro." Int.J.Radiat.Biol. 19 (1971): 467-77.
- Buchanan, M. T. and K. Hynynen. "Design and experimental evaluation of an intracavitary ultrasound phased array system for hyperthermia." IEEE Trans Biomed Eng 41.12 (1994): 1178-87.
- Diederich, C. J. and K. Hynynen. "The development of intracavitary ultrasonic applicators for hyperthermia: a design and experimental study." Med Phys 17.4 (1990): 626-34.
- E.Atkinson. "Hyperthermia dose definition." J.Bioeng. 1 (1977): 487-92.
- F.H.Johnson, H.Eyring, and M.Palissar. The Kinetic Basis of Molecular Biology. New York: Wiley, 1954.
- G.Nussbaum. Medical Physics Monograph No. 8, Physical Aspects of Hyperthermia. New York: American Institute of Physics, 1982.
- Hurwitz, M. D. et al. "Feasibility and patient tolerance of a novel transrectal ultrasound hyperthermia system for treatment of prostate cancer." Int.J.Hyperthermia 17.1 (2001): 31-37.
- Hutchinson E.B. and Hynynen K. "Intracavitary phased arrays for non-invasive prostate surgery." IEEE Trans Ultrason Ferroelectr Freq Contr 43 (1996): 1032-42.

ICRU, International Commission on Radiation Units and Measurements. Tissue Substitutes, Phantoms, and Computational Modelling in Medical Ultrasound.

Bethesda: Maryland Report 61, 1998.

L.E.Kinsler et al. Fundamentals of Acoustics. 2000.

Mast T.D. "Empirical relationships between acoustic parameters in human soft tissues." Acoustics Research Letters Online 1.2 (2000): 37-42.

Mast, T. D. et al. "Simulation of ultrasonic pulse propagation, distortion, and attenuation in the human chest wall." J.Acoust.Soc.Am. 106.6 (1999): 3665-77.

Mast, T. D. et al. "A k-space method for large-scale models of wave propagation in tissue." IEEE Trans.Ultrason.Ferroelectr.Freq.Control 48.2 (2001): 341-54.

Maurieb E.N. Human Anatomy & Physiology. 5th edition ed. New York: Addison Wesley Longman, 1999.

Overgaard, J. et al. "Hyperthermia as an adjuvant to radiation therapy of recurrent or metastatic malignant melanoma. A multicentre randomized trial by the European Society for Hyperthermic Oncology." Int.J.Hyperthermia 12.1 (1996): 3-20.

Pennes H.H. "Analysis of tissue and arterial blood temperatures in the resting human forearm." Journal of applied physiology 1 (1948): 93-122.

Pierce A.D. Acoustics: An Introduction to Its Physical Principles and Applications. Melville, NY: Acoustical Society of America, 1989.

- Sapareto S.A. and Dewey W.C. "Thermal dose determination in cancer therapy." Int J Radiat Oncol Biol Phys 10 (1984): 787-800.
- Smith, N. B., M. T. Buchanan, and K. Hynynen. "Transrectal ultrasound applicator for prostate heating monitored using MRI thermometry." Int.J.Radiat.Oncol.Biol.Phys. 43.1 (1999): 217-25.
- Tabei, M., T. D. Mast, and R. C. Waag. "A k-space method for coupled first-order acoustic propagation equations." J.Acoust.Soc.Am. 111.1 Pt 1 (2002): 53-63.
- W.Dewey et al. "Cellular Response to combinations of hyperthermia and radiation." Radiation Biology 123 (1977): 463-74.

intensity fluctuations as a function of geophysical time are shown for different positions of the IS with respect to the acoustic propagation path. A theoretical model consisting of internal waves coupled with the acoustic normal modes and horizontal rays is presented. The correlation between

the signal fluctuations and the internal soliton is analyzed using frequency dependent index of refraction. Model results are compared with the SWARM-95 experimental observation. [Work supported by ONR and RFBR Grant No. 03-05-64568.]

WEDNESDAY MORNING, 12 NOVEMBER 2003

TRINITY A ROOM, 8:00 A.M. TO 12:15 P.M.

### Session 3aBB

## Biomedical Ultrasound/Bioresponse to Vibration: Multidisciplinary and Non-Conventional Approaches in Biomedical Ultrasound

Stanislav Emelianov, Chair

*Department of Biomedical Engineering, University of Texas, Austin, Texas 78712*

Chair's Introduction—8:00

### Invited Papers

8:05

**3aBB1. Optoacoustics for biomedical applications.** Takashi Buma, JingYong Ye, Theodore Norris (Ctr. for Ultrafast Optical Sci., 1006 Gerstacker Bldg., Univ. of Michigan, 2200 Bonisteel Blvd., MI 48109-2099), Susanne Milas, Monica Spisar, Kyle Hollmann, Matthew O'Donnell, James Hamilton, Stanislav Emelianov, Lajos Balogh, and James Baker, Jr. (Univ. of Michigan, MI)

We are developing optical techniques to generate and receive ultrasound for various biomedical applications including high frequency 2D arrays, molecular imaging, and microfluidic devices. A 2D synthetic receive array uses a HeNe laser to probe the surface displacements of a thin reflective membrane. Images with near optimal resolution and wide fields of view have been produced at 10 to 50 MHz. A 75 MHz transmitting 2D array element relies on the thermoelastic effect. A 10 ns laser pulse is focused onto a 25  $\mu\text{m}$  thick black polydimethylsiloxane (PDMS) film spin coated on a pure PDMS substrate. Our work in optoacoustic molecular imaging combines ultrafast lasers with high frequency ultrasound. When ultrafast laser pulses are focused into transparent media, laser induced optical breakdown (LIOB) produces acoustic emission and cavitation bubbles. A real-time acoustic technique has been developed to characterize LIOB in dendrimer nanocomposite (DNC) solutions. Lamb waves propagating in thin membranes have found widespread use in microfluidic devices. We use the thermoelastic effect as a noncontact method to generate continuous-wave Lamb waves in gold-coated membranes. We believe these results demonstrate the potential of optoacoustic methods for a broad range of applications in biomedical ultrasonics.

8:30

**3aBB2. Ultrasound-aided high-resolution biophotonic imaging.** Lihong V. Wang (Texas A&M Univ., 3120 TAMU, 233 Zachry Bldg., College Station, TX 77843-3120)

We develop novel biophotonic imaging for early-cancer detection, a grand challenge in cancer research, using nonionizing electromagnetic and ultrasonic waves. Unlike ionizing x-ray radiation, nonionizing electromagnetic waves such as optical waves are safe for biomedical applications and reveal new contrast mechanisms and functional information. For example, our spectroscopic oblique-incidence reflectometry can detect skin cancers based on functional hemoglobin parameters and cell nuclear size with 95% accuracy. Unfortunately, electromagnetic waves in the nonionizing spectral region do not penetrate biological tissue in straight paths as do x-rays. Consequently, high-resolution tomography based on nonionizing electromagnetic waves alone, as demonstrated by our Mueller optical coherence tomography, is limited to superficial tissue imaging. Ultrasonic imaging, on the contrary, furnishes good imaging resolution but has poor contrast in early-stage tumors and has strong speckle artifacts as well. We developed ultrasound-mediated imaging modalities by combining electromagnetic and ultrasonic waves synergistically. The hybrid modalities yield speckle-free electromagnetic-contrast at ultrasonic resolution in relatively large biological tissue. In ultrasound-modulated (acousto)-optical tomography, a focused ultrasonic wave encodes diffuse laser light in scattering biological tissue. In photo-acoustic (thermo-acoustic) tomography, a low-energy laser (RF) pulse induces ultrasonic waves in biological tissue due to thermoelastic expansion.

8:55

**3aBB3. Nonconventional approaches to ultrasonic assessment of skeletal system.** Armen Sarvazyan (Artann Labs., 1753 Linvale-Harbourton Rd., Lambertville, NJ 08530)

Conventional bone ultrasonometry is based on the transmission mode measurement of the linear acoustic parameters of bone (speed of sound and broadband attenuation). It is a well-established technique specifically for osteoporosis diagnostics though it is highly limited in its applications. It cannot be used for the assessment of the hip bone which is the most important area in characterization of the skeletal system and can hardly be used in pediatric applications, particularly in neonatology, for the assessment of newborns and premature and low-birth-weight infants skeletal systems, which became especially vital during the last few decades. There are several new ideas on acoustic assessment of the skeletal sites hardly accessible by the conventional bone ultrasonometry and

3a WED. AM

Best Available Copy



on principles of the acoustic characterization of bone quality, fracture risk evaluation, and monitoring of therapeutic interventions. New approaches are based on the use of the ultrasound radiation pressure for the remote generation of acoustic waves in bones, on the use of various modes of guided acoustic waves having a propagation speed dependent on both the elasticity modulus and the bone thickness, on the use of geometrical dispersion of sound velocity for bone characterization, and the use of principles of nonlinear acoustic spectroscopy for remote bone testing. [Work supported by NIH.]

## Contributed Papers

9:20

**3aBB4. A "Fresnel-transducer" for prostate hyperthermia treatment.** Robert M. Keolian (Penn State Appl. Res. Lab., P.O. Box 30, State College, PA 16804-0030, bonzo@sabine.acs.psu.edu), Osama M. Al-Bataineh, Nadine B. Smith, Victor W. Sparrow (Penn State, University Park, PA 16802), and Lewis E. Harpster (Penn State Milton S. Hershey Medical Ctr., Hershey, PA 17033)

Simulations and construction methods will be described for a novel "Fresnel-transducer." The transducer is designed for transrectal hyperthermia treatment of prostate cancer as an adjuvant to radiotherapy or chemotherapy. Forty nine 6.3 mm diameter 1.5 MHz PZT elements are arranged in a 3 by 7 cm honeycomb-like pattern. They are individually aimed so that their beams partially converge behind the prostate. The increased beam density away from the transducer compensates for the loss of acoustic intensity due to attenuation. The aiming of the beams is additionally biased toward the periphery of the heated region to compensate for cooling from lateral heat conduction. The elements are divided into three interspersed sets, each driven at a slightly different frequency, to minimize stationary Moire interference bands between the beams. The combined effect is to uniformly raise the prostate temperature to 43 °C without overheating the rectal wall. [Research supported by the Department of Defense Congressionally Directed Medical Prostate Cancer Research Program.]

9:35

**3aBB5. Vibration characteristics of implants.** Ahmed M. Al-Jumaily (Diagnostics and Control Res. Ctr., Auckland Univ. of Technol., Auckland, New Zealand, ahmed.al-jumaily@aut.ac.nz), Mostafa Fatemi, and James F. Greenleaf (Ultrasound Res. Lab., Mayo Clinic and Foundation, Rochester, MN 55905)

Vibro-acoustography is a technique that uses the radiation force of amplitude-modulated ultrasound to evaluate the dynamic response of an object at the modulation frequency. One potential application of this technique is to assess the reaction of the host tissue to the implant material by evaluating the mechanical properties of the tissue surrounding the implant. To do this, we use vibro-acoustography to measure the frequency response of the implant, and use this information to evaluate the mechanical parameters of the surrounding. Two theoretical models are developed to study the dynamic response of an implant in tissue. The first model is for an implant (1×25-mm steel beam) fully embedded in a viscoelastic medium (tissue). The second model is for a partially embedded implant with one part exposed to the open environment. The exposed end is rigidly connected to a base, and the other end is freely embedded in the viscoelastic medium. At the interface between the two media matching of boundary conditions is achieved to determine the force response. For both models eigenvalues and eigenfunctions are determined and transfer functions are evaluated. The first two natural frequencies compare well with available experimental and finite-element data.

9:50

**3aBB6. Sector array transducers for vibro-acoustography.** Glauber Silva, Shigao Chen, Randall Kinnick, James Greenleaf, and Mostafa Fatemi (Mayo Clinic and Foundation, Rochester, MN 55905)

Vibro-acoustography is an imaging technique that maps the acoustic response of an object to a localized harmonic radiation force. This force is generated by two interfering continuous-wave ultrasound beams at slightly different frequencies  $f_1$  and  $f_2$ . The system point-spread function (PSF) is related to the radiation force on a point-target. Imaging artifacts depend on the PSF sidelobes, which can be reduced by mismatching the sidelobes of each ultrasound beam. Here, we propose a beamforming approach based

on an 8-element sector transducer with consecutive elements alternately driven at  $f_1$  and  $f_2$ . The transducer generates two ultrasound beam skewed by 22.5° with respect to each other. The system PSF is analytically derived. The theory is validated by experiments using a small steel sphere (radius = 0.2 mm) as a point-target. A laser vibrometer is used to measure the vibration of the sphere and evaluate the PSF of the system. Theoretically, the PSF sidelobes are under -15.8 dB in eight spots circularly distributed and separated by 22.5°, which agrees with the experimental results. Simulation shows that with 16 elements sidelobes are under -35.2 dB. In conclusion, sector transducers for vibro-acoustography may have lower sidelobes as the number of array elements is increased. [Work supported by Grant Nos. EB00535-01, EB2640, and IMG0100744.]

10:05-10:15 Break

10:15

**3aBB7. Radiation force produced by time reversal acoustic focusing system.** Armen Sarvazyan and Alexander Sutin (Artann Labs., Inc., 1753 Linvale-Harbourton Rd., Lambertville, NJ 08530)

An ultrasonic induced radiation force is an efficient tool for remote probing of internal anatomical structures and evaluating tissue viscoelastic properties, which are closely related to tissue functional state and abnormalities. Time Reversal Acoustic Focusing System (TRA FS) can provide efficient ultrasound focusing in highly inhomogeneous media. Furthermore, numerous reflections from boundaries, which distort focusing in conventional ultrasound focusing systems and are viewed as a significant technical hurdle, lead to an improvement of the focusing ability of the TRA system. In this work the TRA FS field structure and radiation force in a transcranial phantom were investigated. A simple TRA FS comprising a plane piezoceramic transducer attached to an external resonator such as an aluminum block was acoustically coupled to the tested transcranial phantom. A custom-designed compact electronic unit for TRA FS provided receiving, digitizing, storing, time reversing and transmitting of acoustic signals in a wide frequency range from 0.01 to 10 MHz. The radiation force produced by ultrasonic pulses was investigated as a function of the transmitted ultrasound temporal parameters. The simplest TRA FS provided focusing of 500 kHz ultrasound pulses and the generation of a radiation force with an efficacy hardly achievable using conventional sophisticated phased array transmitters. [Work supported by NIH.]

10:30

**3aBB8. Effects of transducer and tissue parameters on motion induced by radiation force during ultrasonic lesion monitoring.** Samuel Mikaelian and Frederic L. Lizzi (Riverside Res. Inst., 156 William St., 9th Fl., New York, NY 10038, mikaelian@rriinc.org)

Tissue motion induced by acoustic radiation force is studied as a means of monitoring the formation of therapeutic lesions with increased stiffness produced by high-intensity focused ultrasound (HIFU). Our analyses and simulations examine the role and interplay of various tissue and system parameters to assist in designing practical systems and interpreting results. The radiation force is generated by a therapeutic transducer excited at levels below lesion-production threshold, while the magnitude and time-course of the induced motion is monitored via a confocal and collinear diagnostic transducer. Lesions are detected by comparing pre- and post-treatment motion patterns. Parameters characterizing properties of the motion-inducing beam, such as its intensity and spatial profile, and tissue parameters signifying its viscoelastic properties, acoustic attenuation, and geometry, are the focus of this investigation. Acoustic attenuation, which can increase significantly during lesion production and directly

## A "Fresnel-transducer" for prostate hyperthermia treatment

Robert M. Keolian<sup>\*†</sup>, Osama M. Al-Bataineh<sup>‡</sup>,  
Nadine B. Smith<sup>†‡</sup>, Victor W. Sparrow<sup>‡</sup>,  
Lewis E. Harptser<sup>#</sup>

The Pennsylvania State University

<sup>\*</sup>Applied Research Laboratory,

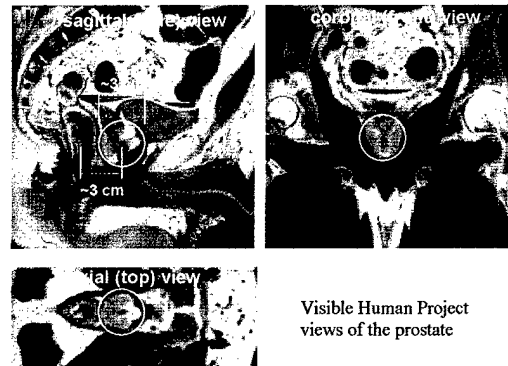
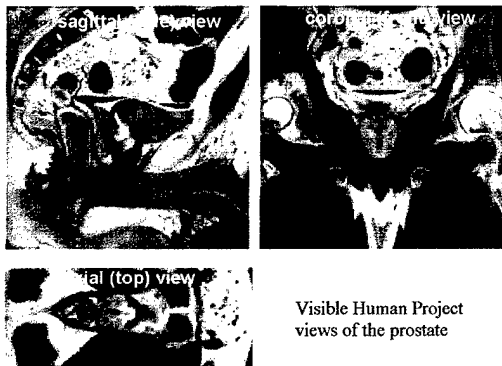
<sup>†</sup>Department of Bioengineering,

<sup>‡</sup>Graduate Program in Acoustics,

<sup>#</sup>Milton S. Hershey Medical Center

## Goal:

- Heat entire prostate if possible
- Increase  $T$  by  $6.0 \pm 1$  °C for 30-60 minutes
- No hot spots
- The entire treatment cannot take too long (about 1 hr)
- Especially sure to heat back (toward rectum) and sides
  - 80% of cancers

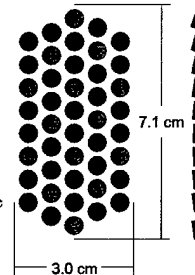


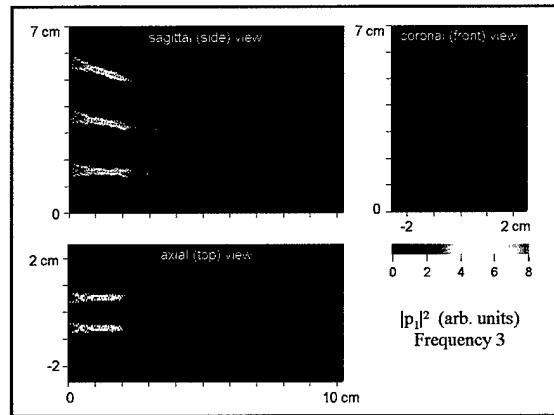
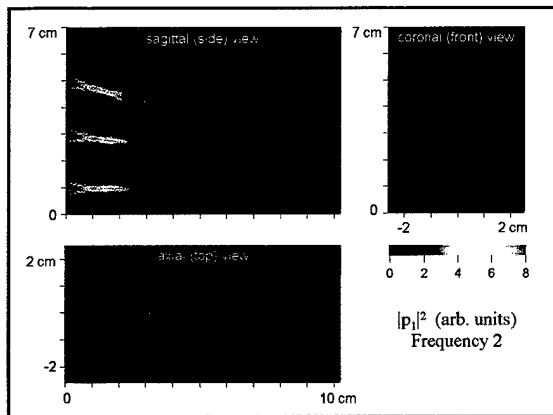
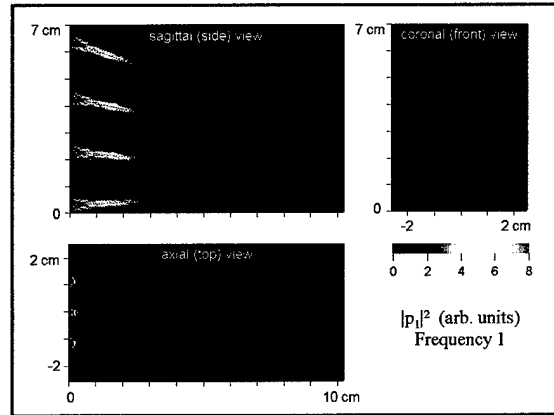
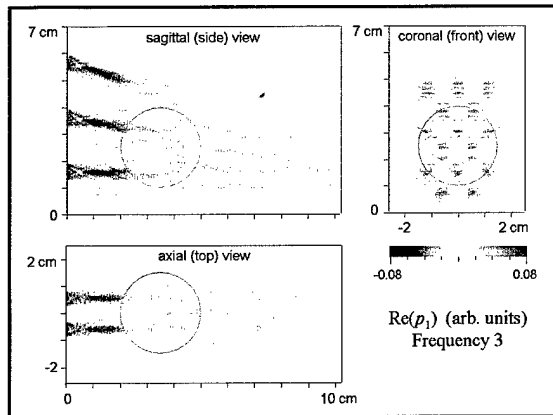
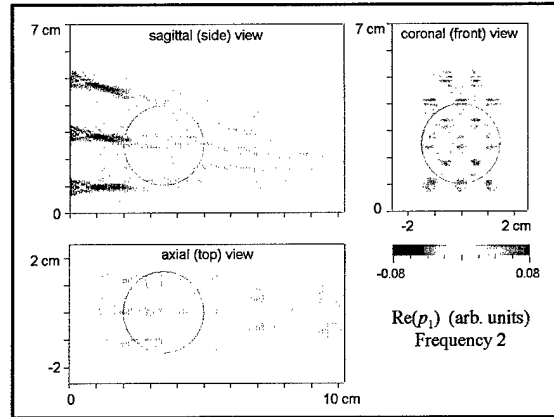
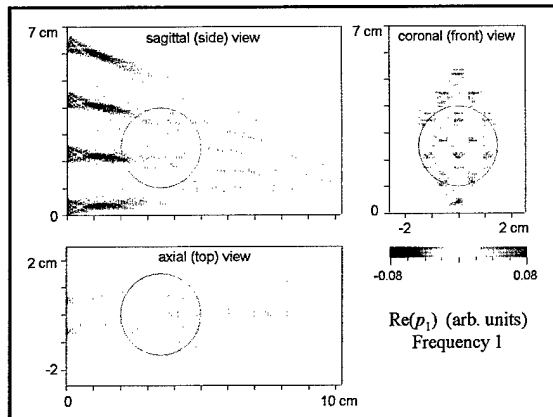
## A problem with steered arrays:

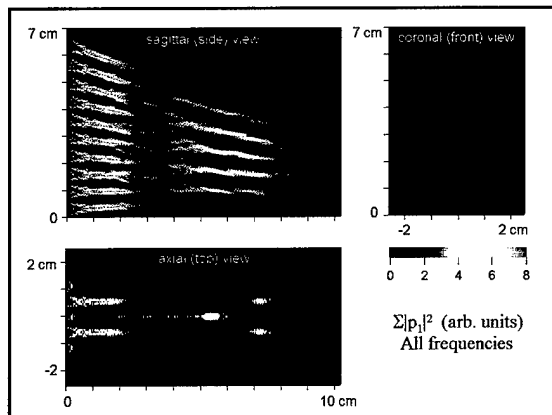
- Need frequency high enough to get absorption in prostate
- Need frequency low enough that sound gets to prostate
- 1-2 MHz good compromise
  - 0.5 to 1 dB/cm attenuation
- Transducer must be big to heat entire prostate all at once
  - more energy at rectum than prostate due to absorption
  - need power/area at rectum  $\leq$  power/area at prostate
- 2D steerable array has thousands of elements at 1-2 MHz
- Aiming individual elements toward prostate center helps
  - less steering angle, so fewer bigger elements
  - but if you're willing to individually aim the elements...

## The Idea:

- Many (44) individual elements
  - individually aimed
- Embrace incoherence
  - honeycomb pattern
  - three different frequencies
  - 3.2 mm diameter elements
  - in 3.3 mm holes in substrate





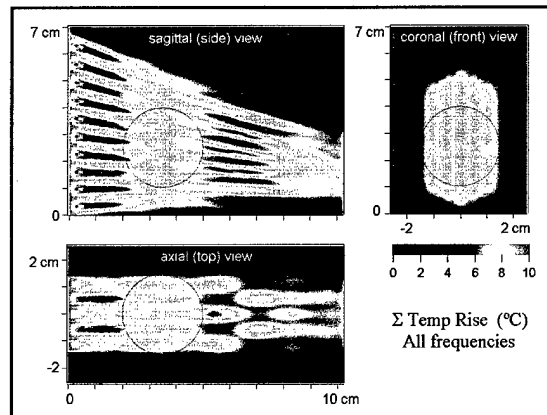
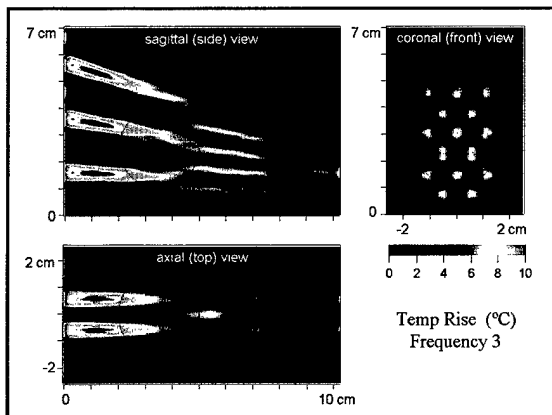
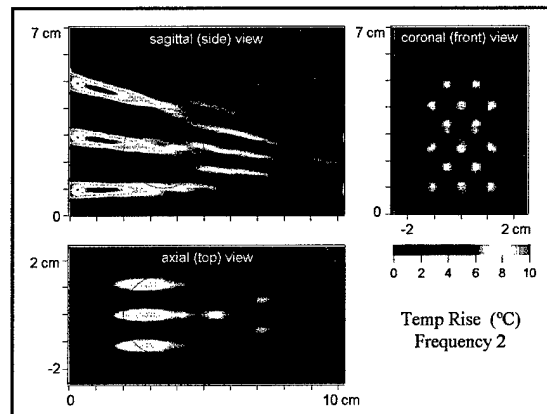
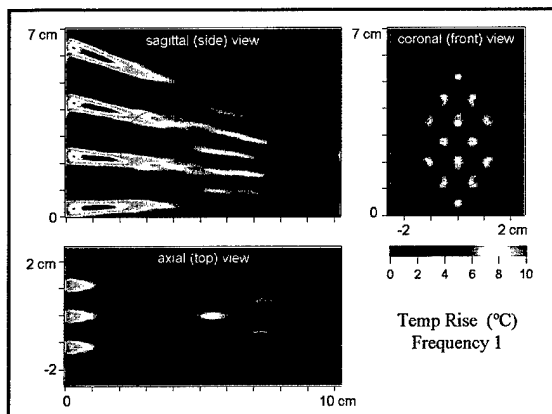


Bio Heat Transfer Equation:

$$\rho c_p \frac{\partial T}{\partial t} = \kappa \nabla^2 T - w c_p T + q$$

$$T = (\text{const.}) \mathfrak{F}^{-1} \left[ \frac{1}{1 + \delta^2 k^2} \mathfrak{F}(q) \right]$$

$$\delta = \sqrt{\frac{\kappa}{w c_p}} = 5.25 \text{ mm}$$



- Can steer individual elements
  - gyrate pattern
- Rotate frequencies
- Sweep frequencies
- Add more frequencies



- Moral:

Instead of lots of little elements of different phases,  
use fewer, bigger elements at different frequencies

### Acknowledgements

This work is supported by the Department of Defense  
Congressionally Directed Medical Prostate Cancer  
Research Program (DAMD 17-0201-0124).

nature of this problem. It is shown that a large number of samples is often required to optimally resolve surface orientation using the optimality criteria of the MLE derived in Naftali and Makris [J. Acoust. Soc. Am. 110, 1917-1930 (2001)].

4:45

**2pAO15. Geocorrection and filtering of 3D bottom images from multi-beam sonar records.** Jerzy Demkowicz, Krzysztof Bikonis, Andrzej Stepnowski, and Marek Moszynski (Gdansk Univ. of Technol., Narutowicza 11/12, 80-952 Gdansk, Poland)

For the last decade multibeam sonars have been increasingly used for mapping and visualization of the seafloor to provide the "physical bases" for environmental studies. Increasing amount of digital (raster) echo

records of high resolution from a multibeam sonar have enhanced the potential of computer modeling of the marine environment to improve our understanding of the bottom processes. However, the 3D bottom images as the result of merging different sonar transects do not comply exact geographical positions and should be corrected. Additionally, the raw sonar records are subject to systematic errors, random noise and outliers. In this paper, Kalman filtering technique to generating optimal estimates of bottom surface from a noisy raw sonar records is proposed. The experiment on the surface indicates that after applying the Kalman filtering the outliers of raw records can be efficiently removed. Moreover, the two-step Kalman filtering method enables 3D seabed visualization in real time. The paper proposes the geographical corrections applied to the merged multibeam sonar transects records. The 3D bottom relief before, and after the filtering method are presented.

TUESDAY AFTERNOON, 11 NOVEMBER 2003

TRINITY A ROOM, 1:00 TO 3:30 P.M.

### Session 2pBB

#### Biomedical Ultrasound/Bioresponse to Vibration: HIFU and Scattering

Ibrahim M. Hallaj, Chair

*Wolf, Greenfield and Sacks, PC, Federal Reserve Plaza, 600 Atlantic Avenue, Boston, Massachusetts 02210*

#### Contributed Papers

1:00

**2pBB1. Synchronization of HIFU therapy system with an arbitrary ultrasound imager.** Neil Owen, Michael Bailey, James Hossack, and Lawrence Crum (Ctr. for Industrial and Medical Ultrasound, 1013 NE 40th St., Seattle, WA 98105)

Synchronization for image guided therapy using high intensity focused ultrasound (HIFU) and imaging ultrasound is achieved with a new technique that uses the focused transducer as a receiver that can detect the acoustic pulses created by the imaging probe. Without synchronization, interference from the high intensity source occludes the imager's display unpredictably, degrading the quality of the system. An imaging probe (Sonosite 180) is registered with a HIFU transducer ( $d=33$  mm,  $roc=55$  mm,  $f=3.5$  MHz) such that the scan line bisects the single element focus. When acoustically coupled through a scattering medium, imaging pulses are passively detected with the HIFU transducer and electronically conditioned into a TTL level trigger. A LabVIEW program uses the trigger to create a pulse width modulated signal that controls the timing of HIFU excitation during treatment. Detection takes less than 1% of the time between displayed images when the imager is running at 20 frames per second. HIFU excitations are programmed to occur such that the single element focus is free of interference when viewed with the imager during treatment. With no electrical connections for this new, simple technique, an arbitrary imager can be selected for synchronized image guided therapy. [Work supported by NSBRI.]

1:15

**2pBB2. Rapid continuous-wave pressure field calculations for spherically focused radiators.** Robert McGough (Dept. of Elec. and Computer Eng., Michigan State Univ., 2120 Eng. Bldg., East Lansing, MI 48824, mcgough@egr.msu.edu)

A new accelerated expression for the continuous-wave pressure field generated by a spherically focused radiator is obtained when the impulse response formulation is transformed and optimized for numerical evaluations. The resulting integral expression converges much more quickly than the impulse response approach, resulting in far fewer function evaluations for the same numerical error. The optimized integral expression is between

two and seven times as fast as the impulse response approach, where the increase in speed depends on the peak value of the specified error. In addition, this new result completely eliminates the cone-shaped regions required for impulse response calculations, so the resulting computer code for the accelerated expression is less complicated than the corresponding code for the impulse response. Results also show that the new expression eliminates the numerical artifact that is encountered near the boundary between regions defined for impulse response calculations. All of these features are useful in thermal therapy computer simulations that employ spherically focused transducer geometries.

1:30

**2pBB3. Design and evaluation of a 63 element 1.75-dimensional ultrasound phased array for treating benign prostatic hyperplasia.** Khaldon Y. Saleh and Nadine B. Smith (Dept. of Bioengineering, 205 Hallowell Bldg., The Penn State Univ., University Park, PA 16802)

Focused ultrasound surgery (FUS) is a clinical method for treating benign prostatic hyperplasia (BPH) in which tissue is noninvasively necrosed by elevating the temperature at the focal point above  $60^{\circ}\text{C}$  using short sonications. With 1.75-dimensional (1.75-D) arrays, the power and phase to the individual elements can be controlled electronically for focusing and steering. This research describes the design, construction and evaluation of a 1.75-D ultrasound phased array to be used in the treatment of benign prostatic hyperplasia. The array was designed with a steering angle of  $\pm 13.5$  deg in the transverse direction, and can move the focus in three parallel planes in the longitudinal direction with a relatively large focus size. A piezoelectric ceramic (PZT-8) was used as the material of the transducer and two matching layers were built for maximum acoustic power transmission to tissue. To verify the capability of the transducer for focusing and steering, exosimetry was performed and the results correlated well with the calculated fields. *In vivo* experiments were performed to verify the capability of the transducer to ablate tissue using short sonications. [Work supported by the Whitaker Foundation and the Department of Defense Congressionally Directed Medical Prostate Cancer Research Program.]

**2pBB4. Optimized hyperthermia treatment of prostate cancer using a novel intravaginary ultrasound array.** Osama M. Al-Bataineh, Nadine B. Smith (Dept. of Bioengineering, The Penn State Univ., University Park, PA 16802), Robert M. Keolian, Victor W. Sparrow (The Penn State Univ., University Park, PA 16802), and Lewis E. Harpster (Penn State Milton S. Hershey Medical Ctr., Hershey, PA 17033)

Localized uniformly distributed ultrasound-induced hyperthermia is a useful adjuvant to radiotherapy in the treatment of prostate cancer. A two-dimensional,  $20 \times 4$  element, transrectal phased-array probe was designed to deliver a uniform and controllable amount of heat directly to the prostate without damaging the rectal wall or surrounding tissue. A three-dimensional prostate model was created using anatomical markers from the Visible Human Project to optimize the array. Sound speed, density, and absorption parameters were mapped to hue, saturation and value of the photographic data to simulate sound propagation through inhomogeneous tissue using the  $k$ -space method. To satisfy the requirements of this method from 1.2 to 1.8 MHz, the grid was adjusted to have 5 points per millimeter in each Cartesian direction. A spherical wave pulse was propagated through the model using tapered absorption boundary conditions. The expected temperature rise due to sound was obtained using the bio-heat transfer equation. Optimal insonification parameters that uniformly heat the prostate to  $43^\circ\text{C}$  for 40–60 minutes were determined for use in the construction of a clinical hyperthermia array. [Research supported by the Department of Defense Congressionally Directed Medical Prostate Cancer Research Program.]

2:00

**2pBB5. Separating thermal coagulation and cavitation effects in HIFU attenuation measurements.** Justin Reed, Michael Bailey, Ajay Anand, and Peter Kaczowski (Appl. Phys. Lab., Univ. of Washington, 1013 NE 40th St., Box 355640, Seattle, WA 98105-6698)

HIFU can be used to destroy tumors. The conversion of acoustic energy into heat causes protein coagulation (Lesion) in tissue. Attenuation measurements have been proposed to monitor the progression of thermal therapy. The goal of this work is to study and separate the effects of cavitation and thermal coagulation in attenuation measurements. A HIFU transducer was used to treat Bovine liver. A receiving transducer mounted across from the transmitting HIFU transducer measured attenuation during the treatment. A pressure chamber provided static pressure greater than the pressure amplitude of the HIFU wave, which suppressed cavitation. rf data from a commercial ultrasound scanner was also obtained. A large increase in attenuation was observed with cavitation present, while a subtle increase in attenuation was observed with cavitation suppressed. Attenuation estimated from the RF data showed an increase in attenuation downstream of the location of the lesion with cavitation present, while a subtle increase in attenuation was observed at the location of the lesion with cavitation suppressed. It has been found that attenuation measurements are greatly affected by the presence of cavitation, and the actual effect of thermal coagulation on attenuation is quite small. [Work supported by NIH, NSF, NSBRI.]

2:15

**2pBB6. Numerical investigation of dual-frequency HIFU pulsing for lithotripsy.** Wayne Kreider, Michael Bailey, and Lawrence Crum (Ctr. for Industrial and Medical Ultrasound, APL, Univ. of Washington, 1013 NE 40th St., Seattle, WA 98105, wkreider@u.washington.edu)

As an alternative to traditional shock-wave lithotripsy, high-intensity focused ultrasound (HIFU) is currently being investigated for its capability to comminute renal calculi. Because current data indicate that cavitation plays a role in both stone comminution as well as collateral tissue damage, the cavitation effects of HIFU treatment strategies are investigated numerically. In particular, numerical simulations are designed to model the response of bubbles to acoustic excitations generated by a prototype, dual-

frequency HIFU transducer for lithotripsy. The prototype transducer is capable of producing both high- ( $\sim 4\text{MHz}$ ) and low-frequency ( $\sim 100\text{-kHz}$ ) outputs, while the bubble dynamics are modeled by the Gilmore equation for a single spherical bubble subject to diffusion. Numerical simulations are currently ongoing to investigate the effects of the relative phase between high and low-frequency pulses. Initial results demonstrate that the simultaneous application of high and low-frequency pulses can generate maximum pressures several orders of magnitude higher than high-frequency pulses alone.

2:30

**2pBB7. The characterization of the lesion growth in time.** Marie Nakazawa, Justin A. Reed, Michael R. Bailey, and Yongmin Kim (Dept. of Elec. Eng., Univ. of Washington, 1400 NE Campus Pkwy., Seattle, WA, nakazawa@ns.cradle.titech.ac.jp)

Thermal heating effects of high intensity focused ultrasound (HIFU) on the dynamics of lesion formation were characterized automatically to assess the role of vapor bubbles in distorting the shape. Tissue mimicking phantom was used in experiments by a 4.2 MHz curve-linear transducer with 44 mm diameter and 44 mm radius of curvature. A variety of HIFU intensities were produced by different amplitudes. Images were acquired by a CCD camera and HDI-1000 ultrasound imager, recorded to VHS, and digitized to measure lesion size and shape. Each image was subtracted with noise reduction in order to detect the HIFU on time and to segment the boundaries of the lesions performed by Matlab programming. Area, length, width, and ratio of lesion area proximal to center line over area distal to center line were calculated along HIFU exposure time. Slight increase in HIFU intensity, means hyperecho forms earlier, and lesion shape change. The data supported the hypothesis that lesion dramatically distorts well after hyperecho with only small increase in HIFU intensity. [Work supported by National Space and Biomedical Research Institute.]

2:45

**2pBB8. Optimization of angular compounding in scatterer size estimation.** Anthony L. Gerig, Quan Chen, and James A. Zagzebski (Dept. of Medical Phys., Univ. of Wisconsin-Madison, 1300 Univ. Ave., Rm. 1530, Madison, WI 53706, algerig@wisc.edu)

Ultrasonic scatterer size estimates generally have large variances due to the inherent noise of the spectral estimates used to calculate size. Compounding partially correlated size estimates associated with the same tissue, but produced with data acquired from different angles of incidence, is an effective way to reduce the variance without making dramatic sacrifices in spatial resolution. This work derives theoretical approximations for the correlation between these size estimates, and between their associated spectral estimates, as functions of data acquisition and processing parameters, where a Gaussian spatial autocorrelation function is assumed to adequately model scatterer shape. Size results exhibit a fair degree of agreement with those of simulation experiments, while spectral results compare favorably with simulation outcomes. Utilization of the theoretical correlation expressions for data acquisition and processing optimization is discussed. Further simplifying approximations, such as the invariance of phase and amplitude terms with rotation angle, are made in order to obtain closed-form solutions to the derived spectral correlation, and permit an analytical optimization analysis. Results indicate that recommended parameter adjustments for performance improvement depend upon whether, for the system under consideration, the primary source of estimate decorrelation with rotation is scatterer phase change or field separation. [Work supported by NIH T32CA09206.]

2p TUE. PM

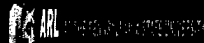
## Optimized Hyperthermia Treatment of Prostate Cancer Using an Intracavitary Ultrasound Array

Osama M. Al-Batanchi<sup>1</sup>, Robert M. Keolian<sup>2</sup>, Victor W. Sparrow<sup>3</sup>,  
Lewis F. Harpster<sup>4</sup> and Nadine Barrie Smith<sup>1,5</sup>

<sup>1</sup>Department of Bioengineering, <sup>2</sup>Applied Research Laboratory,  
<sup>3</sup>Graduate Program in Acoustics, College of Engineering,

<sup>4</sup>Department of Urology, College of Medicine,  
The Pennsylvania State University

507



## Outline

Wave Propagation in 3D Inhomogeneous Models  
k-Space Method  
Human Prostate Model & Wave Propagation  
Pressure & Temperature Simulation  
Ultrasound Array Fabrication  
Conclusions

## Wave Propagation in 3D Inhomogeneous Models

Numerical solution of forward scattering problem using local methods such as finite difference and finite element methods requires fine meshes (10 points per minimum wavelength). 2D simulation is feasible.

Numerical solution using global methods (spectral methods) such as k-space method allows computations to be performed on coarser grids while maintaining accuracy.

Spectral methods require only two points per wavelength for homogeneous mediums; four points per wavelength for inhomogeneous mediums.

## k-Space Method

3D sound wave propagation in prostate model will help in optimizing the driving and control parameters of the designed ultrasound phased array to prevent any "hotspots" while treating prostate cancer.

Linear Acoustic Wave Equation :

$$\nabla \cdot \left( \frac{1}{\rho(x)} \nabla p(x,t) \right) - \frac{1}{\rho(x)c(x)^2} \frac{\partial^2 p(x,t)}{\partial t^2} = 0$$

The spatial differential equations are solved by a simple Fourier Transform method, and temporal iteration is performed using a k-t space propagator.

## Human Prostate Model

Visible Human Project  
3D prostate model

Acoustical parameters for each point (density, sound speed and absorption)

Pressure field simulation (Dell Workstation, Linux 8.0, Fortran 77)



Sound speed

Connective tissue: 1.613 mm/s  
Muscle: 1.547 mm/s  
Fat: 1.478 mm/s  
Water: 1.524 mm/s

## Wave Propagation in the Prostate Model

$f = 1.2$  MHz  
 $257 \times 257 \times 185$  points  
 $6.4 \times 6.4 \times 4.6$  cm<sup>3</sup>  
102 points / inch  
6 points /  $\lambda$   
34 ms



Tapered absorption boundary layer



### 1D Phased Array: Pressure Calculation

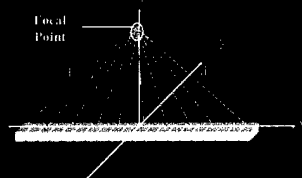
Frequency = 1.2 MHz  
Kerf width = 0.12 mm  
Phased linear array

Pressure contribution for each simple source:

$$p = (X, Y, Z) = \frac{1}{Z} \rho c A_{\text{elem}} e^{-j k \sqrt{Z^2 + (x - x_{\text{elem}})^2 + (y - y_{\text{elem}})^2}}$$

Phase for each element:

$$2\pi \frac{f}{c} \sqrt{Z^2 + (x - x_{\text{elem}})^2 + (y - y_{\text{elem}})^2}$$



### Pressure Field Simulation

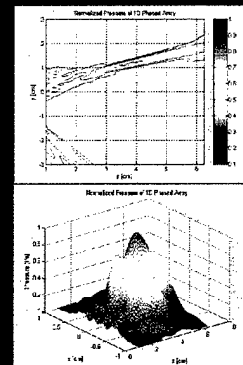
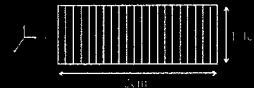
Homogenous medium simulation

Steering of the beam

Focusing deep in the tissue

Destructive interference is maximized through rectal wall

Constructive interference is maximized at the focal point



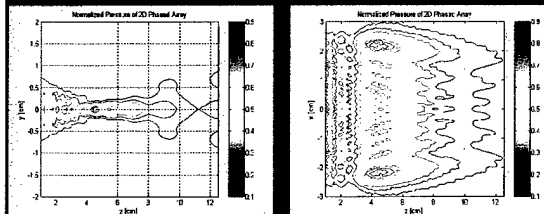
### Pressure Field Simulation

4 x 20 element phased array

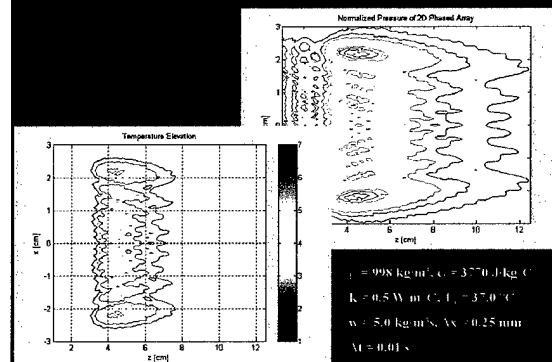
The inner elements were connected in parallel

60 elements, kerf width = 0.12 mm

Frequency = 1.2 MHz, 56 x 22 mm<sup>2</sup>



### Temperature Simulation



### Ultrasound Array Fabrication

PZT 8 (35 ArrayL 300 °C)

Two matching layers (2 - 4)

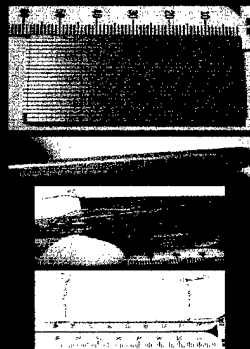
1<sup>st</sup> Silver-polymer composite

2<sup>nd</sup> Epoxy 301

5.6 x 2 cm<sup>2</sup> (1.4 x 2 cm<sup>2</sup>)

60 coaxial cables (l = 6 m)

Water & air circulation



### Conclusions

Intracavitary ultrasound heat therapy provides a noninvasive method to treat prostate cancer

Visible Human Project<sup>®</sup> provides high resolution images for the whole body, which considered helpful in simulation purposes

k-Space computational method is found appropriate to simulate pressure field in 3D large volume models with less storage requirements

Future work: exosimetry and in vivo experiments will validate the k-space approach

### Acknowledgements

This work is supported by the Department of Defense  
Congressionally Directed Medical Prostate Cancer  
Research Program (DAMD 17-0201-0124).

# Fast adaptive control for MRI-guided ultrasound hyperthermia treatment for prostate disease: *in vitro* and *in vivo* results

L. Sun<sup>1</sup>, O. Al-Bataineh<sup>1</sup>, C. M. Collins<sup>2</sup>, M. B. Smith<sup>2</sup>, and N. B. Smith<sup>1,3</sup>

<sup>1</sup>Department of Bioengineering, <sup>2</sup>Graduate Program in Acoustics, Pennsylvania State University, University Park, USA, 16802

<sup>3</sup>Center for NMR Research, Department of Radiology, The Pennsylvania State University College of Medicine, Hershey, PA 17033

## INTRODUCTION

Previous researchers have successfully demonstrated the application of temperature feedback control for thermal treatment of disease using MR thermometry (1-4). Using the temperature-dependent proton resonance frequency (PRF) shift, ultrasound heating for hyperthermia to a target organ (such as the prostate) can be tightly controlled. However, the response of the target to ultrasound heating varies in type, size, location, shape, stage of growth, and proximity to other vulnerable organs. To adjust for clinical variables, a novel adaptive feedback control system has been designed utilizing real-time, on-line MR thermometry by adjusting the output power to an ultrasound array to quickly reach the hyperthermia target temperatures. The advantages of this fast adaptive control method are that there is no need of *a priori* knowledge of the initial tissue properties and it can quickly reach the steady state target temperature by adaptively changing the output power according to the dynamic tissue properties (e.g. thermal conductivity, blood perfusion). To rapidly achieve and manage therapeutic temperatures from an ultrasound array, this research was conducted to utilize closed loop MRI guided temperature control using a novel adaptive feedback system with *in vitro* and *in vivo* experiments.

## MATERIALS AND METHODS

**Fast adaptive MRI control system:** To shorten hyperthermia treatment time, previous researchers have evaluated several control schemes (1, 4, 5). Although the controllers initially operated well, some controllers had undesirable overshoots and oscillations (1, 5). The rapid adaptive control approach used here was designed to track an exponential target temperature with a very fast time constant and to avoid overshoots and oscillations. This robust control system had an ordinary feedback loop composed of the hyperthermia process and a second feedback loop that adjusted the controller parameters (Fig. 1). The mechanism for adjusting the parameters in a model reference adaptive system can be obtained in gradient method by applying Lyapunov stability theory (6). Three dimensional finite difference time domain computer simulations based on Pennes' bioheat transfer equation were conducted to determine the initial values of the control parameters.

**Ultrasound hyperthermia system:** For treatment of prostate disease, the ultrasound hyperthermia system consisted of a transrectal intracavitary array with 16 elements operating at 1.5 MHz. To drive the array, a multi-channel programmable ultrasound phased array driving system operating between 1-2 MHz and capable of 60W per channel was used. Verification of the temperature change within the target used a multi-channel fiber optic (Luxtron®) thermometer probe to provide a reference for the MR temperature map results.

**In vitro and in vivo experiments:** Nine *in vitro* adaptive control experiments were conducted using bovine muscle phantom within the 3 Tesla Bruker S-300 MRI scanner using the ultrasound array. The tissue was coupled to the ultrasound through a circulating water filled bolus surrounding the applicator. MR temperatures in a region of interest (ROI) were selected from the tissue from pre-treatment images were used as feedback thermometry data to the controller. Using rabbit thigh muscle (New Zealand white), *in vivo* animal experiments were conducted using a similar procedure as the phantom experiments with the animal anesthetized using ketamine (40 mg/kg) and xylazine (10 mg/kg). Both the animal and phantom experiments used a 26 cm diameter birdcage coil. For rapid hyperthermia heating, the time constant (target temperature) was selected to be less than 2 minutes for a total experiment of 25 minutes.

**MR temperature imaging:** The proton resonant frequency shift was evaluated by using a spoiled gradient echo (SPGR) sequence with the following imaging parameters: TR = 100 ms, TE = 15 ms, flip angle = 30°, data matrix 64 x 64, field of view (FOV) = 14 x 14 cm, slice thickness = 8 mm and bandwidth = 61.7 kHz. These parameters were chosen to maximize the temperature dependent phase shift, while maintaining a high temporal resolution. A baseline scan was acquired before ultrasound heating and subsequent temperature measurement scans were obtained every 19.7 seconds. Phase subtraction was conducted on-line in real-time to calculate the PRF shift (7). The temperature elevation was obtained using the temperature dependence for muscle  $\alpha(t) = -0.00909$  ppm/°C by averaging temperatures within a 4 x 3 pixel region located at least 1 cm above the bolus-tissue interface.

## RESULTS

Robust adaptive MR temperature control has been demonstrated for both the *in vitro* and *in vivo* experiments. A temperature map (Fig. 2) using phase subtraction images from an *in vivo* rabbit experiment can be seen with a color bar indicating the temperature change within the selected heating ROI from the array below. Since the desired target temperature profile was 38°C for all nine *in vitro* experiments, Fig. 3(a) plots nine averaged MR temperature results (mean  $\pm$  s.d.) which were consistent with the controller target temperature (solid line) and comparable with the Luxtron® results (x-marks). Consistently starting with an initial phantom temperature of 28°C, the controller achieved the steady state temperature within 6 minutes and deviation from the target profile was no greater than  $\pm 1.37^\circ\text{C}$ . Similar to the *in vitro* results, *in vivo* temperature control can be seen in Fig. 3(b) where the rabbit thigh muscle was heated initially from about 36.5°C for 25 minutes. For this experiment, the target temperature was 44.5°C and was achieved in 8 minutes. From other *in vivo* experiments, the maximum variation from the desired temperature profile was  $-3.9^\circ\text{C}$ ; after reaching steady state, tissue temperature was maintained at  $44.5^\circ\text{C} \pm 1.2^\circ\text{C}$ .

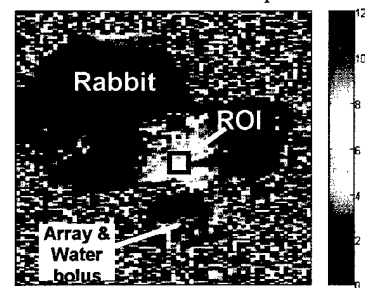
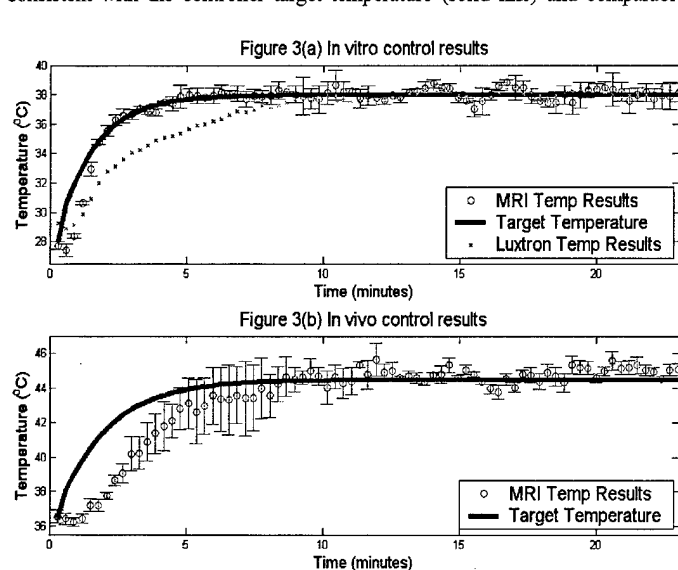


Figure 2

## DISCUSSION AND CONCLUSION

Dynamic MR temperature control for hyperthermia is necessary for fast effective thermal treatments while eliminating the risk of permanently damaging healthy tissue due to overheating. Integration of ultrasound hyperthermia and MR thermometry with robust adaptive control between the modalities has clinical applications. Considering that the accuracy of PFR technique is approximately  $\pm 1^\circ\text{C}$ , the adaptive control system works well to effectively track the reference by adjusting the transducer power according to dynamic tissue properties such as blood perfusion rate. This work was supported by the Whitaker Foundation (RG-00-0042) and the Department of Defense Congressionally Directed Medical Prostate Cancer Research Program (DAMD 17-0201-0124).

## REFERENCES

- (1) F. Vimeux et al, *Invest Rad*, 34,3,1999;
- (2) N. B. Smith et al, *Proc. ISMRM 1999*;
- (3) B. Behnia et al, *MRE*, 15:101-110, 2002;
- (4) R. Salomir et al, *MRM*, 43: 342-347, 2000;
- (5) A. Hartov et al, *Int. J Hyperthermia*, 9, 4, 1993;
- (6) L. Sun et al, *Proc IEEE Ultrasonics Symposium*, 2003;
- (7) A. H. Chung et al, *MRM*, 36: 745-752, 1996

nature of this problem. It is shown that a large number of samples is often required to optimally resolve surface orientation using the optimality criteria of the MLE derived in Naftali and Makris [J. Acoust. Soc. Am. **110**, 1917-1930 (2001)].

4:45

**2pAO15. Geocorrection and filtering of 3D bottom images from multi-beam sonar records.** Jerzy Demkowicz, Krzysztof Bikonis, Andrzej Stepnowski, and Marek Moszynski (Gdansk Univ. of Technol., Narutowicza 11/12, 80-952 Gdansk, Poland)

For the last decade multibeam sonars have been increasingly used for mapping and visualization of the seafloor to provide the "physical bases" for environmental studies. Increasing amount of digital (raster) echo

records of high resolution from a multibeam sonar have enhanced the potential of computer modeling of the marine environment to improve our understanding of the bottom processes. However, the 3D bottom images as the result of merging different sonar transects do not comply exact geographical positions and should be corrected. Additionally, the raw sonar records are subject to systematic errors, random noise and outliers. In this paper, Kalman filtering technique to generating optimal estimates of bottom surface from a noisy raw sonar records is proposed. The experiment on the surface indicates that after applying the Kalman filtering the outliers of raw records can be efficiently removed. Moreover, the two-step Kalman filtering method enables 3D seabed visualization in real time. The paper proposes the geographical corrections applied to the merged multi-beam sonar transects records. The 3D bottom relief before, and after the filtering method are presented.

TUESDAY AFTERNOON, 11 NOVEMBER 2003

TRINITY A ROOM, 1:00 TO 3:30 P.M.

### Session 2pBB

## Biomedical Ultrasound/Bioresponse to Vibration: HIFU and Scattering

Ibrahim M. Hallaj, Chair

*Wolf, Greenfield and Sacks, PC, Federal Reserve Plaza, 600 Atlantic Avenue, Boston, Massachusetts 02210*

### Contributed Papers

1:00

**2pBB1. Synchronization of HIFU therapy system with an arbitrary ultrasound imager.** Neil Owen, Michael Bailey, James Hossack, and Lawrence Crum (Ctr. for Industrial and Medical Ultrasound, 1013 NE 40th St., Seattle, WA 98105)

Synchronization for image guided therapy using high intensity focused ultrasound (HIFU) and imaging ultrasound is achieved with a new technique that uses the focused transducer as a receiver that can detect the acoustic pulses created by the imaging probe. Without synchronization, interference from the high intensity source occludes the imager's display unpredictably, degrading the quality of the system. An imaging probe (Sonosite 180) is registered with a HIFU transducer ( $d=33$  mm,  $roc=55$  mm,  $f=0.5$  MHz) such that the scan line bisects the single element focus. When acoustically coupled through a scattering medium, imaging pulses are passively detected with the HIFU transducer and electronically conditioned into a TTL level trigger. A LabVIEW program uses the trigger to create a pulse width modulated signal that controls the timing of HIFU excitation during treatment. Detection takes less than 1% of the time between displayed images when the imager is running at 20 frames per second. HIFU excitations are programmed to occur such that the single element focus is free of interference when viewed with the imager during treatment. With no electrical connections for this new, simple technique, an arbitrary imager can be selected for synchronized image guided therapy. [Work supported by NSBRI.]

1:15

**2pBB2. Rapid continuous-wave pressure field calculations for spherically focused radiators.** Robert McGough (Dept. of Elec. and Computer Eng., Michigan State Univ., 2120 Eng. Bldg., East Lansing, MI 48824, mcgough@egr.msu.edu)

A new accelerated expression for the continuous-wave pressure field generated by a spherically focused radiator is obtained when the impulse response formulation is transformed and optimized for numerical evaluations. The resulting integral expression converges much more quickly than the impulse response approach, resulting in far fewer function evaluations for the same numerical error. The optimized integral expression is between

two and seven times as fast as the impulse response approach, where the increase in speed depends on the peak value of the specified error. In addition, this new result completely eliminates the cone-shaped regions required for impulse response calculations, so the resulting computer code for the accelerated expression is less complicated than the corresponding code for the impulse response. Results also show that the new expression eliminates the numerical artifact that is encountered near the boundary between regions defined for impulse response calculations. All of these features are useful in thermal therapy computer simulations that employ spherically focused transducer geometries.

1:30

**2pBB3. Design and evaluation of a 63 element 1.75-dimensional ultrasound phased array for treating benign prostatic hyperplasia.** Khaldon Y. Saleh and Nadine B. Smith (Dept. of Bioengineering, 205 Hallowell Bldg., The Penn State Univ., University Park, PA 16802)

Focused ultrasound surgery (FUS) is a clinical method for treating benign prostatic hyperplasia (BPH) in which tissue is noninvasively necrosed by elevating the temperature at the focal point above 60 °C using short sonications. With 1.75-dimensional (1.75-D) arrays, the power and phase to the individual elements can be controlled electronically for focusing and steering. This research describes the design, construction and evaluation of a 1.75-D ultrasound phased array to be used in the treatment of benign prostatic hyperplasia. The array was designed with a steering angle of  $\pm 13.5$  deg in the transverse direction, and can move the focus in three parallel planes in the longitudinal direction with a relatively large focus size. A piezoelectric ceramic (PZT-8) was used as the material of the transducer and two matching layers were built for maximum acoustic power transmission to tissue. To verify the capability of the transducer for focusing and steering, exosimetry was performed and the results correlated well with the calculated fields. *In vivo* experiments were performed to verify the capability of the transducer to ablate tissue using short sonications. [Work supported by the Whitaker Foundation and the Department of Defense Congressionally Directed Medical Prostate Cancer Research Program.]

**2pBB4. Optimized hyperthermia treatment of prostate cancer using a novel intravaginary ultrasound array.** Osama M. Al-Bataineh, Nadine B. Smith (Dept. of Bioengineering, The Penn State Univ., University Park, PA 16802), Robert M. Keolian, Victor W. Sparrow (The Penn State Univ., University Park, PA 16802), and Lewis E. Harpster (Penn State Milton S. Hershey Medical Ctr., Hershey, PA 17033)

Localized uniformly distributed ultrasound-induced hyperthermia is a useful adjuvant to radiotherapy in the treatment of prostate cancer. A two-dimensional,  $20 \times 4$  element, transrectal phased-array probe was designed to deliver a uniform and controllable amount of heat directly to the prostate without damaging the rectal wall or surrounding tissue. A three-dimensional prostate model was created using anatomical markers from the Visible Human Project to optimize the array. Sound speed, density, and absorption parameters were mapped to hue, saturation and value of the photographic data to simulate sound propagation through inhomogeneous tissue using the  $k$ -space method. To satisfy the requirements of this method from 1.2 to 1.8 MHz, the grid was adjusted to have 5 points per millimeter in each Cartesian direction. A spherical wave pulse was propagated through the model using tapered absorption boundary conditions. The expected temperature rise due to sound was obtained using the bio-heat transfer equation. Optimal insonification parameters that uniformly heat the prostate to  $43^\circ\text{C}$  for 40–60 minutes were determined for use in the construction of a clinical hyperthermia array. [Research supported by the Department of Defense Congressionally Directed Medical Prostate Cancer Research Program.]

2:00

**2pBB5. Separating thermal coagulation and cavitation effects in HIFU attenuation measurements.** Justin Reed, Michael Bailey, Ajay Anand, and Peter Kaczowski (Appl. Phys. Lab., Univ. of Washington, 1013 NE 40th St., Box 355640, Seattle, WA 98105-6698)

HIFU can be used to destroy tumors. The conversion of acoustic energy into heat causes protein coagulation (Lesion) in tissue. Attenuation measurements have been proposed to monitor the progression of thermal therapy. The goal of this work is to study and separate the effects of cavitation and thermal coagulation in attenuation measurements. A HIFU transducer was used to treat Bovine liver. A receiving transducer mounted across from the transmitting HIFU transducer measured attenuation during the treatment. A pressure chamber provided static pressure greater than the pressure amplitude of the HIFU wave, which suppressed cavitation. rf data from a commercial ultrasound scanner was also obtained. A large increase in attenuation was observed with cavitation present, while a subtle increase in attenuation was observed with cavitation suppressed. Attenuation estimated from the RF data showed an increase in attenuation downstream of the location of the lesion with cavitation present, while a subtle increase in attenuation was observed at the location of the lesion with cavitation suppressed. It has been found that attenuation measurements are greatly affected by the presence of cavitation, and the actual effect of thermal coagulation on attenuation is quite small. [Work supported by NIH, NSF, NSBRI.]

2:15

**2pBB6. Numerical investigation of dual-frequency HIFU pulsing for lithotripsy.** Wayne Kreider, Michael Bailey, and Lawrence Crum (Ctr. for Industrial and Medical Ultrasound, APL, Univ. of Washington, 1013 NE 40th St., Seattle, WA 98105, wkreider@u.washington.edu)

As an alternative to traditional shock-wave lithotripsy, high-intensity focused ultrasound (HIFU) is currently being investigated for its capability to comminute renal calculi. Because current data indicate that cavitation plays a role in both stone comminution as well as collateral tissue damage, the cavitation effects of HIFU treatment strategies are investigated numerically. In particular, numerical simulations are designed to model the response of bubbles to acoustic excitations generated by a prototype, dual-

frequency HIFU transducer for lithotripsy. The prototype transducer is capable of producing both high- ( $\sim 4\text{MHz}$ ) and low-frequency ( $\sim 100\text{-kHz}$ ) outputs, while the bubble dynamics are modeled by the Gilmore equation for a single spherical bubble subject to diffusion. Numerical simulations are currently ongoing to investigate the effects of the relative phase between high and low-frequency pulses. Initial results demonstrate that the simultaneous application of high and low-frequency pulses can generate maximum pressures several orders of magnitude higher than high-frequency pulses alone.

2:30

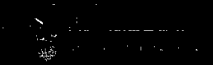
**2pBB7. The characterization of the lesion growth in time.** Marie Nakazawa, Justin A. Reed, Michael R. Bailey, and Yongmin Kim (Dept. of Elec. Eng., Univ. of Washington, 1400 NE Campus Pkwy., Seattle, WA, nakazawa@ns.cradle.titech.ac.jp)

Thermal heating effects of high intensity focused ultrasound (HIFU) on the dynamics of lesion formation were characterized automatically to assess the role of vapor bubbles in distorting the shape. Tissue mimicking phantom was used in experiments by a 4.2 MHz curve-linear transducer with 44 mm diameter and 44 mm radius of curvature. A variety of HIFU intensities were produced by different amplitudes. Images were acquired by a CCD camera and HDI-1000 ultrasound imager, recorded to VHS, and digitized to measure lesion size and shape. Each image was subtracted with noise reduction in order to detect the HIFU on time and to segment the boundaries of the lesions performed by Matlab programming. Area, length, width, and ratio of lesion area proximal to center line over area distal to center line were calculated along HIFU exposure time. Slight increase in HIFU intensity means hyperecho forms earlier, and lesion shape change. The data supported the hypothesis that lesion dramatically distorts well after hyperecho with only small increase in HIFU intensity. [Work supported by National Space and Biomedical Research Institute.]

2:45

**2pBB8. Optimization of angular compounding in scatterer size estimation.** Anthony L. Gerig, Quan Chen, and James A. Zagzebski (Dept. of Medical Phys., Univ. of Wisconsin-Madison, 1300 Univ. Ave., Rm. 1530, Madison, WI 53706, algerig@wisc.edu)

Ultrasonic scatterer size estimates generally have large variances due to the inherent noise of the spectral estimates used to calculate size. Compounding partially correlated size estimates associated with the same tissue, but produced with data acquired from different angles of incidence, is an effective way to reduce the variance without making dramatic sacrifices in spatial resolution. This work derives theoretical approximations for the correlation between these size estimates, and between their associated spectral estimates, as functions of data acquisition and processing parameters, where a Gaussian spatial autocorrelation function is assumed to adequately model scatterer shape. Size results exhibit a fair degree of agreement with those of simulation experiments, while spectral results compare favorably with simulation outcomes. Utilization of the theoretical correlation expressions for data acquisition and processing optimization is discussed. Further simplifying approximations, such as the invariance of phase and amplitude terms with rotation angle, are made in order to obtain closed-form solutions to the derived spectral correlation, and permit an analytical optimization analysis. Results indicate that recommended parameter adjustments for performance improvement depend upon whether, for the system under consideration, the primary source of estimate decorrelation with rotation is scatterer phase change or field separation. [Work supported by NIH T32CA09206.]

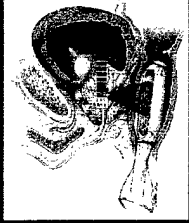

**The Pennsylvania State University**  
 Graduate Program in Acoustics

**Design and evaluation of a 63 element 1.75-D ultrasound phased array for treating benign prostatic hyperplasia**

Khaldon Y. Saleh<sup>1</sup> and Nadine Barrie Smith<sup>1,2</sup>  
 The Pennsylvania State University  
 College of Engineering  
 Department of Bioengineering<sup>1</sup> and Graduate Program in Acoustics<sup>2</sup>  
 University Park, PA 16802

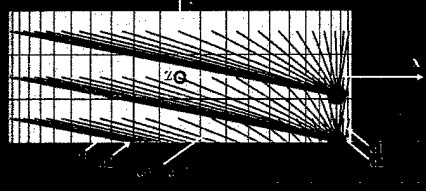
**Introduction**

- 1.75-D array design.
- Focusing and steering in a 3-D volume.
- Two matching layers to increase acoustical power transmission.
- Low capacitance cable and matching circuits.


  
<http://www.focus-surgery.com>

**Design issues**

Huygens' principle to determine the pressure.



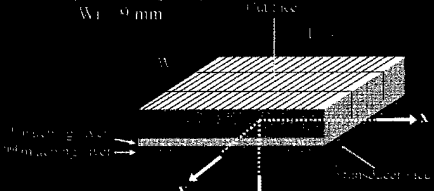
$$p(x, y, z) = \frac{j\rho c}{4\pi} \iint_{S_0} \frac{e^{j\omega(t - \frac{r}{c})}}{r} \exp(j\phi) - \frac{2\pi h}{\lambda} - d_0 \alpha$$

$$\phi_0 = \frac{360}{\lambda} (d_0 - d_1) = 360 \theta$$

**1.75-D array design**

21 x 3 1.75-D dimensional phased array.

$L = 0.83[2 - \text{hamming}(21)] \text{ mm}$   
 $W = 9 \text{ mm}$

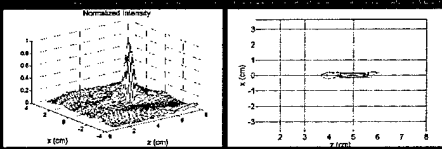


Frequency: 1.2 MHz.  
 Ceramic: PZT-8.

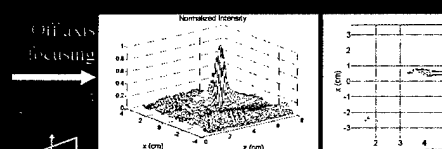
x: Transverse  
 y: Longitudinal  
 z: Radial

**Simulation results**

**On axis focusing**

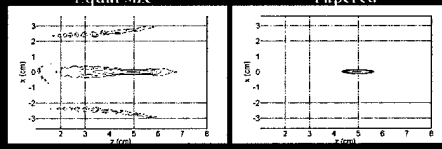


**Off axis focusing**

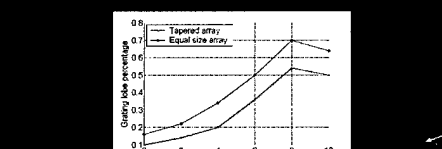


**Simulation results (Grating lobe reduction)**

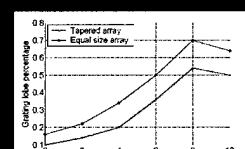
**Equal size**



**Tapered**



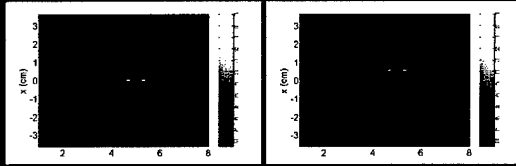
Variable length elements (tapered) versus equal size elements



## Simulation results (Temperature simulations)

Bio-Heat Transfer Equation (BHTE).

$$\rho C_p \frac{\partial T}{\partial t} = k \left( \frac{\partial^2 T}{\partial x^2} + \frac{\partial^2 T}{\partial y^2} + \frac{\partial^2 T}{\partial z^2} \right) - \rho C_b (T - T_a) + q(x, y, z)$$



Temperature = 60 °C at the focal point  
Simulation time = 10 sec

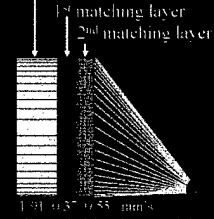
## Construction issues (Matching layers)

GND P/T-S elements

$$Z_1 = (Z_{piezo})^{4/7} (Z_{tissue})^{3/7}$$

$$Z_2 = (Z_{piezo})^{1/7} (Z_{tissue})^{6/7}$$

1<sup>st</sup> matching layer:  
2-3.5 micron Silver epoxy  
Silver powder  
2<sup>nd</sup> matching layer:  
Epo-Tek 301

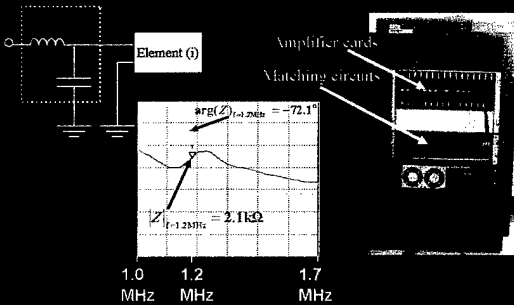


Dieing  
Kerf width: 0.3 mm



## Construction issues (Electrical impedance matching)

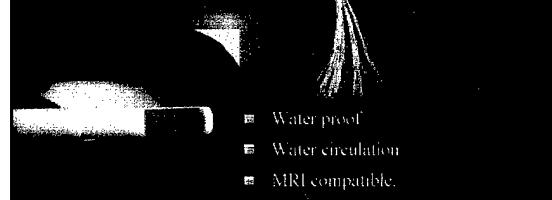
Matching circuit (i)



## Construction

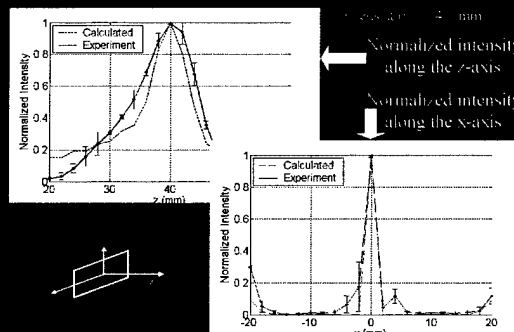
Building the matching layers  
then dice the ceramic.  
The ceramic was cut in house  
in our lab.

Wiring and water  
circulation tubes



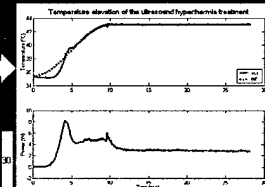
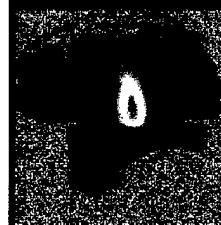
- Water proof
- Water circulation
- MRI compatible.

## Exposimetry results



## Ex vivo / In vivo experiments

*In vivo* control experiment  
On rabbit thigh muscle.



A temperature map obtained by  
an MRI scan for *Ex vivo* bovine.  
Heating time: 2 minutes

## Conclusions

- A 1.75-D phased array capable of focusing and steering in a volume
- Matching layers to acoustically match
- Low capacitance cable to prevent loss of power due to the high element impedance
- The final array was water proof and MRI compatible
- Exposimetry results correlate well with theory
- MRI experiments to monitor temperature

## Acknowledgments

- Whitaker Foundation
- Department of Defense Congressionally Directed Medical - Prostate Cancer Research Program - Idea Development Award



## Therapeutic Applications of Ultrasound: Treatment of Prostate Disease, Minimally Invasive Tumor Treatment and Noninvasive Drug Delivery

Nadine Barrie Smith  
The Pennsylvania State University  
College of Engineering  
University Park, PA 16802

## Therapeutic Ultrasound Arrays

### Prostate Disease

- Prostate cancer: Hyperthermia, unfocused US heating 42-45°C for 30-60 min (1.5 MHz)
- Benign Prostatic Hyperplasia: Focused heating to ablate tissue: 60-100°C for 1-10 seconds (1.5 MHz)

### Hollow Sphere piezoelectric as a .....

- High Pressure Hydrophone
- Minimally Invasive Interstitial Ablation

### Noninvasive Drug Delivery

Develop a light weight, low profile (practicable) device to transdermally deliver insulin across skin without bioeffects (20 kHz)

## Prostate Cancer

- In the US alone: 179,300 new cases of prostate cancer 2000.
- With a estimated 37,000 deaths per year, this is the second leading cause of cancer death in men (American Cancer Society).
- Current treatment :
  - Surgery
  - Hormone therapy
  - Chemotherapy
  - Radiotherapy
  - Wait-and-see
- One clinically used treatment is to use transrectal ultrasound hyperthermia in conjunction with external beam irradiation.

## Transrectal Array

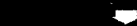
- Ultrasound offers an attractive means of noninvasive localized hyperthermia treatment of tumors in the prostate due to the proximity of the prostate to the rectum.
- IDE approved device, current in use in Phase II patient trials at Dana-Farber Cancer Institute, Boston, MA.

## MRI Thermometry

- Traditionally, invasive thermometry has been used to measure temperatures in the target region. Thermocouples may bypass the regions of greatest temperature elevation.
- Explores the potential of MR guidance and thermometry for clinical therapy. This method relies on frequency changes resulting from temperature-dependent variations in the molecular shielding constant of the water molecule

## Materials and Methods

Power Field Simulations  
(Rayleigh-Sommerfeld Integral)  
O'Neil 1949



Temperature Simulations  
(Bio-heat transfer equation)  
Pennes 1948



Thermal Dose  
(estimate of time required for a hyperthermia treatment, 30 minutes at 43°C)  
Sapareto and Dewey, 1984

Power field simulations (Rayleigh-Sommerfeld Integral, O'Neil 1949)

Acoustic pressure  $p(x, y, z)$  at any point  $i$  in the field:

$$p_i(x, y, z) = \frac{j\omega\rho_0}{4\pi c} \iint_S \left\{ \left( \frac{\partial \phi}{\partial z} \right)_0 \right\} e^{-jk\sqrt{r^2 + z^2}} \cdot d\alpha$$

net power deposition at  $(x, y, z)$

$$q(x, y, z) = \frac{\alpha P}{\rho c} \cdot \frac{(x, y, z)}{r^2}$$



Temperature simulations (Bio-heat transfer equation, Pennes 1948)

$$\rho c \frac{dT}{dt} = k \left( \frac{d^2 T}{dx^2} + \frac{d^2 T}{dy^2} + \frac{d^2 T}{dz^2} \right) - w c_b (T - T_b) + (Q_p - Q_m)$$

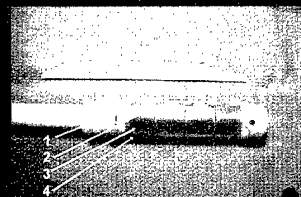
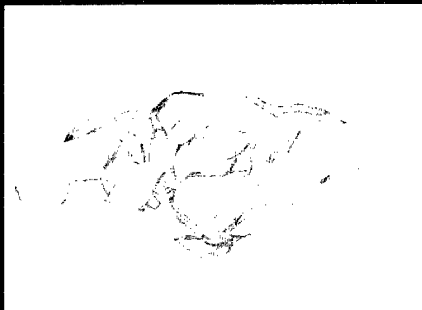
Thermal Dose

\* estimate of time required for a hyperthermia treatment (Sapareto and Dewey, 1984)  
\* 30 minutes at 43°C

$$\text{Dose}(T_{ref}) = \sum_{t=0}^{t_{max}} R^{43-T_w} \Delta t$$

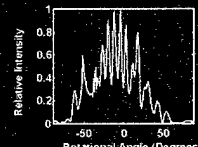
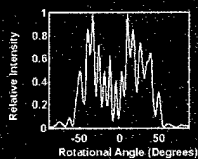
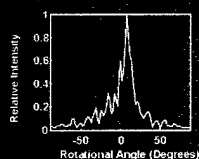
### Computer Tomography (CT)

12 patients with prostate cancer  
AutoCAD



- \* 16 channels, 4 x 4 pattern. Applicator machined from Delrin<sup>®</sup>.
- \* Cut from 25 mm O.D., 15 mm long, cylinders of PZT-8 material (EDO, Salt Lake City). Scored on inner surface.
- \* 120° angular beam field and length 6 cm would heat the entire gland. Diameter limited to 23 mm.

### Array Exosimetry



### Non-Invasive MRI Thermometry

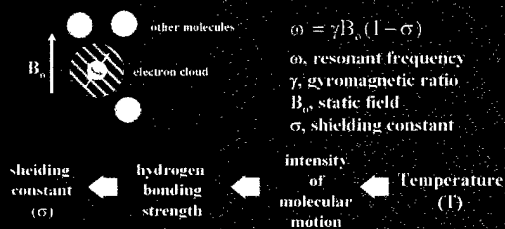
- Applications
- (a) hyperthermia
  - (b) focused ultrasound surgery
  - (c) laser induced ablation
  - (d) cryosurgery
  - (e) RF microwave

Invasive techniques using thermocouples interfere with the temperature distribution and give information at a few pre-determined sites.

#### Proton Resonance Frequency Shift :

- \*  $\pm 0.5-1.0$  °C temperature resolution
- \* 1 mm spatial resolution

### MRI Temperature Proton Chemical Shift



In MRI, the spatial position and the chemical shift are encoded by phase and frequency of the precession of the protons, respectively.

### Temperature Measurements: (Ishihara et al., 1985)

Temperature sensitive proton resonant frequency shift

$$\Delta T = - \frac{\Delta \phi}{\gamma \cdot TE \cdot B_0 \cdot \alpha(T)}$$

where,  $\Delta T$  = temperature change (°C)

$\Delta \phi$  = phase change (rads)

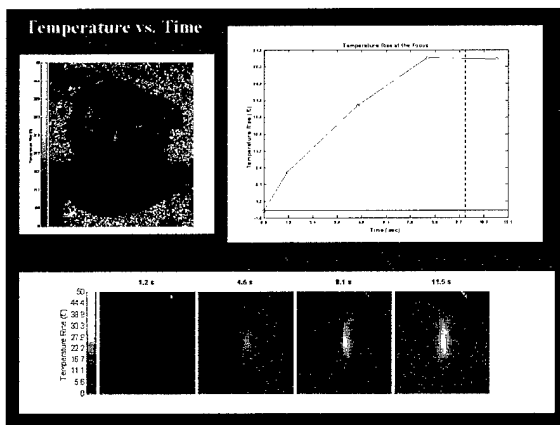
TE = Echo Time (sec)

$\gamma = 2\pi \cdot 42.58$  MHz/T

$B_0 = 1.5$  T

$\alpha(T)_{\text{muscle}} = -0.00909$  ppm/°C

$\alpha(T)_{\text{milk}} = -4.59 \times 10^{-3}$  ppm/°C



### Materials and Methods :

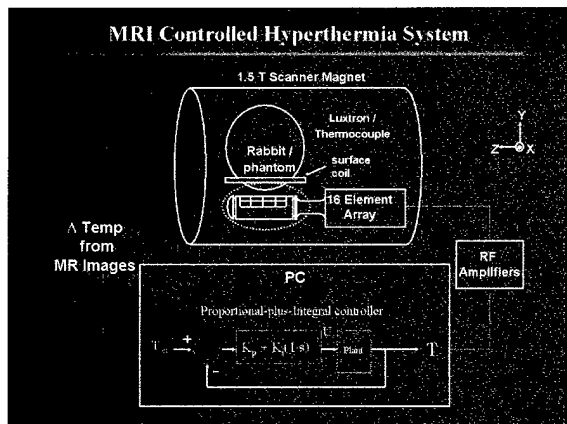
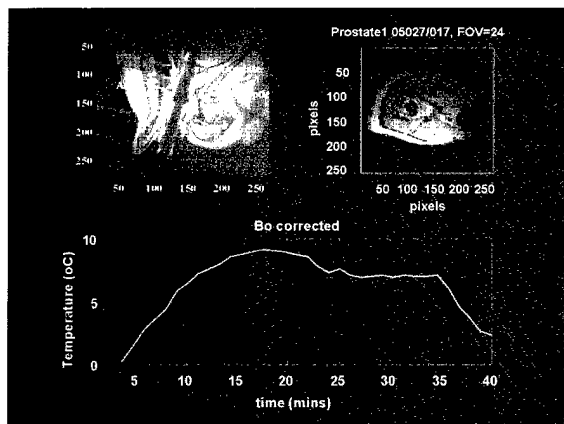
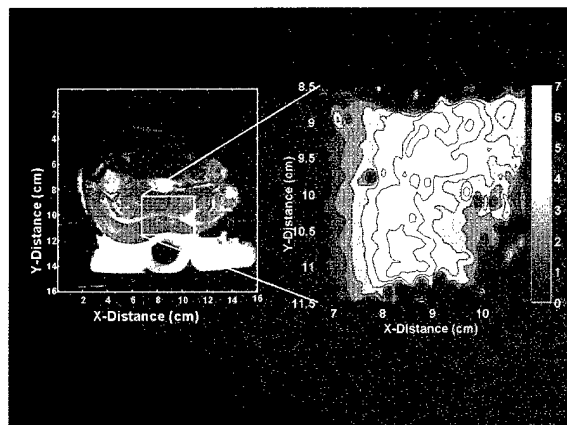
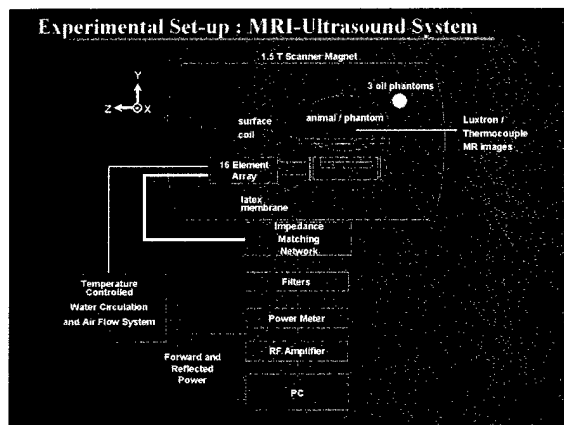
**Experiments**

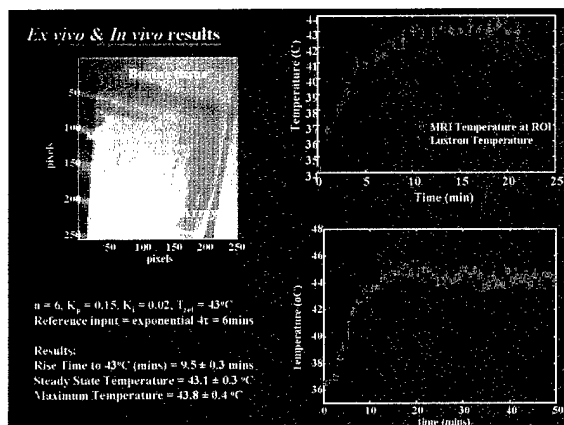
- Ex vivo* bovine muscle
- In vivo* rabbit muscle (IACUC approval: ketamine-xylazine)
- In vivo* canine prostate
- Ex vivo, in vivo* MRI feedback

**Temperature probes**

- Thermocouple (copper and constantan, 50µm dia)
- Luxtron fiber optic with a brass catheter surrounding

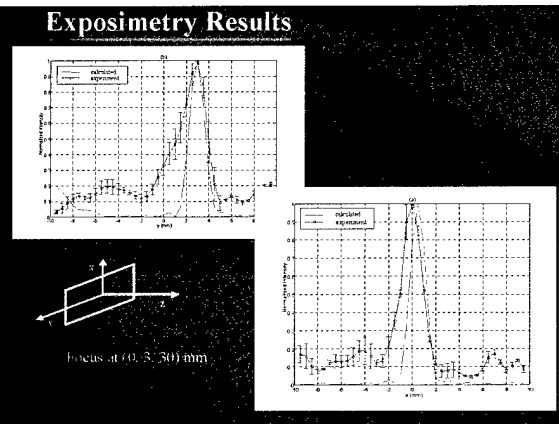
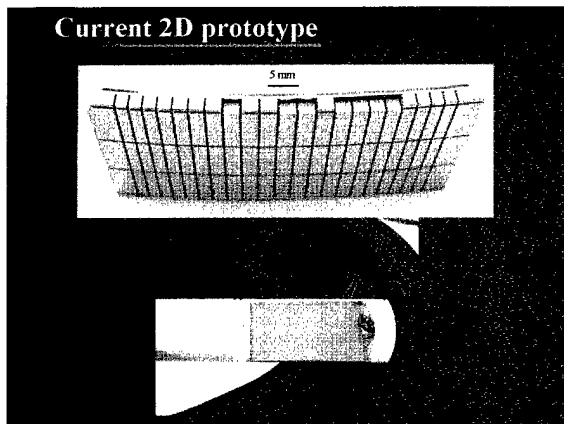
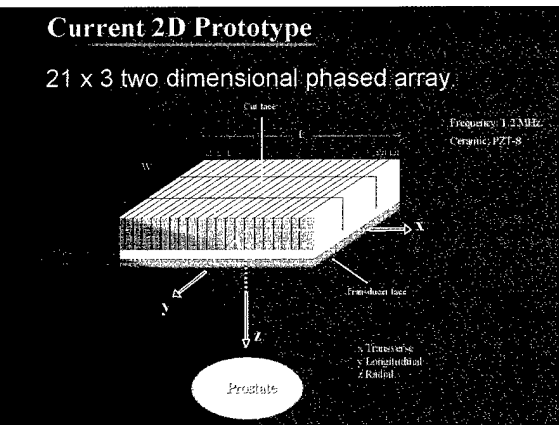
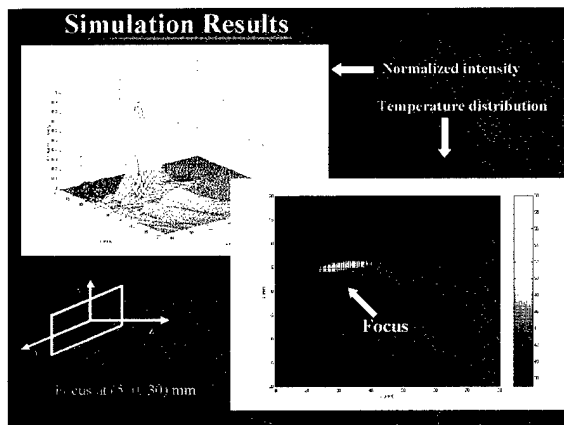
**MRI: 1.5 Tesla Clinical Scanner (GE Medical Systems, Milwaukee, WI)**

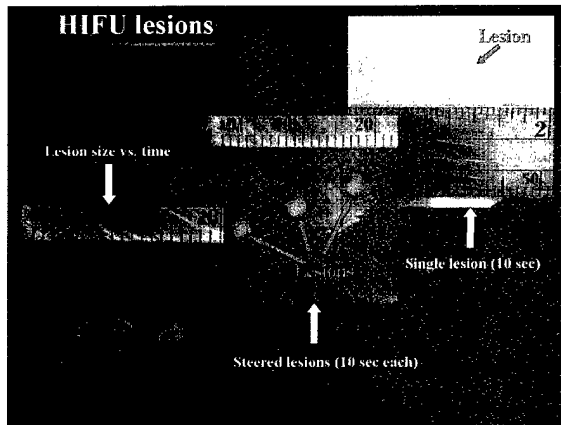




### Focused US for Treatment of Benign Prostatic Hyperplasia

♦ Design a focused 2-D (1.2 MHz, 64 elements), linear array for ablating abnormal prostate tissue in the focal zone up to  $60-100^\circ\text{C}$  in a very short duration ( $< 10$  sec).  
 ♦ Theoretically evaluate the pressure field using Rayleigh Integral.  
 ♦ Steer the US focus with a custom (computer) amplifier: amplitude: 0-60 electrical watts per channel, phase:  $\pm 1^\circ$ .  
 ♦ Experimentally evaluate the pressure field using hydrophone data and compare to theoretical results. Ex vivo results.





## Therapeutic Ultrasound Arrays

### Prostate Disease

- Prostate cancer: Hyperthermia, unfocused US heating 42–45°C for 30–60 min (1.5 MHz)
- Benign Prostatic Hyperplasia: Focused heating to ablate tissue: 60–100°C for 1–10 seconds (1.5 MHz)

### Hollow Sphere piezoelectric as a .....

- High Pressure Hydrophone
- Minimally Invasive Interstitial Ablation

### Noninvasive Drug Delivery

Develop a light weight, low profile (practicable) device to transdermally deliver insulin across skin without bioeffects (20 kHz)

### Novel Piezoceramic Hollow Sphere as a .....

#### Hydrophone

Ultrasound Receiving Device as a High Pressure Hydrophone

#### Transducer

Ultrasound Transmitting Device for Minimally Invasive Interstitial Ablation



- Omni-directional
- High Sensitivity
- Low Overall Density
- Miniature Size
- Withstand High Pressures

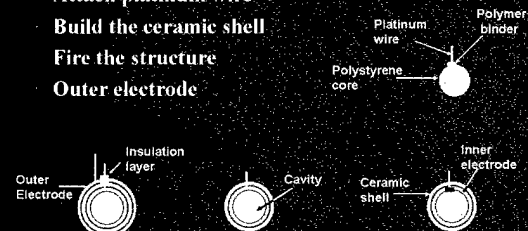
## Co-firing Technique

Attach platinum wire

Build the ceramic shell

Fire the structure

Outer electrode



(Newnham et al. 2002)

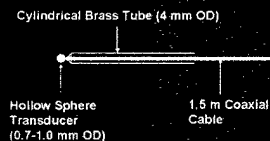
## High Pressure Hydrophone

1.5 m coaxial cable

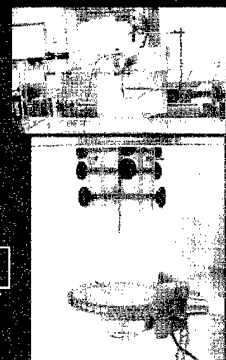
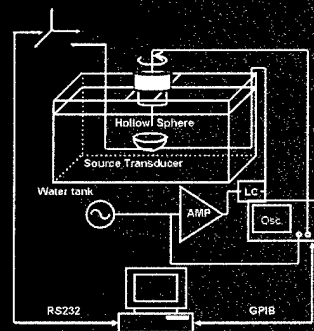
Suitable housing

Insulation layer

BNC connector

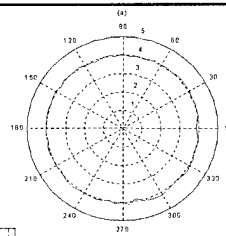
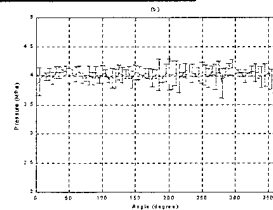


## Exposimetry Setup



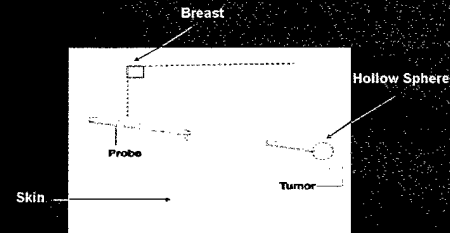
## Results

Flat sensitivity response  
Omni-directional receiving pattern  
1.7 MHz



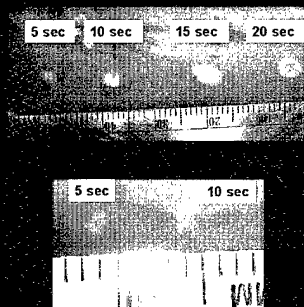
## Interstitial Ablation Device

- Bolus of water
- CW excitation
- Porcine kidney cortex tissue ablation



## Results

Resonance Frequency (1.87 and 2.7 MHz)  
Necrosed volume increased as a function of sonication period



## Therapeutic Ultrasound Arrays

### Prostate Disease

- Prostate cancer: Hyperthermia, unfocused US heating 42–45°C for 30–60 min (1.5 MHz)
- Benign Prostatic Hyperplasia: Focused heating to ablate tissue: 60–100°C for 1–10 seconds (1.5 MHz)

### Hollow Sphere piezoelectric as a .....

- High Pressure Hydrophone
- Minimally Invasive Interstitial Ablation

### Noninvasive Drug Delivery

- Develop a light weight, low profile (practicable) device to transdermally deliver insulin across skin without bioeffects (20 kHz)

## Noninvasive Drug Delivery

Approximately 15.7 million people in the United States suffer from diabetes. From a human and economic perspective, it is one of the most costly diseases (US Congressionally / Insulin Diabetes Research Working Group 1999; NIH Pub 99-1968).

Until a cure can be found, management of diabetes sometimes requires painful repetitive injections of insulin up to three times each day.

Studies have shown that ultrasound mediated transdermal drug delivery offers promising potential for noninvasive drug administration

The goal of this research was to design a small, light weight, low profile array based on the cymbal transducer which could transdermally deliver insulin *in vivo*.

Compound	Preparation	Frequency	Intensity	Device	Investigator
Aldosterone	in vitro human	20 kHz	125 mW/cm <sup>2</sup>	Sonicator <sup>®</sup>	(Johnson et al. 1996)
Benzene	in vitro human	1.3 MHz	2 W/cm <sup>2</sup>	Therapeutic US	(Mitrangiti et al. 1995b)
Bicarbonate	in vivo rat	20 kHz	1 W/cm <sup>2</sup>	Sonicator <sup>®</sup>	(Mitrangiti et al. 2000a)
Butanol	in vitro human	1.3 MHz	2 W/cm <sup>2</sup>	Therapeutic US	(Mitrangiti et al. 1995b)
Caffeine	in vitro human	1.3 MHz	2 W/cm <sup>2</sup>	Therapeutic US	(Mitrangiti et al. 1995b)
Calcium	in vivo rat	20 kHz	1 W/cm <sup>2</sup>	Sonicator <sup>®</sup>	(Mitrangiti et al. 2000a)
Corticosterone	in vitro human	20 kHz	125 mW/cm <sup>2</sup>	Sonicator <sup>®</sup>	(Johnson et al. 1996)
Dexamethasone	in vitro human	1 MHz	1.4 W/cm <sup>2</sup>	Therapeutic US	(Johnson et al. 1996)
Dextran <sup>®</sup>	in vivo rat	20 kHz	1 W/cm <sup>2</sup>	Sonicator <sup>®</sup>	(Mitrangiti et al. 2000a)
Estrogen	in vitro human	1 MHz	1.4 W/cm <sup>2</sup>	Therapeutic US	(Johnson et al. 1996)
Glucose <sup>®</sup>	in vitro human	20 kHz	1 W/cm <sup>2</sup>	Sonicator <sup>®</sup>	(Kott et al. 1996)
Insulin	in vivo rat	20 kHz	1 W/cm <sup>2</sup>	Sonicator <sup>®</sup>	(Mitrangiti et al. 2000a)
Lidocaine	in vitro human	1 MHz	1.4 W/cm <sup>2</sup>	Therapeutic US	(Johnson et al. 1996)
Linoleic acid	in vitro human	1 MHz	1.4 W/cm <sup>2</sup>	Therapeutic US	(Johnson et al. 1996)
Mannitol	in vivo rat	20 kHz	1 W/cm <sup>2</sup>	Sonicator <sup>®</sup>	(Mitrangiti et al. 2000a)
Progesterone	in vitro human	1.3 MHz	2 W/cm <sup>2</sup>	Therapeutic US	(Mitrangiti et al. 1995b)
Salicylic acid	in vivo guinea pig	2–16 MHz	0.2 W/cm <sup>2</sup>	Phonemeter <sup>®</sup>	(Bouman et al. 1992)
Sucrose	in vitro human	20 kHz	125 mW/cm <sup>2</sup>	Sonicator <sup>®</sup>	(Johnson et al. 1996)
Testosterone	in vitro human	1 MHz	1.4 W/cm <sup>2</sup>	Therapeutic US	(Johnson et al. 1996)
Urea	in vivo rat	20 kHz	1 W/cm <sup>2</sup>	Sonicator <sup>®</sup>	(Mitrangiti et al. 2000a)
Water	in vitro human	20 kHz	125 mW/cm <sup>2</sup>	Sonicator <sup>®</sup>	(Johnson et al. 1996)

### Summary of papers using ultrasound for enhanced insulin delivery

Preparation	Frequency	Intensity	Device	Reference
<i>in vitro</i> human <i>in vivo</i> rat	20 kHz	$I_{app} = 12.5 - 225$ $mW/cm^2$	sonicator <sup>1</sup>	Mitragotri et al., 1995
<i>in vitro</i> human	20 kHz	$0.1 - 1^* W/cm^2$	sonicator <sup>2</sup>	Zhang et al., 1996
<i>in vivo</i> rat	20 kHz	$2.5, 10^* W/cm^2$	sonicator <sup>2</sup>	Boucaud et al., 2000
<i>in vivo</i> rat	48 kHz	$0.6 - 4.3^*$ $mW/cm^2$	ultrasonic bath <sup>4</sup>	Tachibana 1991
<i>in vivo</i> rabbit	105 kHz	$1.7^* mW/cm^2$	piezoelectric transducer <sup>3</sup>	Tachibana 1992

Legend: <sup>1</sup> Brand not indicated; <sup>2</sup> W-385 Heat Systems Ultrasonics, Inc., Farmingdale, NY; <sup>3</sup> VCX 400, Sonics and Materials, Newtown, CT; <sup>4</sup> Cole Parmer Instrument Co, Chicago, IL; <sup>5</sup> Transducer company not indicated.

### Insulin Delivery Transducers

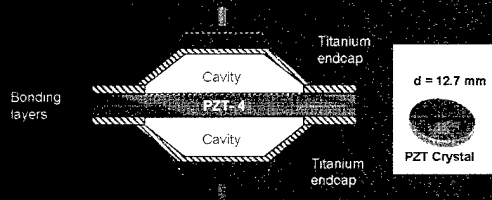
Want.....

- Miniature in size
- Frequency range will be between 20 – 100 kHz
- Capability of generating sufficient high pressure and intensity
- High efficiency
- Low cost

### Cymbal arrays

- Compact, light structure
- Resonance frequency adjustable between 20-50 kHz
- Low cost (ST)
- Accurate and precise exposimetry

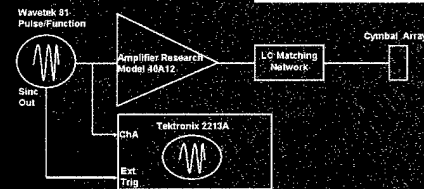
### Cymbal Single Element Transducer



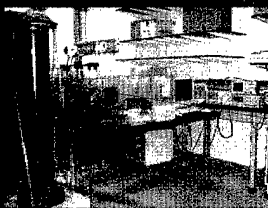
- Lead zirconate-titanate (PZT-4) ceramic
- Radial motion (i.e. the vibration moves from the center of the disc to the edges with radial symmetry)
- Cavities amplify the radial displacement into large axial displacement normal to the caps

### Cymbal Array

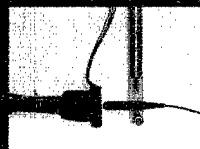
- Water-proof, electrical matching
- Encased in a URALITE<sup>®</sup> polymer (acoustic impedance = water)
- Four cymbal transducers arranged in a 2 x 2 pattern
- Weight = 22 grams



### Ultrasound Exposimetry

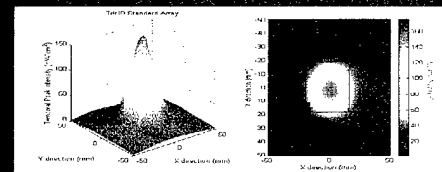


- \* Degassed, distilled water (1-2 ppm).
- \* Anechoic using sound absorbing material.
- \* Automated using computer control.



### Exposimetry Results

- $\Delta WG = 600 mV_{pp}$  w/ pulse duration of 200 ms and pulse repetition period of 1 second (i.e. 20% duty cycle). Amplifier gain was 50 dB.
- Multiple scannings, 3-5 each.
- Determined over planes of 0.1, 2 and 5 mm from the array surface.



Plane	$P_1$	$P_2$	$I_{app1}$	$I_{app2}$	$I_{app3}$	$I_{app4}$
0 mm	54738.9	56375.7	207.2	31.1	1.6	25.8
1 mm	51633.6	51633.6	180.1	28.0	1.4	24.0
2 mm	49125.5	49762.5	167.3	25.6	1.3	22.1
5 mm	43552.1	44149.3	131.7	20.3	1.0	17.4

Pressure in Pa; Intensity in  $mW/cm^2$ .

### Prior *ex vivo* experiments results

Abdominal *ex vivo* human skin samples (skin bank) were used for Humulin® R and Humalog® insulin transmission experiments.

For determining transport of insulin across *ex vivo* human skin, a Franz diffusion cell was used. Ultrasound exposed for 1 hour at  $I_{\text{app}} = 173.7 \pm 1.2 \text{ mW/cm}^2$ ,  $I_{\text{app}} = 1.1 \pm 0.05 \text{ mW/cm}^2$ .

Insulin concentrations in the receiver compartment measured over one hour was determined using a spectrophotometer.

Visual and microscopic examination of the post ultrasound exposed skin did not indicate any noticeable damage or significant change to the skin.

(U/hr)	Humulin® R	Humalog®
Control	$4.1 \pm 0.5$ (n=3)	$7.0 \pm 4.4$ (n=5)
Cymbal Array	$45.9 \pm 12.9$ (n=15)	$30.8 \pm 12.6$ (n=6)

(Smith et al. "Ultrasound Mediated Transdermal Transport of Insulin through *in vivo* Human Skin using Novel Transducer Designs" UMD, 29 (2), 311 - 317, 2003.

### *In vivo* rat experiments procedure

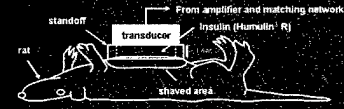
PSU IACUC approved protocol

Anesthetic - ketamine (60 mg/kg) and XYLIZINE (10 mg/kg)

Hyperglycemia induced by xylazine (Kawai et al. 1997)

Glucose level for normal rats:  $\approx 100 \text{ mg/dL}$

Hyperglycemia:  $419 \pm 31 \text{ mg/dL}$  (n=20)



Glucose determination:

Blood (0.1 ml) removed from jugular vein at the start & every 30 minutes up to 90 minutes

ACCU-CHEK™ blood glucose monitoring system

Normalize results with respect to a baseline for each rat

### *In vivo* experiments procedure

Six groups (29 rats total, 4-5 rats/group, 90 min procedure)

Control (insulin, no ultrasound, n=5)

Negative control (saline with ultrasound, n=5)

Ultrasound exposure at  $I_{\text{app}} = 100 \text{ mW/cm}^2$  for

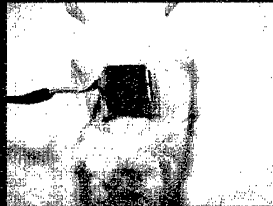
60 min (n=5),

20 min (n=5),

10 min (n=4),

5 min (n=4)

Euthanized under anesthesia at end



### *In vivo* results

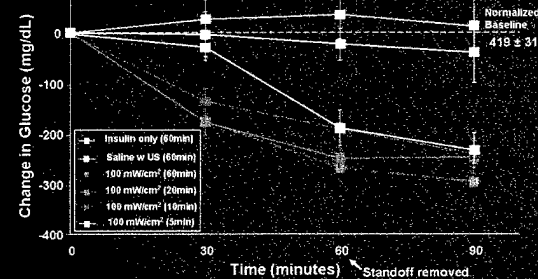
Human Fasting Glucose Test for Diabetes (mg/dL)

\*Normal: 70-110

\*Impaired fasting glucose: 110-126

\*Impaired glucose tolerance: 140-200

\*Diabetic: > 200



### *In vivo* rabbit experiments

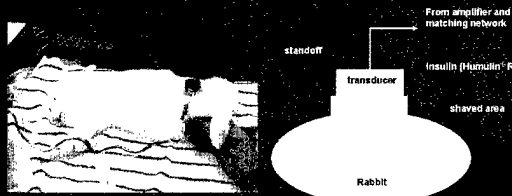
PSU IACUC approved protocol

Anesthetic - ketamine (40 mg/kg) and xylazine (10 mg/kg)

Hyperglycemia induced by xylazine (Kawai et al. 1997)

Normal glucose level for rabbits:  $\approx 100$ -135 mg/dL

After xylazine (hyperglycemia):  $245 \pm 45 \text{ mg/dL}$  (n = 14)

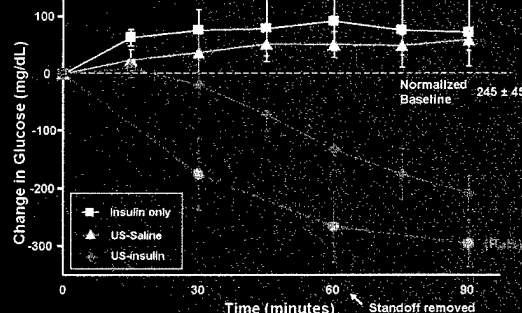


### *In vivo* rabbit experiments

Human Diabetes (mg/dL)

\*Normal: 70-110

\*Diabetic: > 200





1. *Journal of Management Studies*, 1996, 33, 1, 1-14.  
 2. *Journal of Management Studies*, 1996, 33, 1, 15-30.  
 3. *Journal of Management Studies*, 1996, 33, 1, 31-46.  
 4. *Journal of Management Studies*, 1996, 33, 1, 47-62.  
 5. *Journal of Management Studies*, 1996, 33, 1, 63-78.  
 6. *Journal of Management Studies*, 1996, 33, 1, 79-94.  
 7. *Journal of Management Studies*, 1996, 33, 1, 95-110.  
 8. *Journal of Management Studies*, 1996, 33, 1, 111-126.  
 9. *Journal of Management Studies*, 1996, 33, 1, 127-142.  
 10. *Journal of Management Studies*, 1996, 33, 1, 143-158.  
 11. *Journal of Management Studies*, 1996, 33, 1, 159-174.  
 12. *Journal of Management Studies*, 1996, 33, 1, 175-190.  
 13. *Journal of Management Studies*, 1996, 33, 1, 191-206.  
 14. *Journal of Management Studies*, 1996, 33, 1, 207-222.  
 15. *Journal of Management Studies*, 1996, 33, 1, 223-238.  
 16. *Journal of Management Studies*, 1996, 33, 1, 239-254.  
 17. *Journal of Management Studies*, 1996, 33, 1, 255-270.  
 18. *Journal of Management Studies*, 1996, 33, 1, 271-286.  
 19. *Journal of Management Studies*, 1996, 33, 1, 287-302.  
 20. *Journal of Management Studies*, 1996, 33, 1, 303-318.  
 21. *Journal of Management Studies*, 1996, 33, 1, 319-334.  
 22. *Journal of Management Studies*, 1996, 33, 1, 335-350.  
 23. *Journal of Management Studies*, 1996, 33, 1, 351-366.  
 24. *Journal of Management Studies*, 1996, 33, 1, 367-382.  
 25. *Journal of Management Studies*, 1996, 33, 1, 383-398.  
 26. *Journal of Management Studies*, 1996, 33, 1, 399-414.  
 27. *Journal of Management Studies*, 1996, 33, 1, 415-430.  
 28. *Journal of Management Studies*, 1996, 33, 1, 431-446.  
 29. *Journal of Management Studies*, 1996, 33, 1, 447-462.  
 30. *Journal of Management Studies*, 1996, 33, 1, 463-478.  
 31. *Journal of Management Studies*, 1996, 33, 1, 479-494.  
 32. *Journal of Management Studies*, 1996, 33, 1, 495-510.  
 33. *Journal of Management Studies*, 1996, 33, 1, 511-526.  
 34. *Journal of Management Studies*, 1996, 33, 1, 527-542.  
 35. *Journal of Management Studies*, 1996, 33, 1, 543-558.  
 36. *Journal of Management Studies*, 1996, 33, 1, 559-574.  
 37. *Journal of Management Studies*, 1996, 33, 1, 575-590.  
 38. *Journal of Management Studies*, 1996, 33, 1, 591-606.  
 39. *Journal of Management Studies*, 1996, 33, 1, 607-622.  
 40. *Journal of Management Studies*, 1996, 33, 1, 623-638.  
 41. *Journal of Management Studies*, 1996, 33, 1, 639-654.  
 42. *Journal of Management Studies*, 1996, 33, 1, 655-670.  
 43. *Journal of Management Studies*, 1996, 33, 1, 671-686.  
 44. *Journal of Management Studies*, 1996, 33, 1, 687-702.  
 45. *Journal of Management Studies*, 1996, 33, 1, 703-718.  
 46. *Journal of Management Studies*, 1996, 33, 1, 719-734.  
 47. *Journal of Management Studies*, 1996, 33, 1, 735-750.  
 48. *Journal of Management Studies*, 1996, 33, 1, 751-766.  
 49. *Journal of Management Studies*, 1996, 33, 1, 767-782.  
 50. *Journal of Management Studies*, 1996, 33, 1, 783-798.  
 51. *Journal of Management Studies*, 1996, 33, 1, 799-814.  
 52. *Journal of Management Studies*, 1996, 33, 1, 815-830.  
 53. *Journal of Management Studies*, 1996, 33, 1, 831-846.  
 54. *Journal of Management Studies*, 1996, 33, 1, 847-862.  
 55. *Journal of Management Studies*, 1996, 33, 1, 863-878.  
 56. *Journal of Management Studies*, 1996, 33, 1, 879-894.  
 57. *Journal of Management Studies*, 1996, 33, 1, 895-910.  
 58. *Journal of Management Studies*, 1996, 33, 1, 911-926.  
 59. *Journal of Management Studies*, 1996, 33, 1, 927-942.  
 60. *Journal of Management Studies*, 1996, 33, 1, 943-958.  
 61. *Journal of Management Studies*, 1996, 33, 1, 959-974.  
 62. *Journal of Management Studies*, 1996, 33, 1, 975-990.  
 63. *Journal of Management Studies*, 1996, 33, 1, 991-1006.  
 64. *Journal of Management Studies*, 1996, 33, 1, 1007-1022.  
 65. *Journal of Management Studies*, 1996, 33, 1, 1023-1038.  
 66. *Journal of Management Studies*, 1996, 33, 1, 1039-1054.  
 67. *Journal of Management Studies*, 1996, 33, 1, 1055-1070.  
 68. *Journal of Management Studies*, 1996, 33, 1, 1071-1086.  
 69. *Journal of Management Studies*, 1996, 33, 1, 1087-1102.  
 70. *Journal of Management Studies*, 1996, 33, 1, 1103-1118.  
 71. *Journal of Management Studies*, 1996, 33, 1, 1119-1134.  
 72. *Journal of Management Studies*, 1996, 33, 1, 1135-1150.  
 73. *Journal of Management Studies*, 1996, 33, 1, 1151-1166.  
 74. *Journal of Management Studies*, 1996, 33, 1, 1167-1182.  
 75. *Journal of Management Studies*, 1996, 33, 1, 1183-1198.  
 76. *Journal of Management Studies*, 1996, 33, 1, 1199-1214.  
 77. *Journal of Management Studies*, 1996, 33, 1, 1215-1230.  
 78. *Journal of Management Studies*, 1996, 33, 1, 1231-1246.  
 79. *Journal of Management Studies*, 1996, 33, 1, 1247-1262.  
 80. *Journal of Management Studies*, 1996, 33, 1, 1263-1278.  
 81. *Journal of Management Studies*, 1996, 33, 1, 1279-1294.  
 82. *Journal of Management Studies*, 1996, 33, 1, 1295-1310.  
 83. *Journal of Management Studies*, 1996, 33, 1, 1311-1326.  
 84. *Journal of Management Studies*, 1996, 33, 1, 1327-1342.  
 85. *Journal of Management Studies*, 1996, 33, 1, 1343-1358.  
 86. *Journal of Management Studies*, 1996, 33, 1, 1359-1374.  
 87. *Journal of Management Studies*, 1996, 33, 1, 1375-1390.  
 88. *Journal of Management Studies*, 1996, 33, 1, 1391-1406.  
 89. *Journal of Management Studies*, 1996, 33, 1, 1407-1422.  
 90. *Journal of Management Studies*, 1996, 33, 1, 1423-1438.  
 91. *Journal of Management Studies*, 1996, 33, 1, 1439-1454.  
 92. *Journal of Management Studies*, 1996, 33, 1, 1455-1470.  
 93. *Journal of Management Studies*, 1996, 33, 1, 1471-1486.  
 94. *Journal of Management Studies*, 1996, 33, 1, 1487-1502.  
 95. *Journal of Management Studies*, 1996, 33, 1, 1503-1518.  
 96. *Journal of Management Studies*, 1996, 33, 1, 1519-1534.  
 97. *Journal of Management Studies*, 1996, 33, 1, 1535-1550.  
 98. *Journal of Management Studies*, 1996, 33, 1, 1551-1566.  
 99. *Journal of Management Studies*, 1996, 33, 1, 1567-1582.  
 100. *Journal of Management Studies*, 1996, 33, 1, 1583-1598.  
 101. *Journal of Management Studies*, 1996, 33, 1, 1599-1614.<